SPACE ENVIRONMENT TECHNOLOGIES

SET TR 2011-001

Energy Balance in the Core of the Saturn Plasma Sheet

Jean Michi Yoshii

Dec 2011

Notice: This document is released for public distribution by Space Environment Technologies.

ENERGY BALANCE IN THE CORE OF THE SATURN PLASMA SHEET

by

Jean Michi Yoshii

A Dissertation Presented to the
FACULTY OF THE USC GRADUATE SCHOOL
UNIVERSITY OF SOUTHERN CALIFORNIA
In Partial Fulfillment of the
Requirements for the Degree
DOCTOR OF PHILOSOPHY
(AEROSPACE ENGINEERING)

December 2011

Dedication

This dissertation is dedicated to Dr. Lena Valavani, who convinced me that graduate school was possible. Although this journey was very much more 1.0D0 steps forward, 2.0*RAND() steps back than 1000 miles directly forward, I would not have taken the first step at all without her encouragement.

Acknowledgements

I would like to thank my committee members for their advice and support. I am particularly indebted to my advisor, D. Shemansky, for his patience and guidance.

Heartfelt thanks to my coworkers at SET for sharing their data, technical and editorial advice, and encouragement.

To my family, who have never given up on me and would not let me give up, many thanks and (hopefully) fewer worries now.

For so many things (letting me blow off steam, keeping the Ohrwürmer at bay, helping me keep what sanity I have left, ... but mostly just putting up with me), I owe the Nanka Kyudo Kai, R. Beal, and G. Geiger a huge debt of gratitude.

Profound thanks to composers G. Puccini, R. Wagner, and R. Strauss and their brilliant interpreter, B. Nilsson, who made the slog much more tolerable. I am sure my neighbors will be delighted not to hear *Der Ring des Nibelungen*, *Turandot*, and, especially, *Elektra* blasting away late into the night as often.

Table of Contents

List of Tables

List of Figures

Abstract

This dissertation presents a gas phase water chemistry model of the inner Saturn magnetosphere. Detailed calculations of the plasma sheet electron energy balance establish, for the first time, a direct relation between the forcing energy deposition into the plasma sheet and the state of the ambient plasma sheet electrons.

The two-part model comprises a chemistry code and an energy balance calculation. The chemistry code, coreqg.f90, iteratively solves chemistry rate equations for the thirteen ion and neutral species (H_2O, H_2O^+, H, H^+, O, O^+, H_2, H_2^+, O_2, O_2^+, OH, OH^+, and H_3O^+) included in the system. The water chemistry architecture file used by coreqg.f90 completely describes each reaction by specifying the reactant and product species and supplying the collision strength data used to calculate rate coefficients for the chemistry. The input parameter space for the code consists of the number densities and temperatures for the plasma sheet electrons, the heterogeneous electrons, and the selected source species, H_2O and H.

The energy balance calculation operates on the chemistry code outputs and determines the net energy rate for the plasma sheet electrons. Curves for the net plasma sheet electron energy rate vs. input plasma sheet electron temperature, as a function of heterogeneous electron density, are presented. Energy equilibrated plasma sheet electron temperature and gas species partitioning are determined at net zero plasma sheet electron energy rate.

The role played by the Saturn atmospheric heterogeneous hydrogen in maintaining the observed neutral-dominated magnetospheric gas is investigated. The water source rate and energy deposition rate required to maintain the gas at the location of Enceladus (4 Saturn radii (R_s) from Saturn center) are evaluated. Energy relaxation lifetimes for neutral and ion gas species are also determined. Comparison of the model against observation shows basic agreement for the core of the plasma sheet.

The chemistry code input and output files used in the data analysis and plots in this dissertation (plasma sheet electron densities = 50.0, 75.0, and 100.0 cm^{-3}) are archived as supplementary files.

Chapter 1

Introduction

At present, the Saturn magnetosphere is not well understood. As a gas giant, Saturn was expected to have a plasma-dominated magnetosphere similar to that of Jupiter, based on the Voyager observations and theoretical considerations during that epoch. The presence of satellites with significant atmospheres at both planets (Io at Jupiter and Titan at Saturn), readily losing gas to the magnetosphere environment, suggested that the Saturn magnetosphere should bear similarities to Jupiter. The Voyager epoch ended with the conclusion that the Saturn magnetosphere was similar to the Jupiter magnetosphere, albeit on a much smaller scale in energy and density, according to models developed by Richardson and Eviatar ([79] and later papers through 1992).

This conclusion was countered by the claim, based on the Voyager Ultraviolet Spectrograph Experiment (UVS) results, that the Saturn magnetosphere contained a large concentration of broadly distributed neutral H gas [9], [81]. In work by Shemansky and Hall [93], a large abundance of OH was found using the Hubble Space Telescope (HST) [95]. The Saturn magnetosphere is now understood to contain predominantly neutral gas (mainly H_2O, H, OH, and O with a neutral/ion density ratio as high as ~ 300, in strong contrast to a value of ~ 0.003 at Jupiter) whose populations can vary on short time scales [20].

The known, substantial sources of neutral gas do not adequately explain the observed, dynamic environment of the Saturn system. The energy required to produce and maintain the gas in its presently observed broad spatial distribution, and the physical chemistry responsible for partitioning of the gas's species, need to be examined in sufficient detail to develop a first order understanding of the system. In particular, the role that hydrogen coming off the top of the Saturn atmosphere plays in the chemistry of the inner magnetosphere has not previously been explored. Population changes observed on a time scale of weeks have not been explained.

The purpose of this dissertation is to investigate the physical chemistry of the Saturn magnetosphere to explain the basic physical processes that control the system.

1.1 Current knowledge of the Saturn magnetosphere

The Saturn system includes a significant ring system, six major satellites (Mimas, Enceladus, Tethys, Rhea, Dione, and Titan), and a number of smaller satellites. The magnetosphere can be divided into an inner region (McIlwain's parameter[17] $L \lesssim 12$), which contains all of the major satellites except Titan, and an outer region. The magnetospheric plasma is weakly ionized everywhere within and beyond the bow-shock region. The neutral gas is composed mainly of HI (atomic hydrogen), OI (atomic oxygen), OH, and H_2O. Figure 1.1 shows the relative locations of the main satellites and the neutral gas, and Table 1.1 lists the positions of major bodies in the Saturn system.

Table 1.1. Saturn System from Titan inward

Body	location[a] , R_s[b]
D ring	1.11 (inner edge)
C ring	1.2348 (inner edge)
Maxwell Gap	1.45
B ring	1.52 – 1.9477
A ring	2.02 – 2.2670
F ring	2.3267 (center)
G ring	2.8 (center)
E ring	3 – 8
Mimas	3.08
Enceladus	3.95
Tethys	4.88
Dione	6.26
Rhea	8.73
Titan	20.3

[a][a] Esposito et al.[22]; Morrison et al.[69].

[b]1 R_s = 1 equatorial Saturn radius = 60268 km.

For this dissertation, the region of particular interest within the inner magnetosphere is the E ring region in the vicinity of the satellite Enceladus. The E ring is a tenuous and diffuse ring of small ($\sim \mu$m-sized), icy particles lying between 3 and 8 R_s (1 R_s = 1 Saturn radius = 60268 km), outside the main (A, B, and C) rings and the F and G rings. Five of the major satellites lie within the E ring: Mimas, Enceladus, Tethys, Dione, and Rhea.

1.1.1 Magnetospheric observations

Much of the Saturn data were obtained by the Pioneer, Voyager, and Cassini spacecraft and the Hubble Space Telescope. Pioneer 11 supplied the first *in situ* observations of

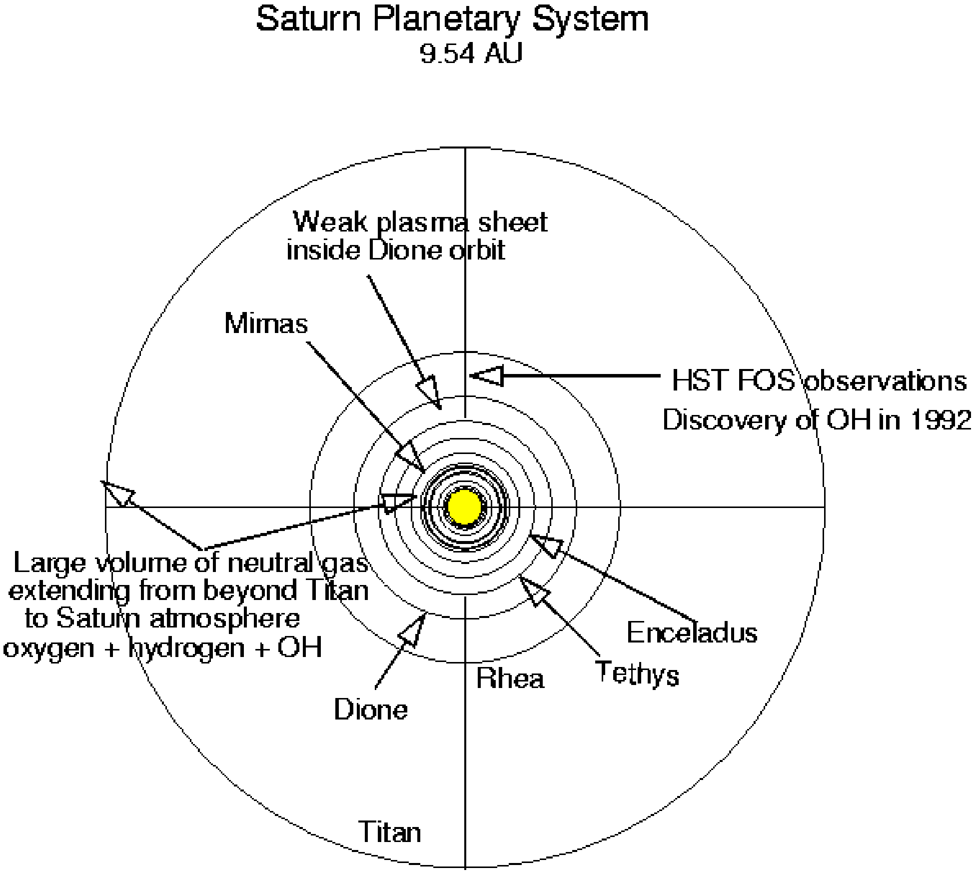

Figure 1.1 North polar view of the Saturn system to Titan orbit.
Saturn and its main rings appear at the center of the diagram. The orbits of the major E ring satellites Mimas (3.08 Saturn radii), Enceladus (3.95 R_s), Tethys (4.88 R_s), Dione (6.26 R_s), and Rhea (8.73 R_s) are shown. The core of the inner plasma sheet lies just outside the orbit of Enceladus (c.f. Figure 1.11). Neutral H fills the system in a local time dependent distribution (see Figures 1.4 and 1.3) extending beyond 45 R_s, beyond the orbit of Titan (20.3 R_s). Water product neutrals are distributed in the inner region (c.f. Section 1.1.3 and Figures 1.5 through 1.10). The distance from the Sun labelled in the figure, 9.54 AU, is from ca. 1980; the Sun-Saturn distance at the time of the cited Cassini observations in 2004 and 2005 was 9.04 AU.

the planetary magnetic field. Using Pioneer 11 and Voyager 1 and 2 magnetometer data, Acuña et al. derived a field model [1] with a magnetic dipole aligned nearly perfectly with the planetary rotational axis and displaced northward by 0.04 – 0.05 R_s (Saturn radii – 60,280 km) and small quadrupole and octupole terms. Other Voyager instruments of interest are the plasma science experiments (PLS), which measured electrons and ions in the energy range of 10 – 5950 eV; the low-energy charged particle (LECP) instruments, which measured electrons with energies $\geq$ 26 keV and ions with energies $\geq$ 40 keV; and the ultraviolet spectrometers (UVS), which observed emissions and extinctions in the 500 – 1700 Å wavelength range [8]. More recently, the ESA space observatory Herschel has observed magnetospheric water[35].

On Cassini, the instruments of particular interest are the Ultraviolet Imaging Spectrograph (UVIS) [19], the Cassini Plasma Spectrometer (CAPS) [117], and the Ion Neutral Mass Spectrometer (INMS) [112]. Data from the Visible and Infrared Mapping Spectrometer (VIMS) [11] and, for particles abovve 10 keV, the Magnetospheric Imaging Instrument (MIMI) [57] are also of interest.

The scientific objectives for UVIS include observations of the Saturn and Titan atmospheres and the ring structure and composition; measurment of magnetospheric neutrals; and determination of the size and distribution of dust particles in the rings [21]. UVIS consists of an EUV spectrograph covering wavelengths of 56–118 nm, an FUV spectrograph covering the 110–190 nm range, a high-speed photometer (HSP) with a spectral response covering the range 115–190 nm, and a hydrogen-deuterium absorption cell (HDAC) designed to determine relative hydrogen and deuterium abundances from Lyman-α emissions[19].

Data collected by CAPS include the energies and densities of ions and electrons, with the objective of studying the composition and dynamics of the magnetosphere[117]. The electron spectrometer operates over an electron energy range of 0.6 eV to 30 keV, while the ion mass spectrometer measures energies from 1 eV to 50 keV. The ion beam spectrometer determines the electrical charge of ions.

Among the objectives of INMS are the measurement of ion and neutral species composition in the magnetosphere and the study of interactions between rings and satellites and the magnetosphere [112]. However, the instrument's science goals mostly target Titan and its data may be of limited use for magnetospheric modelling.

In addition to studying the structure and composition of the rings, VIMS is used to examine the composition of icy satellite surfaces, and the structure and behavior of the Saturn and Titan atmospheres [12]. The two channels, a visible and near-infrared channel (VIMS-VIS) covering 0.3–1.05 μm and an IR channel (VIMS-IR) covering 0.85–5.1 μm, both provide spectral data. The imaging capabilities of VIMS are used to map the spatial distributions of surface constituents of icy satellites [11].

MIMI studies the energetic particle environment at Saturn [57]. Its Low Energy Magnetospheric Masurement System (LEMMS) measures ion and electron fluxes with energies ranging from 20 keV to 130 MeV, while the Ion and Neutral Camera (INCA) images ions and the energetic neutral atoms (ENA) formed by charge exchange between ions and the ambient neutral gas. Among the scientific objectives of MIMI are a study of magnetosphere-ring and magnetosphere-satellite interactions; the effects of plasma and radiation bombardment on the icy surfaces of satellites and ring particles; and, through ENA imaging, the configuration and dynamics of magnetospheric plasma.

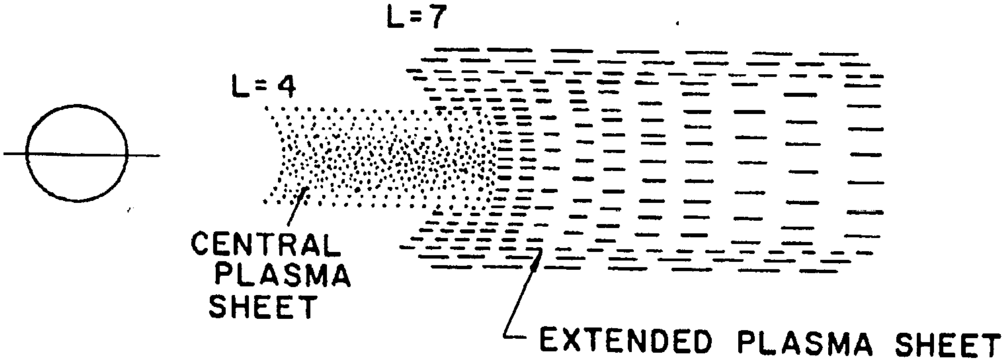

Figure 1.2 Schematic of Saturnian plasma sheet configuration.
The Voyager PLS observations observed an inner plasma torus and an outer plasma sheet. The inner plasma torus lay between L-shells 4 and 8 (corresponding roughly to the location of Enceladus and just inside Rhea, in the equatorial plane). Its radial density profile was flat, and the density dependence on the azimuthal coordinate Z was Gaussian with a root-mean-square width of 0.93 R_s. The extended plasma sheet had a distinct inner edge at L$\sim$7 was detected out to at least L$\sim$17 (somewhat inward of Titan). Its radial density dependence was also flat, while the azimuthal density profile was flat up to $|Z| \sim 1.8$ R_s before decreasing with a scale height of 0.24 R_s. The figure is from Bridge et al.[7]. Reprinted with permission from AAS.

1.1.2 Voyager era understanding

The inner magnetosphere contains a low density, low energy, corotating plasma and a more tenuous, high-energy plasma comprised of particles trapped in the radiation belts. The radiation belt particles generate the ring current by undergoing $\nabla \times \vec{B}$ drift.

The main features observed by PLS were an inner plasma torus between L-shell$\approx$4 and L$\approx$7 and an extended plasma sheet detected from an inner edge at $\sim$7 R_s out to at least $\sim$17 R_s (Figure 1.2). The extended sheet had a nearly flat distribution, independent of L and independent of Z, the azimuthal coordinate, up to $|Z| \sim 1.8$ R_s, then falling off with a scale height of 0.24 R_s[7]. The distribution of the inner torus was also flat radially; its azimuthal density profile was a Gaussian with a root-mean-square width of 0.93 R_s.

From $\sim 4 - 4.5\ R_s$ inward to the Voyager 2 ring crossing at $2.73\ R_s$, the electrons were too cold to be measured reliably by PLS. The (now known to be) high concentrations of neutrals in the magnetosphere are responsible for cooling the electrons.

A study of the Voyager 1 PLS electron data indicated a depletion of 30 – 6000 eV electrons between $8.4\ R_s$ inbound and $6.7\ R_s$ outbound, suggesting interaction between the local thermal plasma and particulate matter[98]. An additional reduction in suprathermal electrons in the vicinity of Enceladus was attributed to dust enhancement. The removal of suprathermal electrons by the E ring was suggested as a mechanism for collapsing the inner plasma torus: the extinction of suprathermal electrons greatly reduced the extent to which electrons were able to travel azimuthally, weakening the polarization electric field available to pull ions off the equatorial plane.

Higher energy particles (electron energies $\gtrsim$22 keV, ion energies $\gtrsim$28 keV) were found to play only a minor role, as the Voyager LECP instruments measured densities which were very small compared to those of lower energy ions and electrons or, for that matter neutrals, e.g. densities varying from a maximum of about 2×10^{-2} cm^{-3} near Dione to 3×10^{-4} cm^{-3} near Titan for particles with energies $\gtrsim$40 keV[56]. Ion fluxes above the interplanetary levels were not detected in the energy range above $\sim$2 MeV.

Magnetosphere models in the Voyager era calculated low densities for both ions and neutrals. The densities of individual species were typically on the order of 1 to 10 cm^{-3} for H^+, heavy ions (usually assumed to be O^+ and/or OH^+, but sometimes including H_2O^+), H, and O (and/or OH) at 5 R_s[95]. Total heavy neutral species source rates were on the order of 10^{26} s^{-1}. Like the observations, the models generally did not distinguish between the heavy ion species.

1.1.3 The OH controversy and unexplained dynamism in the inner magnetosphere

A controversy over the neutral populations arose when Shemansky and Hall[93] published Voyager UVS observations indicating that H Ly α emissions increased radially inward toward Saturn. The mosaic scan conducted during days of year 324 to 343 in 1980 (Figure 1.3) showed higher emissions (in the plot, darker shdaing) in the vicinity of Saturn compared to regions farther away (lighter shading). The Saturn atmosphere was suggested as the source of the gas, as the Titan hydrogen torus could not supply hydrogen inside $\sim$8 R_s and the sunlit Saturn atmosphere was a viable candidate for the local-time nonuniform (Figure 1.4) source of the emissions, which occurred consistently on the dayside of the sun-Saturn line. The emission structure visible in the figure was independent of Saturn's rotation period (10 hr 39 min) and was seen throughout the twenty days of the observation. Electron impact dissociation of H_2 in the exosphere, which would produce atomic hydrogen energetic enough to populate the magnetosphere, was the suggested mechanism.

The Shemansky and Hall analysis indicated that rather than a torus sourced by Titan with a cavity inside 8 R_s, the atomic hydrogen instead formed an extended distribution which continued outward from the top of the Saturn atmosphere. Water products would be expected to dominate near the equatorial plane in the inner magnetosphere, with number densities considerably higher than the ones in plasma models required to balance the energy budget. The Shemansky and Hall model yielded typical values of [O] $\sim$ 400 cm^{-3}, [H] $\sim$ 130 cm^{-3}, [OH] $\sim$ 40 cm^{-3}, and [H_2O] $\sim$ 20 cm^{-3}, with [O^+] $\sim$ 30 cm^{-3}

and $[H^+] \sim 3$ cm^{-3}, with a total heavy neutral source rate of 28×10^{26} s^{-1}, an order of magnitude higher than in previous magnetosphere models.

The presence of large neutral densities in the inner magnetosphere was confirmed by observations made in 1992 using the Faint Object Spectrograph (FOS) on the Hubble Space Telescope[95]. The results of those observations and subsequent ones in 1994 and 1996[87] are summarized in Figure 1.5, a plot of OH abundance as a function of radial position, and Figure 1.6, which plots total neutral and OH densities against radial position. The listed density of OH, which peaked at 160 cm^{-3} at 4.5 R_s, was based on a reaction rate which was a factor of 10 too slow; revised estimates were 600 – 1000 cm^{-3}. The inferred amount of neutral O was equal to the amount of OH.

1.1.4 Cassini results

Cassini has been orbiting Saturn since the Saturn Orbit Insertion (SOI) in July 2004. Early results from the Cassini mission include magnetospheric ion concentrations measured during the approach to Saturn and orbital insertion. In the E ring region, CAPS measurements of proton populations range from 0.5 to 5 cm^{-3} with energies of 1 – 10 eV and water group ion (OH^+, H_2O^+, H_3O^+, and O^+, collectively referred to as W^+) populations range from 1 to 30 cm^{-3} [99], with energies of 2 – 100 eV and O^+ outnumbered by the other W^+ species by a factor of 2 [116]. These ion densities are comparable to earlier ion density measurements[25]. CAPS data also indicate the presence of N^+ [101] within ~1 R_s vertically off the orbital plane in the E ring region. The ratio of N^+ to W^+ is consistent with Enceladus as the source of the N^+ [100].

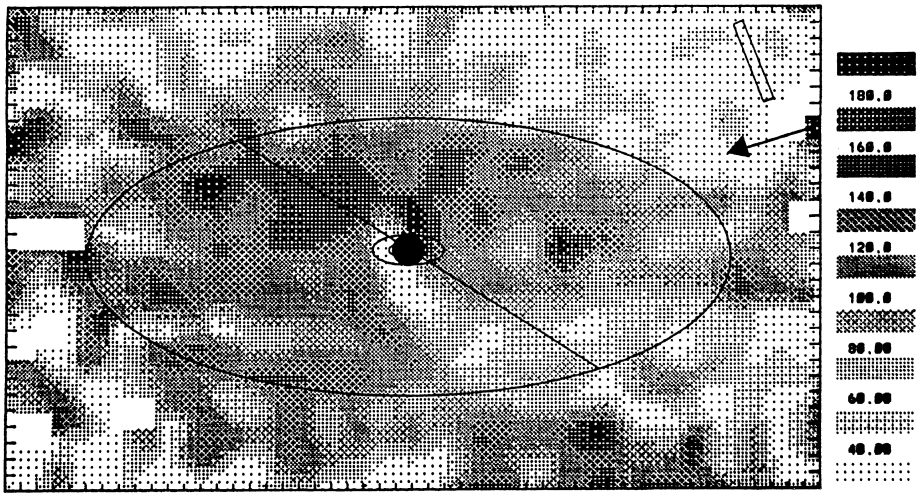

Figure 1.3 Half tone plot of Saturn system H Ly α emission from Voyager 1 UVS data.

This mosaic scan was conducted over days of year 324 to 343 in 1980, with a total integration time of 126 hours. The scale at the right of the plot gives the brightness of the H Ly α (1216 Å) emission in Rayleighs. The pixel size is 1 R_s x 1 R_s perpendicular to the instrument boresight, corresponding to 1 R_s x 2.4 R_s when projected onto Saturn's equatorial plane. At the time, the Voyager 1 orbit had an inclination of 26°. Saturn and its main rings are drawn to scale; the large ellipsoid represents Titan's orbit. The arrow at the upper right of the plot indicates the Sun-Saturn line, while the rectangular box shows the mean size and orientation of the instrument field of view. The diagonal line from upper left to lower right marks Saturn's terminator. Local interstellar medium background and stellar emissions were subtracted. Shemansky and Hall attribute the bright spot at the right ansa of Titan's orbit (near the right center edge of the plot) to imperfect correction of a stellar source, and the bright patches near the edges of the figure to lower integration times and poorer signal to noise ratios.

The main features of the H Ly α emission are the confinement of the brightest regions inside the orbit of Titan and its asymmetry, with a maximum roughly at Saturn's dusk terminator (upper left sector of Saturn) and a minimum at the pre-dawn region (lower right sector of Saturn). If a Titan hydrogen torus were the sole source of the H Ly α emission, maximum emission regions would be expected at the right and left ansae of Titan's orbit (toward the left center and right center edges of the plot) and the minimum emission region would be in the vicinity of Saturn. An emission source well inside Titan's orbit must therefore be present. The emission structure is independent of Saturn's rotation. The figure is from Shemansky and Hall[93].

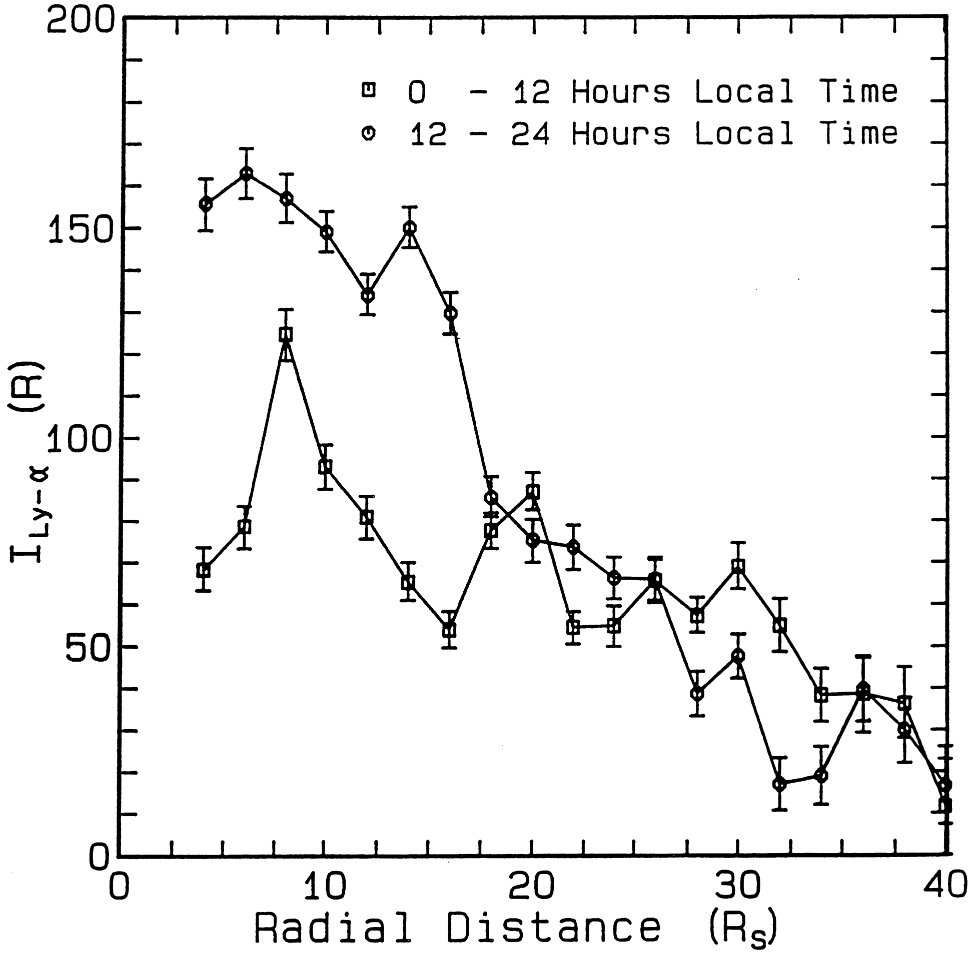

Figure 1.4 The local time dependence of the radial distribution of H Ly α at Saturn. The H Ly α emission data from the mosaic scan in Figure 1.3, averaged over local time. The squares represent data from the solar regions (local time of 0 to 12 hours) while circles are data from the antisolar regions (local time of 12 to 24 hours). The peak near 20 R_s in the 0 to 12-hour local time data is attributed to the Titan H source. Inside the Titan orbit, the dusk side H Ly α emission is brighter than the dawn side emission. The overall increase in emission with decreasing distance from Saturn suggests Saturn is the source of the H. The nonuniformities in the emission suggest a distribution of H with complex radial and azimuthal variations rather than an axially symmetric torus or disk. From Shemansky and Hall[93].

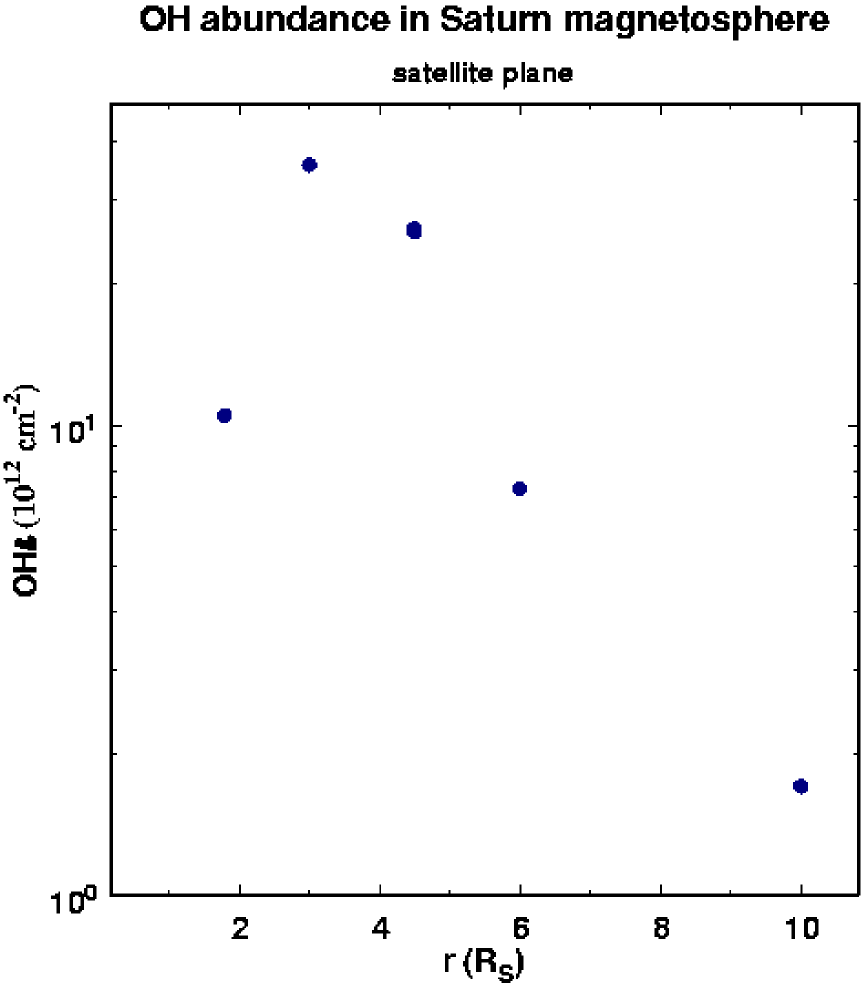

Figure 1.5 OH abundance in the Saturn magnetosphere as a function of radial position.
OH abundances in Saturn's satellite plane, from the 1992 Hubble Space Telescope Faint Object Spectrograph observations by Shemansky et al.[95]. Observations were made on the astronomical west side of the planet, corresponding to dusk local time. The peak at 3–4 R_s suggests a source of water, the precursor species of OH, near Mimas (3.08 R_s) and/or Enceladus (3.95 R_s). The dropoff in abundance beyond 4 R_S suggests the other major E ring satellites, Tethys, Mimas, and Rhea, are not significant contributors of H_2O. The figure is from Shemansky[87].

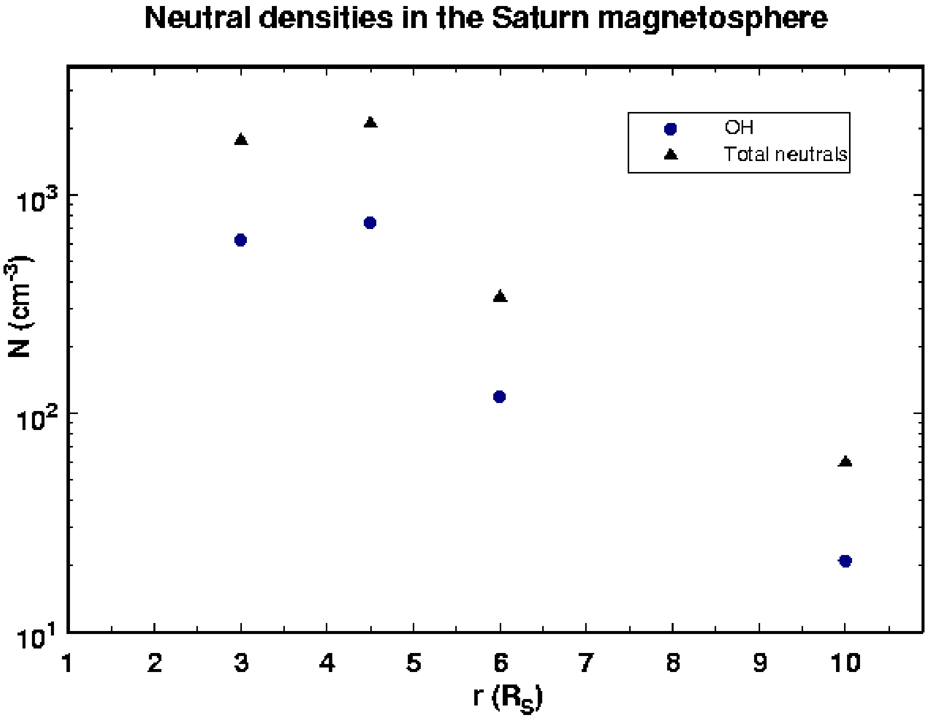

Figure 1.6 Total neutral density and OH density in the Saturn magnetosphere, as functions of radial position.

The data are from the Shemansky et al.[95] Hubble Space Telescope observations of 1992. Local time as in Figure 1.5. The peak densities of 2000 cm^{-3} for total neutrals and 800 cm^{-3} for OH are near 4.5 R$_s$. The total neutral and OH densities drop off rapidly outside of 6 R$_s$. Inward of the peak, the densities are still relatively high at 3 r$_s$, which could suggest a narrow (∼1 R$_s$ radius) torus centered near 4–4.5 R$_s$, i.e. near Enceladus. The figure is from Shemansky[87].

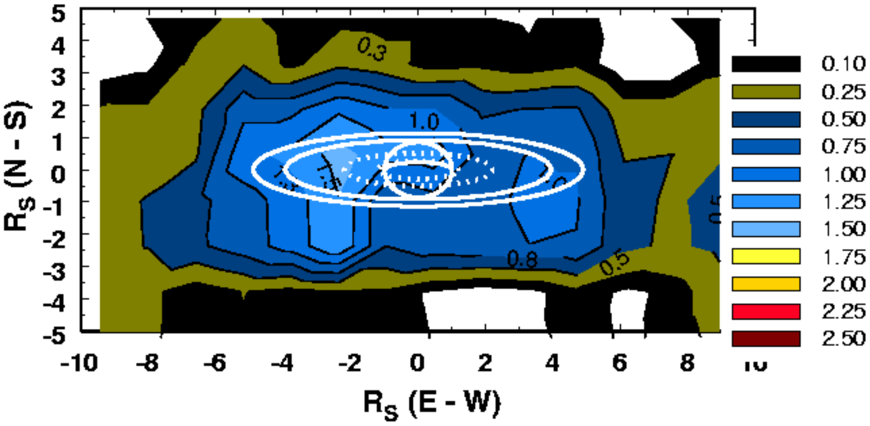

Figure 1.7 Cassini UVIS image of pre-SOI Saturn magnetosphere atomic oxygen emission from 2003 DOY 356 through 2004 DOY 11.

Atomic oxygen 1304 Å emission obtained between 31 December, 2003 and 11 January, 2004. The spacecraft range was 90 – 83 Mkm. The brightness scale to the right of the plot is in Rayleighs. The image pixels are 1.4 R_s x 1.4 R_s. The origin of the plot is the Saturn center, and east-west and north-south distances are in R_s. Saturn and its equator are outlined by solid white lines and the main rings by the dotted white lines; the orbits of Enceladus (3.95 R_s) and Tethys (4.88 R_s) are superimposed. The Sun is on the west (right) side of the figure. The brightest 1304 Å emission is on the dark (left) side of Saturn, with a peak of 1.5 Rayleighs between 1 and 3 R_s. The figure is from the Supporting Online Material for Esposito et al.[20]. Reprinted with permission from AAS.

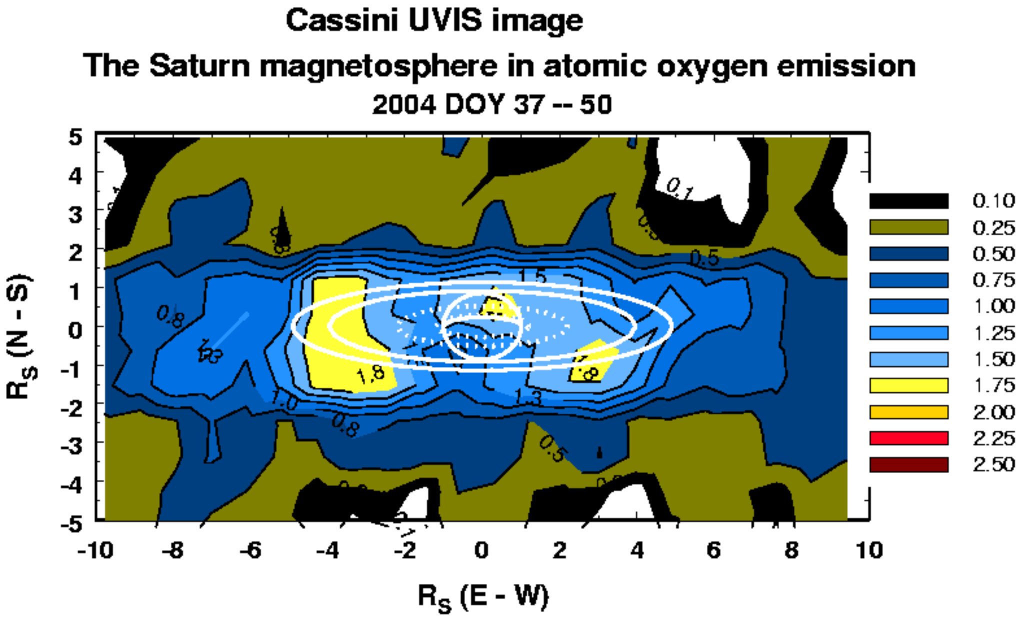

Figure 1.8 Cassini UVIS image of pre-SOI Saturn magnetosphere atomic oxygen emission from 2004 DOY 37 through 2004 DOY 50.

Atomic oxygen 1304 Å emission obtained between 6 February and 19 February, 2004. The spacecraft range was 71 – 65 Mkm. The brightness scale to the right of the plot is in Rayleighs. The image pixels are 0.9 R_s x 0.9 R_s. The origin of the plot is the Saturn center, and east-west and north-south distances are in R_s. Saturn and its equator are outlined by solid white lines and the main rings by the dotted white lines; the orbits of Enceladus (3.95 R_s) and Tethys (4.88 R_s) are superimposed. The Sun is on the west (right) side of the figure, and the spacecraft viewing geometry is the same as in the earlier plot, Figure 1.7. The peak brightness has increased to 1.8 Rayleighs, compared to 1.5 Rayleighs in the earlier observation. The darkside (left side) peak emission region has expanded in size and has moved outward to $\sim$2.5 to 4 R_s (compared to 1 to 3 R_s in the earlier plot). A somewhat smaller peak emission region has appeared on the dayside (right side); the distribution of the emission more closely resembles a torus than in the earlier plot. The figure is from the Supporting Online Material for Esposito et al.[20]. Reprinted with permission from AAS.

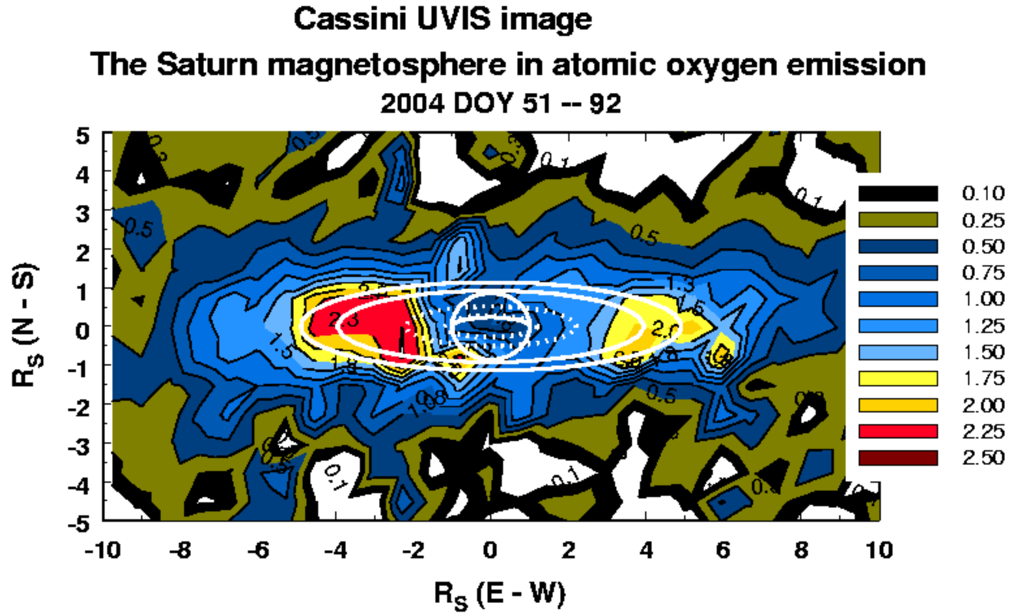

Figure 1.9 Cassini UVIS image of pre-SOI Saturn magnetosphere atomic oxygen emission from 2004 DOY 51 through 2004 DOY 92.
Atomic oxygen 1304 Å emission obtained between 20 February and 01 April, 2004. The spacecraft range was 64 – 45 Mkm. The brightness scale to the right of the plot is in Rayleighs. The image pixels are 0.75 R_s x 0.75 R_s. The origin of the plot is the Saturn center, and east-west and north-south distances are in R_s. Saturn and its equator are outlined by solid white lines and the main rings by the dotted white lines; the orbits of Enceladus (3.95 R_s) and Tethys (4.88 R_s) are superimposed. The Sun is on the west (right) side of the figure, and the spacecraft viewing geometry is the same as in the earlier plots. The size of the darkside (left side) peak emission region is smaller than in early February (previous figure, Figure 1.8), but the peak emission has increased to 2.3 Rayleighs (compared to 1.8 Rayleighs). The peak emission region now extends out to 5 R_s. On the dayside (right side), the brightness remains lower than on the darkside; while the distribution of the emission is still a torus, the asymmetry is greater than it was earlier. The figure is from the Supporting Online Material for Esposito et al.[20]. Reprinted with permission from AAS.

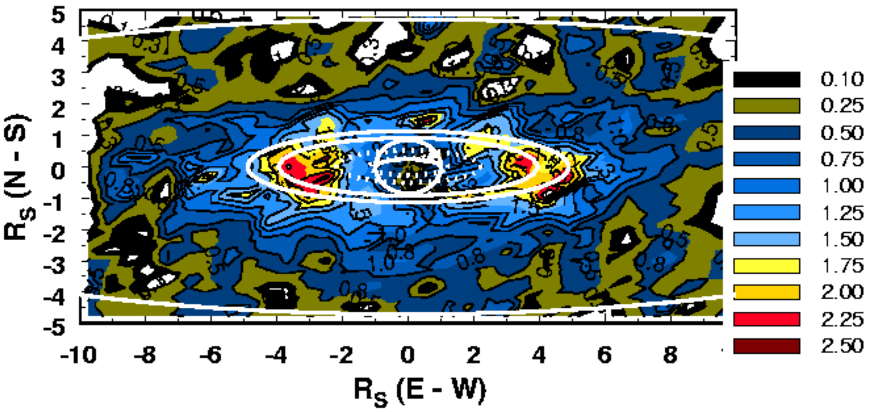

Figure 1.10 Cassini UVIS image of pre-SOI Saturn magnetosphere atomic oxygen emission from 2004 DOY 93 through 2004 DOY 133.

Atomic oxygen 1304 Å emission obtained between 02 April and 12 May, 2004. The spacecraft range was 45 – 28 Mkm. The brightness scale to the right of the plot is in Rayleighs. The image pixels are 0.42 R_s x 0.42 R_s. The origin of the plot is the Saturn center, and east-west and north-south distances are in R_s. Saturn and its equator are outlined by solid white lines and the main rings by the dotted white lines; the orbits of Enceladus (3.95 R_s) and Tethys (4.88 R_s) are superimposed. The Sun is on the west (right) side of the figure, and the spacecraft viewing geometry is the same as in the earlier plots. Although the peak emission remains unchanged at 2.3 Rayleighs, the sizes of the brightest regions continue to decrease compared to the previous two months (Figures 1.8 and 1.9). The asymmetry of the distribution is lower than in the previous month. The figure is from the Supporting Online Material for Esposito et al.[20]. Reprinted with permission from AAS.

UVIS data indicate large and relatively rapid (occurring on time scales on the order of weeks) variations in the atomic oxygen population[20]. In particular, an event which occurred between the UVIS observation window ending 11 January 2004 and the window beginning on 06 February appears to have injected into the magnetosphere a mass of atomic oxygen comparable to the mass of micron-sized E ring particles. The increased OI 1304 emission from the injected oxygen is absent in the image from the 11 January window (Figure 1.7), but manifests as the large bright areas in the image from the 06 February window (Figure 1.8). Figure 1.9 shows the oxygen emission in the next window, which started on 20 February; here, the peak emission has increased from the 06 February window but the overall size of the emission object is smaller. In the next window, which started on 02 April, the peak brightness remains approximately the same but the emission object is smaller (Figure 1.10). It is worth noting that the resolution of these plots improves from 1.4 R_s x 1.4 R_s to 0.42 R_s x 0.42 R_s over the course of the observations.

The transient OI population of the surge decayed within two months, implying a loss rate high enough to deplete the E ring over 100 million years in the absence of a source of ring particles to regenerate the ring. The physical processes by which such a large implied influx of H_2O could be produced are as yet unidentified, and the chemical processes which could remove OI at such a high rate have yet to be determined. The recently discovered plume at Enceladus ([31] and others) is a major source of water products in the magnetosphere.

More recently, Schippers et al. [82] combined CAPS and MIMI data to derive electron populations and energies in the inner magnetosphere. In the E ring region, cold electron temperature and density data range from $\leq$1 eV and $\sim$100 cm^{-3} (extrapolated) at 4 R_s

(vicinity of Enceladus) to ~10 eV and ~10 cm^{-3} near 9 R_s, while the corresponding data for hot electrons range from 100 eV and ~0.01 cm^{-3} (extrapolated) at 4 R_s to 1 keV and ~4 cm^{-3} near 9 R_s. One caveat is that the Schippers et al. *in situ* data are derived from a single orbit and their statistical uncertainty is large. Sittler et al.[97] used CAPS and radio and plasma wave science (RPWS) data to produce 2D (in equatorial radius and azimuthal distance) contour plots for H^+ and W^+ densities, from which the plasma sheet electron density is inferred. Figure 1.11 shows their W^+ contour plot. The heavy ions are confined near the equatorial plane, in contrast to the protons which reach higher latitudes. The W^+ and plasma sheet electron densities are $\gtrsim$50 cm^{-3} at 4 R_s. The Sittler et al. plasma sheet electron density map shows the basic structure of the core of the plasma. An updated schematic of the Saturn magnetosphere is in Figure 1.12.

UVIS system scans confirm the presence of a broad (extending beyond 40 R_s in the equatorial plane) H distribution whose intensity increases with decreasing distance from Saturn, consistent with a source at the top of the atmosphere [94], [67], shown in Figure 1.13. The system scan data indicate O forms a broad torus whose center position is not fixed but rather ranges around 4±1 R_s. The azimuthal extent of the brightest OI 1304 Å signal region is up to ~0.4 R_s off the ring plane. The OI emission has a significant intensity (up to 30 percent of the peak intensity) out to 10 R_s radially and up to 5 R_s azimuthally. A concurrent reanalysis of the HST OH data showed the distribution of OH is half as broad as that of O and also centered near 4 R_s. The rapid fall-off of OH intensity away from 4 R_s is consistent with a source at Enceladus. The slow fall-off of the O distribution indicates its sourcing is different than that of the OH.

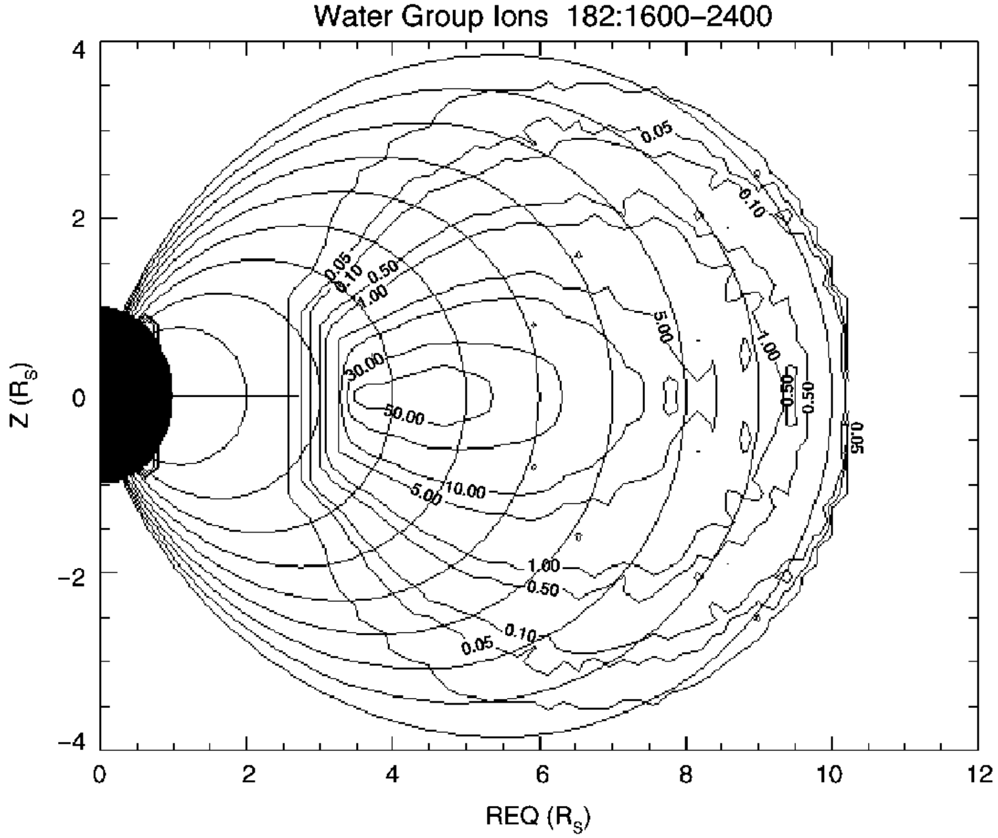

Figure 1.11 2D contour plots of water group ion density from CAPS and RPWS observations.

Total density of water group ions W^+ (O^+, OH^+, H_2O^+, and H_3O^+) as a function of equatorial radius R_{EQ} and azimuthal coordinate Z; distance scales are in Saturn radii (R_s). The smooth, round contours are the dipole magnetic field lines. Units for the density contours are ion cm^{-3}. The W^+ are confined near the equatorial plane out to L shell 10. The peak heavy ion density $\gtrsim$50 cm^{-3}, and the highest density region extends between 3 and 5.5 Rs radially and up to $\sim$0.4 Rs azimuthally. Enceladus is near the center of the peak W^+ density region. Reprinted from Sittler et al.[97] with permission from Elsevier.

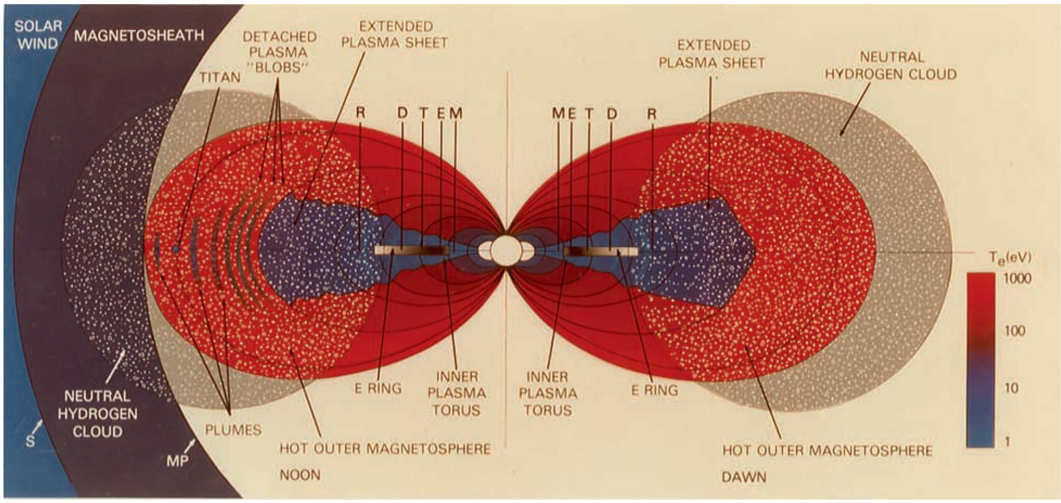

Figure 1.12 Updated schematic of the Saturn magnetosphere based on Cassini observation.
Saturn and its main rings appear at the center of the diagram. The E ring is the gray shaded rectangular region which lies radially outward from the main rings. The letters (M, E, T, D, and R) indicate the positions of the major E ring satellites (Mimas, Encelauds, Tethys, Dione, and Rhea, repsectively). The temperature scale in the lower right corner of the figure indicates plasma electron temperatures ranging from 1 to 1000 eV. The inner plasma torus (blue region) extends out from the main rings to Rhea and contains cold electrons with temperatures below a few eV. The extended plasma sheet (purple region) extends out to about 12 R_s; the electrons have a temperature on the order of 10 eV. The electrons in the outer magnetosphere (red region), which extends beyond Titan, are hot, with temperatures up to 1 keV. A large cloud of neutral hydrogen (white dots) extends beyond the magnetopause boundary (MP), stretching well beyond the orbit of Titan. From Gombosi et al.[26].

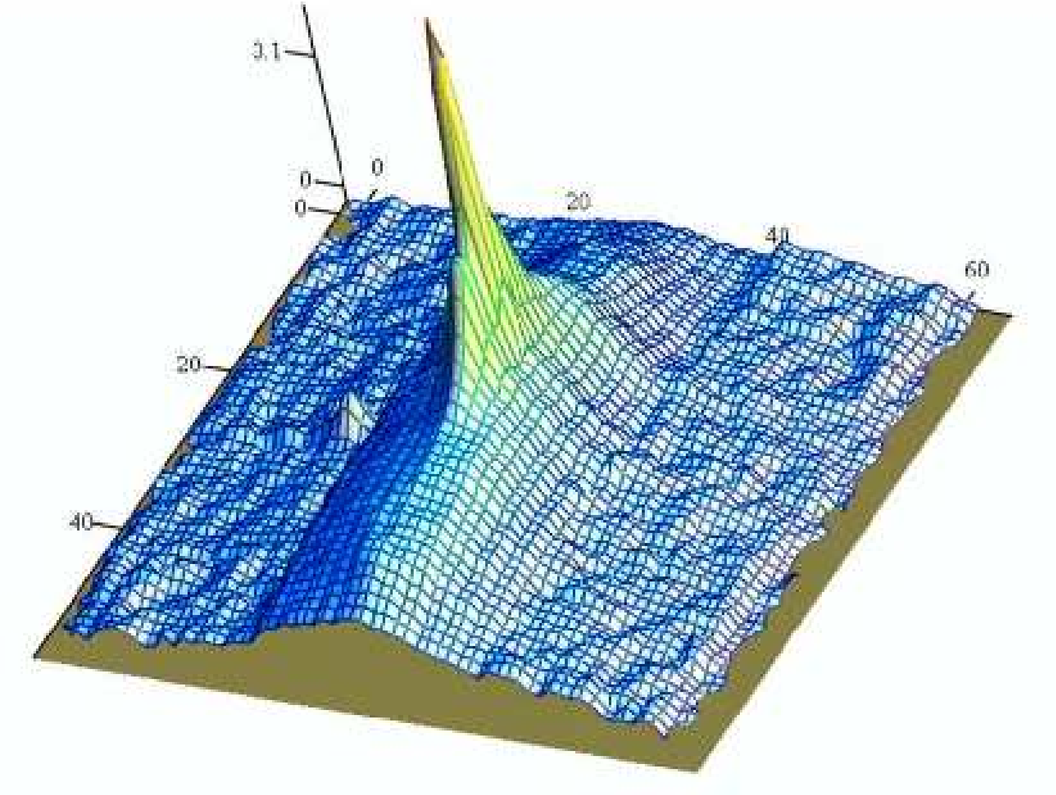

Figure 1.13 Contour plot of pre-SOI Cassini UVIS H Lyα emissions.
This 3D plot shows the extent of the atomic hydrogen in the magnetosphere from a December 2003 observation. The distance scale is in R_s, with Saturn at the center of the plot. The image extends out from Saturn to ± 30 R_s in the east-west (left-right) direction, however measurable H Ly α emissions extend beyond 45 R_s downstream from the Sun. In the north-south (in-out) direction, emissions were measured out to ± 30 r_s from the orbital plane. Saturn's orbital plane runs down the center of the 20 R_s-wide ridge at the center of the image. The intensity (vertical axis) is in arbitrary units; the brown plane marks the zero base plane. The sun is toward the top of the plot, with the sun-planet line along the equator. The small bump to the left of the ridge is on the antisolar side. The figure is reprinted from Shemansky et al.[94] with permission from Elsevier.

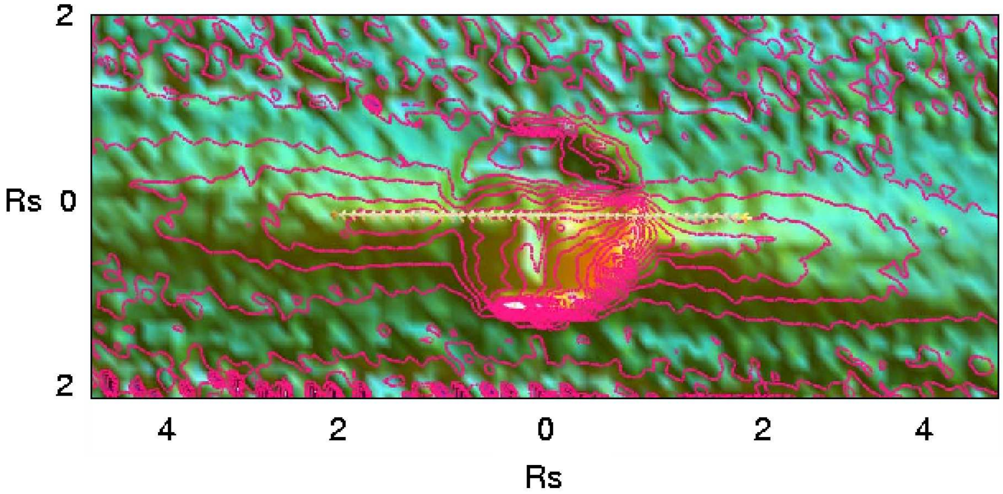

Figure 1.14 Surface contour plot of Cassini UVIS H Lyα emission data from 2005 DOY 74–86
This image shows the escape of atomic hydrogen from the top of the Saturn atmosphere. In this edge-on view of the main rings (horizontal white line at the center of the image), the pixel size if 0.1 R_s x 0.1 R_s. Spacecraft range was 24 – 44 R_s. Total integration time was 13 days. The horizontal axis shows the radial position, while the vertical axis is the azimuthal position. Both distance scales are in R_s, with Saturn center at (0,0). The sun is at the right side of the plot; subsolar latitude is -22.3°. Constant-brightness contour lines are plotted. Peak brightness is about 1100 Rayleighs. Auroral emissions are present at the poles. The distribution of the H Lyα emission is non-uniform and asymmetric, with a bright feature which extends out at an angle of 13.5 ° below the ring plane from the sunlit side of the atmosphere. The contour lines that outline the feature lie at latitudes below the south polar auroral ellipse; atomic hydrogen escapes from this region. On the dark side, the asymmetric distribution is consistent with the presence of both orbiting and ballistic hydrogen from the thermosphere; this corroborates earlier Voyager UVS observations. Reprinted from Shemansky et al.[94] with permission from Elsevier.

One feature in the UVIS system scans is a plume-like structure in the H distribution[94]. Figure 1.14 shows this temporally persistent feature which lies at a -13.5 deg angle to the equatorial plane. The dynamics behind the formation of the plume are as yet undetermined. Notably, the broad O torus also shows a similar tilt. The overall picture painted by the system scans is that there is a steady outflow of long-lived H off the top of the Saturn atmosphere which produces the extensive hydrogen cloud; a plume of short-lived, ballistic H atoms; a well-defined OH torus sourced by Enceladus; and an O torus which has a source and/or distribution mechanism different from that of the OH torus. At 3 – 4 R_s, measured densities are 500 cm^{-3} for O and 700 cm^{-3} for OH [94].

The measured density of $[H] = 450$ cm^{-3} includes both the long-lived atoms in the atmospheric flux and the short-lived plume atoms. Both populations of H atoms pass through the magnetosphere largely unaffected by chemistry [91] and act as a forcing function for the inner magnetosphere. In the context of the present model, a forcing is an external source of gas or energy (via photons or electrons) which interacts with and influences the magnetospheric gas; any losses of the imposed gas particles, electrons, and photons are negligible and are instantaneously replaced, so the number density of particles or photons is effectively constant, and neither the particles nor the photons are resident in the magnetosphere. The Saturn H flux is large, with an estimated value of 3×10^{30} s^{-1} [94].

In the Saturn magnetosphere, the relatively large numbers of neutrals means that quenching by neutrals will determine the local plasma conditions. The plasma density is very low, and the plasma does not drive the chemistry in the magnetosphere. In contrast, at Jupiter the neutrals produced by the satellite Io ionize and undergo magnetic heating to form a plasma which far outnumbers the neutrals. The locally produced ions at Jupiter and at Saturn are accelerated by the rotating planetary magnetic field, and the gyro motion is at energies of hundreds of eV. Coulomb collisions between ions and electrons are the main heating process for the plasma sheet electrons (c.f. Section 3.1.5). The plasma sheet electrons are so much colder than the ions (typical new ion energy of $\sim$250 eV vs. electron energy $\sim$10 eV at Jupiter, $\sim$160 eV vs. less than 1 eV at Saturn) because of cooling by inelastic collisions with the neutral gas[91].

1.1.5 Modelling the magnetospheric gas environment

The magnetic field observed by Pioneer 11 and the Voyager missions has been fitted to an axisymmetric spherical harmonic model containing dipole and small quadrupole terms[1]. The magnetic dipole axis nearly aligns with the rotational axis. The magnetosphere is distorted by a ring current located between 8 R_S and 15.5 R_S. The ring current is omitted from the chemistry model as it is outside the region of interest, i.e. the E ring. As a simplifying assumption, rigid plasma corotation is assumed. The ions are too short-lived to thermalize, and the pickup energies are substantially higher than the orbital energies (at 4 R_s, the pickup energy of $\sim$160 eV for O^+ is roughly nine times the energy of an orbiting O atom). Velocity contributions to the ion energies from gyromotion phase and from the pre-ionization velocity distribution are therefore neglected, and the corotation energy is used as the ion energy when calculating reaction rates. The solar flux model used in the present work is the solar minimum model from the archive provided by Killen et al. [53].

The initial velocity and energy distributions of plasma and neutral particles are modelled as Maxwellian, using temperatures appropriate for each species. The electrons, on the other hand, have a bimodal energy distribution modeled here using two Maxwellian distributions. The cold plasma sheet electrons are locally produced by ionization processes acting on the neutral cloud. Hot heterogeneous electrons, whose energies range from 1 keV to 100 keV, form in the middle or outer magnetosphere and are transported into the inner magnetosphere [80]. Table 1.2 lists some example parameters of the Saturn magnetosphere at the locations of the HST OH measurements[95]. The Hartogh et al. [35] water abundance cited in the table is the integration of the water number density along the line of sight of the observation; no information about the spatial dependence of the H_2O density can be inferred from the abundance.

1.2 Sources of neutral gas

The major sources of water molecules and their products in the inner magnetosphere are the inner satellites and ring particles. Physical processes such as sputtering and chemical processes including irradiation remove water products from the surfaces of satellites and ring particles. The Enceladus plume is a major source of water molecules, some of which may be in the form of $(H_2O)_n$ clusters. Saturn is the major source of H. In addition, particles would be exchanged between the neutral gas and the plasma by charge exchange and chemistry. Estimates of loss rates for the neutrals (see Table 1.3) exceed calculated source rates from satellite sputtering by more than an order of magnitude.

Table 1.2. Saturn Magnetosphere Parameters

Parameter	R = 3 R_s	R = 4.5 R_s	R = 6 R_s	R = 10 R_s
orbital velocity, km s^{-1}	14.5	11.8	10.3	7.9
orbital period, s	7.8×10^4	1.4×10^5	2.2×10^5	4.8×10^5
corotation velocity[a] , km s^{-1}	29.5	44.3	59.1	98.4
e^- pickup energy, eV	0.002	0.005	0.01	0.03
H^+ pickup energy, eV	3.5	9.5	18	50
O^+ pickup energy, eV	54.7	151	281	798
magnetic field, nT	782	234	99	22
e^- Larmor radius, km	1.4×10^{-4}	1.1×10^{-3}	3.5×10^{-3}	2.5×10^{-2}
H^+ Larmor radius, km	0.4	2	6	47
O^+ Larmor radius, km	7	35	112	820
e^- Debye length, m	···	2.7	7.4	74.3
H^+ Debye length, m	···	12	38	282
O^+, Debye length, m	···	6.9	20.8	154.3
total neutral density[b] , cm^{-3}	$\sim 2 \times 10^3$	$\sim 2 \times 10^3$	300	60
OH density[b] , cm^{-3}	200	700	140	20
O density[b] , cm^{-3}	200	700	500	150
H_2O abundance[c] , 10^{13} cm^{-2}	···	1.5–1.75	···	···
escape velocity, km s^{-1}	20.5	16.7	14.6	11.2
H atom escape energy[d] , eV	2.19	1.46[e]	1.11	0.66
ion-neutral collision lifetime, s	2.9×10^5	···	···	···

[a] Planetary rotation period is 10.656 hr; sidereal period is 29.4 yr.

[b] Melin et al.[67].

[c] Hartogh et al.[35].

[d] Orbit energy is half of the escape energy.

[e] An H atom in orbit at 4.5 R_s would therefore require only an additional 0.73 eV to escape.

1.2.1 Icy satellite sputtering

Energy deposited into the icy surfaces of the E ring satellites by particles (dust, icy grains, ions, etc.) or by photons can release surface material in the form of water molecules and larger ejecta into the surrounding magnetosphere through sputtering. The yield of sputtered molecules depends on a number of factors, including the temperature and structure of the ice, the energy and type of ion, and the angle of incidence [50]. Ion gyromotion can increase the effective area for satellite sputtering [96]. The lack of reliable data leads to uncertainties in the calculated contributions of ion sputtering, dust or micrometeoroid sputtering, and photosputtering.

The velocity distribution of water vapor produced by meteoroid bombardment has been modelled but while laboratory measurements provide mass and energy spectra for the ejecta, the angular dependence is not available[44]; typically, a Maxwellian velocity distribution is assumed or the ejecta are fitted to a collision cascade model[39]. Once ejected, the vapor begins ballistic motion and, if not recaptured by its source, orbits Saturn. Highly eccentric orbits which distribute the vapor widely are possible. However, neutrals produced by sputtering appear to make up only part of the discrepancy between the calculated source rates and the estimated loss rates[39](see Table 1.4).

In addition to products formed directly by sputtering, astrophysical icy surfaces also play a role in molecule formation. Gas-surface chemistry is a mechanism for forming molecules such as H_2 observed in interstellar clouds[18]. Low energy (5 to 100 eV) electron-stimulated production of O_2 from water ice has been reported to be a significant process[74] in the radiation processing of icy bodies in the outer solar system. Depending on the location within the magnetosphere, icy satellite and/or ring particle surfaces may or may not be a significant source of O_2.

1.2.2 E ring grains and other icy particles

Given that satellite sputtering appears not to produce water products rapidly enough to sustain the observed neutral population, a logical step would be to consider the small icy particles which form Saturn's rings. Both physical processes, such as sputtering (considered by [49]), and chemical processes, such as desorption resulting from the injection of excess energy released during a chemical reaction, could result in the loss of molecules from grains. One advantage held by ring particles over satellites is the much larger total surface area available for the production of water products. The grains may play a role in the chemistry of the inner magnetosphere, but in this work, grain chemistry is omitted.

Based on reflectance observations, the larger ring particles in the major rings are believed to contain mostly water ice, with small amounts of sulfur compounds or silicate materials and possibly clathrate hydrates [22]. The size distribution in the A, B, and C rings and the Cassini Division ranges from sub-centimeter to several meters. In addition, there are substantial populations of millimeter and smaller particles in the A and B rings. On the other hand, the E, F, and G rings and the spokes in the B ring are believed to be dominated by micron-sized grains. The particles in the E ring are possible contributors to the large neutral populations observed in their vicinity (e.g. [95]). However, the number density of grains is quite low, peaking at around 5×10^{-3} μm or larger grains cm^{-3} near Enceladus, and falling off according to a power law with distance from the ring plane[51].

Table 1.3. Source rates required to support observed populations in the Saturn magnetosphere

Model	Species	Rate, s^{-1}
Melin et al.(2009)	O	1.3×10^{28}
Sittler et al.(2008)	H^+ and W^+ combined	10^{27}
	H_2O	2×10^{28}
Tokar et al.(2006)	H_2O (Enceladus)	3×10^{27}
Jurac and Richardson(2005)	H_2O	1×10^{28}
Shemansky et al.(2005)	O	5.3×10^{27}
	OH	2.0×10^{27}
Shemansky and Hall(1992)	H	10^{30}
Current model	H_2O	4.0×10^{27}

Table 1.4: Estimated production rates from various sources

Source	Body	Mechanism	Species	rate, s^{-1}
Shemansky and Hall (1992)	Saturn atmosphere	escape	H	10^{30}
Shemansky et al.(2009)				3×10^{30}
Ip (1997)	A ring	hypervelocity	H_2O	$1.5 - 8 \times 10^{26}$
	Enceladus	impacts by		3.7×10^{26}
	Tethys	E ring dust		7.6×10^{25}
Shi et al. (1995)	Enceladus	sputtering	H_2O	$0.03 \times 10^{26} \times (1 - 4)$
	Tethys	(plasma +		$0.28 \times 10^{26} \times (1 - 4)$
	Dione	LECP +		$0.53 \times 10^{26} \times (1 - 4)$
	Rhea	photo)		$0.32 \times 10^{26} \times (1 - 4)$
	total			$1.2 \times 10^{26} \times (1 - 4)$
	E ring	sputtering	H_2O	0.5×10^{26}
Jurac et al. (2001a)	Mimas	O^+ sputter	H_2O	0.12×10^{26}
	Enceladus	+ photosputter		0.09×10^{26}
	Tethys			$0.35 - 0.41 \times 10^{26}$

Continued on next page

Table 1.4 – Continued

Source	Body	Mechanism	Species	rate, s^{-1}
	Dione			$0.23 - 0.40 \times 10^{26}$
	total			$0.81 - 1.03 \times 10^{26}$
Jurac et al. (2001b)	E ring	net sputter	H_2O	0.45×10^{26}
Jurac et al. (2001a)	Mimas	O^+ sputter	O_2	1.6×10^{24}
	Enceladus			1.7×10^{24}
	Tethys			$6.9 - 7.9 \times 10^{24}$
	Dione			$5.2 - 5.5 \times 10^{24}$
	total			$1.5 - 1.7 \times 10^{25}$
Hansen et al.(2006)	Enceladus	south polar plume	H_2O	$5 -> 10 \times 10^{27}$
Hansen et al.(2011)				6.5×10^{27}
Current model				4.0×10^{27}

The main loss process for neutral species is charge exchange, where energetic, newly formed neutrals may exceed the escape velocity. Based on the water products production rate required to maintain the observed gas populations, the Cassini UVIS team determined that the lifetime of an E ring grain is on the order of two months [20]. Assuming grains are generated by the impact of micrometeoroids onto icy surfaces, the earlier grain lifetime estimate of $\sim$ 20 yr would require a grain production rate of 1 kg s^{-1} off the surface of Enceladus and an ejecta mass to micrometeoroid mass ratio of $Y \sim 900$ [47], well in line with the $10^3 < Y < 10^4$ expected from impacts at relative velocities of several km s^{-1} onto solid surfaces. The interplanetary meteoric material flux of 10^{-16} g cm^{-2} s^{-1} [28] would generate enough ejecta to sustain the E ring assuming the longer lifetime for ring particles. It is unknown how the E ring grain population could be replenished at the much higher rate which would be required to replace ring particles in only two months.

Given the low sputtering yields (less than one $\mathrm{H_2O}$ molecule per ion) for the relatively low energy ions in the inner magnetosphere, sputtering of icy grain surfaces is not rapid enough to produce the required flux of water products. While the geometry of the ice may also have an effect, with enhanced sputtering yields calculated for finite grains compared to large ice slabs [48] and preferential erosion of submicron grains compared to larger grains [50], the sputtering yields would still be insufficient. The formation of cluster ions on grain surfaces, e.g. $H^+ + \text{grain} \rightarrow H_3O^+ \cdot (H_2O)_n$ on the grain surface, and the subsequent release of water products when the cluster ion dissociatively recombines with electrons, has also been posited as a mechanism to remove $\mathrm{H_2O}$ molecules from icy surfaces[89].

The estimated energy deposition rate needed to drive the chemistry is 14 GW for the 3 to 6 R_S region [20] (current model: 4.1 GW; see Chapter 4), supplied mainly by energetic electrons injected from the outer magnetosphere. Cassini CAPS measurements of the cold (3 – 30 eV) electron density range from 1 – 10 cm^{-3}, while the hot (100 – 1000 eV) electron density was measured at 0.01 – 0.1 cm^{-3}. However, the hot electron population is severely depleted [99] inside the orbit of Tethys (4.55 R_S), in the region where the neutral cloud was observed.

1.2.3 Enceladus plume

During the Cassini flyby of Enceladus on 14 July 2005, a substantial water vapor plume was detected over the unexpectedly warm south polar region. Initial investigations reported a water-dominated composition[111], with estimates of water production at 5 – $>10 \times 10^{27}$ molecules s^{-1}, or a water output of 150 to 350 kg s^{-1}[31]. Subsequent flybys have provided more information about the plume structure, such as the presence of gas jets and dust jets in addition to the background plume[32], and its temporal variability. The current reported plume composition is 90 ±1% by volume of H_2O, 5.3 ±0.1% CO_2, 4.4% CO, <1.1% N_2, <1.2% C_2H_4, 0.8% NH_3, and minor traces of other hydrocarbons[113]. The most recent estimate of the water source rate is 200 kg s^{-1} ($\sim 6.7 \times 10^{27}$ molecules s^{-1}) with a standard deviation of 30 kg s^{-1} (15%) over three observations in 2005, 2007, and 2010[33]. While these observations are insufficient to observe the long-term variability in the vapor plume output, the H_2O supply rates required to support the HST observations of [93] indicate that the plume must have existed for at least 15 years.

Grains form some part of the output of the plume [77], [78]. Smaller clusters of H_2O molecules (ranging from e.g. several to thousands of molecules) may also be ejected. There is ongoing debate about the geophysical mechanism for the plume, and estimates of the ice to vapor ratio range from $0.1 - <0.2$[52] to ~ 0.4[76]. The small number density of E ring grains compared to gas (peak grain density $\sim 5 \times 10^{-3}$ cm^{-3} at 4 R$_s$[51] compared to densities on the order of $10^1 - 10^3$ for water and water products) indicates relatively few of the particulates in the plume escape Enceladus. Based on Cassini Cosmic Dust Analyzer (CDA) observations of the Enceladus plume, Spahn et al. [102] estimate an escape rate of 5×10^{12} particles s^{-1} for particles larger than 2 μm, corresponding to an escaping mass rate of at least 0.2 kg s^{-1} (approx. 7×10^{24} molecules s^{-1}). By comparison, a production rate of at most 10^{12} particles s^{-1} would be expected from hypervelocity impacts by E ring particles.

Porco et al. [76] infer from Cassini Imaging Science Subsystem (ISS) data an escape rate of $\sim 10^{13}$ s^{-1} for icy particles with a 1 μm radius in the Enceladus plume, with a total icy particle mass production rate of 0.4 kg s^{-1}. Note however that the CDA can only detect particles at least 2 μm in size, whereas the ISS is sensitive to particle sizes down to 0.1 μm. According to the calculations by Porco et al., only $\sim$1% of upward-moving particles in the plume escape from Enceladus; the remainder are deposited on the surface. The Enceladus plume is represented by a source with a number of adjustable parameters including total source rate, icy particle fraction, water cluster fraction, source temperature, particle and/or molecular energy distribution, and vapor composition.

1.2.4 Other sources

The Saturn atmosphere is a significant contributor of atomic hydrogen to the magnetosphere. The mechanism is electron impact dissociation of H_2 in the upper atmosphere[93] producing energetic H atoms, but the forcing of the electrodynamics is not understood. The broad distribution of the O torus (e.g. Figure 1.7) is only partially explained by scattering, as in the model of Johnson et al. [45]. Another source of O may be needed to model the observed distribution.

In addition to a large source rate from the Enceladus plume whose long-term temporal variation is still unknown, the relatively steady supply of neutral water products assumed to be produced from sputtering of satellite surfaces and E ring grains, and a steady supply of H from the Saturn atmosphere, transient sources must also be present in order to explain events such as the large atomic oxygen surge observed by UVIS, as well as smaller, more localized and rapid variations in oxygen concentrations. Mechanisms such as the collision of moonlet-sized icy bodies are among the possible sources [88]. However, transient sources are not the focus of the proposed work and will not be considered initially.

1.3 Water clusters

Although the contributions of E ring grains to the inner magnetospheric chemistry have not yet been studied in detail, a preliminary analysis by Shemansky[89] examined the size of the contribution of the E ring grains by adding grains to the existing gas phase chemistry model and estimating the size of their effect on the chemistry. While the addition of grains lowered the time needed to deplete the oxygen to ∼60 days. The more rapid changes which were observed (e.g., halving of the oxygen concentration over time scales ∼1 week in localized regions of the magnetosphere) indicate the presence of other processes which have not yet been identified.

The vapor plume which expands away from the south polar region of Enceladus contains water clusters[77] and nanometer-sized grains[46] as well as molecular and atomic gas particles and larger ($\gtrsim \mu$m) icy grains. Ion clusters may escape to the gas from ion impacts on ice[58]. The chemical reactions in which the water clusters participate will primarily be cluster ion formation and dissociative recombination. Clusters may also grow in size by binding to H_2O molecules or, albeit less likely, other clusters; collisions may presumably cause clusters to break up as well. However, given the relative scarcity of grains and clusters compared to the gaseous neutrals, the initial chemistry simulations omit both grains and clusters.

Chapter 2

Chemistry simulation code

This chapter describes an initial set of reactions designed to examine the gas phase chemistry in the inner magnetosphere (termed a water chemistry "architecture"), a chemistry code developed to solve the rate equations resulting from the system of reactions, and the approach taken explore the parameter space which allows the chemistry simulation results to be compared against observations.

2.1 Rate theory and the architecture file

The generic chemical reaction

$$A + B \rightarrow C + D \tag{2.1}$$

has an initial state i with the reactants A and B and a final state j with the products C and D. The rate for the reaction is

$$R = k_{ij}[A][B] \tag{2.2}$$

where $[A]$ and $[B]$ are the number densities of A and B, respectively, and k_{ij} is the rate coefficient, in cm^{-3} s^{-1}. The rate coefficient, a measue of the probability that the reaction occurs, will depend on the relative velocity of the reactants. For most of the reactions in this system, one of the reactants (the "impactor") carries most of the velocity; the slower reactant is the "target".

When the reactants include an electron, T will be the electron temperature; the ion or neutral reactant moves so much more slowly that it is effectively a stationary target for the electron. For neutral-neutral reactions, T is the temperature of one of the reactants. The ions are frozen into the magnetic field. Therefore, in ion-neutral reactions, the ions are the impactors and E is determined by the velocity difference between the corotating ion and the effectively stationary orbiting neutral.

The rate coefficients can be expressed in terms of the nondimensional collision strength $\Omega_{ij}(v)$, a quantity proportional to the cross section $\sigma_{ij}(v)$ for the reaction divided by the energy of the impactor[90]:

$$\sigma_{ij}(v) = \frac{\pi \hbar^2}{m^2 v^2}\ \Omega_{ij}(v) \tag{2.3}$$

where v is the relative velocity of the reactants and m is the mass of the impactor, or for neutral-neutral reactions the reduced mass of the reactants. When fitting analytical forms of the collision strength from cross section data, it is convenient to define the nondimensional energies $X = \frac{E}{E_{ij}}$ for reactions with monoenergetic impactors and $Y = \frac{E_{ij}}{kT}$ for reactions with thermal impactors, where $E = \frac{1}{2}mv^2$ (monoenergetic) or kT (thermal) and E_{ij} is a threshold energy for the reaction. E_{ij} may be a physically meaningful energy, such as an ionization potential or dissociation energy, but may also be a purely numerical quantity which aids in the fitting process. The degeneracy of the reaction's initial state, ω_i, must also be taken into account.

In their most basic forms, the rate coefficients are

$$k_{ij}(Y) = \frac{h^2}{(2\pi m)^{\frac{3}{2}}} \left(\frac{Y}{E_{ij}}\right)^{\frac{1}{2}} \frac{\Omega(Y)}{\omega_i} \tag{2.4}$$

for exothermic reactions with thermal impactors, or

$$k_{ij}(Y) = \frac{h^2}{(2\pi m)^{\frac{3}{2}}} \left(\frac{Y}{E_{ij}}\right)^{\frac{1}{2}} \frac{\Omega(Y)}{\omega_i} e^{-Y} \tag{2.5}$$

for endothermic reactions with thermal impactors, or

$$k_{ij}(X) = \frac{\pi \hbar^2}{\sqrt{2}\, m^{\frac{3}{2}}} \frac{1}{E^{\frac{1}{2}}} \frac{\Omega(X)}{\omega_i} \tag{2.6}$$

for monoenergetic impactors. Additional functions of Y may need to be added as factors to the basic equations for $k_{ij}(Y)$ depending on the physics of the process, e.g. momentum transfer is present. Further details are in Appendix A.

The collision strengths $\Omega_{ij}(X)$, for reactions with monoenergetic impactors, and $\Omega_{ij}(Y)$, for reactions with thermal impactors, are calculated using suitable functional forms, e.g.

$$\Omega_{ij}(X) = C_0 \cdot \left(1 - \frac{1}{X}\right) \cdot X^{-2} + \sum_{k=1}^{4} C_k \cdot (X-1) \cdot e^{-k \cdot C_8 \cdot X} + C_5 + \frac{C_6}{X} + C_7 \cdot \ln(X) \tag{2.7}$$

for the excitation of a neutral particle by a monoenergetic impactor[90]. The collision strength coefficients, the C_n in Equation 2.7, are fitted to cross section data as described in Section 2.2.1.

The analytic formulations used for $\Omega_{ij}(X)$ and the corresponding thermal version, $\Omega_{ij}(Y)$, vary depending on issues such as the types of reactants involved, the endothermicity or exothermicity of the process, or whether momentum transfer is involved. Shemansky has defined 18 categories of formulations for $k_{ij}(Y)$, each with a formulation for $\Omega_{ij}(Y)$ [90].

The water chemistry architecture file is a compilation of the collision strength coefficients C_n and threshold energies E_{ij} for each reaction in the system. Other information includes the formulation to be used when calculating the collision strength, and hence the rate coefficient; and the reactants and products are specified. Appendix C describes the architecture file used in this work in more detail and provides a listing of the file.

2.1.1 Basic water chemistry

Previous models of the chemistry of the Saturn magnetosphere were based on gas phase chemistry with H_2O as the dominant source molecule. Reactions between gaseous species and solid phase materials (grains, water clusters) have been excluded. There are currently 74 chemical reactions and two diffusion processes (a full listing is in Table 2.1) in the present, gas-phase only model. However, particulate matter and the molecules ejected from their surfaces may ultimately be required to supplement the gas phase chemistry and reproduce more closely the observed magnetosphere.

Once H_2O molecules are in the magnetosphere, various water products will form under the influence of energy inputs from solar radiation and the hot electrons in the inner magnetosphere. The energy balance of the system must be taken into account in order to constrain the result to a statistical equilibrium.

The primary source of energy going into the magnetosphere is the hot electron population. Electron impact ionization by the heterogeneous electrons produces the secondary electrons that form the locally trapped plasma sheet electrons. Collisions with the neutrals and plasma sheet electrons cool the secondary electrons. Solar radiation forcing is included, but the electrons are the main driver in the system.

While the Cassini data are used to contrain the temperatures and densities of the input forcing electrons, the iterative calculations performed by the chemistry code do not explicitly consider the energy balance. The energy balance calculation is performed after the fact, based on the gas species partitioning calculated by the rate code. Known data such as electron energy loss probabilities in collisions with the various neutral gas species (H, OH, etc.) allow the calculation of the energy flows in the system.

It is possible to obtain statistical equilibrium and charge neutrality without having energy balance in the system. Energy balanced magnetospheric gas compositions are a subset of the possible outputs of the first stage of the physical chemistry code. The 1992 Shemansky and Hall paper[93] is one example of an energy balance calculation which led to the realization that the Saturn magnetosphere must contain a large neutral cloud in order to explain the observed populations.

Photoreactions play an important role in the inner magnetosphere. In particular, the H Lyman-α and shorter wavelength photons are energetic enough to dissociate and ionize water molecules. The main reactions to be considered are the following:

$$
\begin{aligned}
H_2O + h\nu &\rightarrow OH + H \\
&\rightarrow H_2 + O(D) \\
&\rightarrow 2H + O \\
&\rightarrow H_2O^+ + e \\
&\rightarrow OH^+ + H + e \\
&\rightarrow O^+ + H_2 + e \\
&\rightarrow OH + H^+ + e
\end{aligned}
$$

i.e. reactions 6 through 12 (a full listing is in Table 2.1).

The neutral dissociation products of water will also interact with solar radiation, e.g. reactions 37 through 40:

$$
\begin{aligned}
OH + h\nu &\rightarrow OH^+ + e \\
&\rightarrow O + H
\end{aligned}
$$

Solar radiation interacts with the molecular hydrogen present in the magnetosphere. Some example reactions are reactions 29 through 32,

$$\begin{aligned} H_2 + h\nu &\rightarrow H_2^* \rightarrow H(1s) + H(1s) \\ &\rightarrow H(1s) + H(2s, 2p) \\ &\rightarrow H_2^+ + e \\ &\rightarrow H + H^+ + e \end{aligned}$$

The gas phase chemistry also involves species such as O_2 which can form through interactions with solid phase materials as well as through gas phase reactions, even if the models do not explicitly handle the details of the solid phase reactions yet. Reactions 16 through 20 are

$$\begin{aligned} O_2 + h\nu &\rightarrow O + O \\ &\rightarrow O_2^+ + e \\ &\rightarrow O + O^+ + e \end{aligned}$$

In the Saturn system, H_2 and O_2 will typically be in their ground states.

Plasma sheet electrons dissociate and ionize the gas molecules. Some reactions can result in a number of dissociation products which are designated collectively as *pd*. Specific products must be selected to represent *pd* when setting up the chemistry architecture. Some representative reactions are

$$\begin{aligned} H_2O + e &\rightarrow H_2O^+ + 2e \\ H_2 + e &\rightarrow H(1s) + H^+ + 2e \\ O_2 + e &\rightarrow O + O \end{aligned}$$

which are reactions 1, 22, and 13, respectively. As with photodissociation and photoionization, the rates for the corresponding electron impact processes will generally be understated, as the laboratory cross section measurements used to derive collision strength coefficients are taken on molecules in the ground or low excited states. The discrepancies in cross section for ionization or dissociation of excited molecules can be substantial, and methods for taking excitation states into account, e.g. Liu and Shemansky[64], were used where necessary.

Neutral dissociation products will also interact with the secondary electrons and solar radiation. These reactions include reactions 46, 36, 40, and 49:

$$\begin{aligned} H + e &\rightarrow H^+ + 2e \\ OH + e &\rightarrow O + H + e \\ OH + h\nu &\rightarrow OH^+ + e \\ O + e &\rightarrow O^+ + 2e \end{aligned}$$

Molecular ions interact with electrons from both the hot and the cold populations. Recombination leads to dissociation products. For example, reactions 53, 54, and 55:

$$\begin{aligned} H_2O^+ + e &\rightarrow OH + H \\ &\rightarrow OH^+ + H + e \\ &\rightarrow OH + H^+ + e \end{aligned}$$

Given the large neutral/ion ratio, charge exchange is a more probable process for ions to undergo than is recombination. Examples of charge exchange reactions include

$$\begin{aligned} H^+ + H &\rightarrow H + H^+ \\ OH^+ + H_2O &\rightarrow OH + H_2O^+ \end{aligned}$$

which are reactions 67 and 60. The recombination rate for atomic ions is much smaller than that of molecular ions, on the order of 10^{-13} cm^{-3} s^{-1} vs 10^{-8} – 10^{-9} cm^{-3} s^{-1}. Charge exchange is the dominant loss process for H^+ and O^+. Ion diffusion is neglected because loss rates for diffusion are much slower than the loss rates for charge capture.

Other reactions between ions and neutrals or neutrals and neutrals occur, with the products participating in subsequent reactions. For example, reactions 50 and 61:

$$\begin{aligned} OH + O &\rightarrow O_2 + H \\ OH^+ + H_2O &\rightarrow O + H_3O^+ \end{aligned}$$

These reactions are slow in comparison to the other reactions in the system. Although the molecular formation of O_2 under astrophysical conditions is typically associated with icy surfaces, reaction 50, O + OH $\rightarrow$ O_2 + H, occurs in the gas phase[118].

2.2 Water chemistry architecture

A baseline set of magnetospheric gas phase chemical reactions which would occur in the absence of grains and clusters has been set up. At present, electronic excitation is not included in the chemistry, and rovibrational states are not tracked; however, the chemistry rates are based on separate detailed calculations on the species under appropriate physical conditions. To conserve heavy particles, neutral products energetic enough to escape the Saturn system are replaced by diffused-in neutral particles (H_2O for this initial phase). Table 2.1 lists the gas phase reactions used for the baseline case; some gas phase reactions are energetically possible but are not included because their rates are slow compared to those of the listed reactions.

Table 2.1: Baseline gas phase reactions at 4 R_s

Label	Reaction		Source
1	$e + H_2O$	$\rightarrow H_2O^+ + 2e$	[84]
2	$e + H_2O^a$	$\rightarrow OH^+ + H^b + 2e$	[84]
3		$\rightarrow H^+ + OH$	[84]
4		$\rightarrow O^+ + H_2$	[84]

Continued on next page

Table 2.1 – continued

Label	Reaction		Source
5		$\rightarrow$ $OH + H^b$	[34]
6	$h\nu + H_2O$	$\rightarrow$ $OH + H^b$	[36]
7		$\rightarrow$ $H_2^b + O(D)$	[36]
8		$\rightarrow$ $H + H + O$	[36]
9		$\rightarrow$ $H_2O^+ + e$	[36]
10		$\rightarrow$ $OH^+ + H^b + e$	[36]
11		$\rightarrow$ $O^+ + H_2^b + e$	[36]
12		$\rightarrow$ $OH + H^+ + e$	[36]
13	$e + O_2$	$\rightarrow$ $O^b + O^b + e$	[41]
14		$\rightarrow$ $O_2^+ + 2e$	[60], [65]
15		$\rightarrow$ $O^b + O^+ + 2e$	[60], [65]
16	$h\nu + O_2$	$\rightarrow$ $O(3P)^b + O(3P)^b$	[36]
17		$\rightarrow$ $O(3P)^b + O(1D)^b$	[36]
18		$\rightarrow$ $O(1S)^b + O(1S)^b$	[36]
19		$\rightarrow$ $O_2^+ + e$	[36]
20		$\rightarrow$ $O^b + O^+ + e$	[36]
21	$e + H_2$	$\rightarrow$ $H^b + H^b + e$	[84]
22		$\rightarrow$ $H(1s)^b + H^+ + 2e$	[105]
23		$\rightarrow$ $H_2^+ + 2e$	[105]
24		$\rightarrow$ $H_2(a) + e \rightarrow H^b + H^b + e$	[14]
25		$\rightarrow$ $H_2(b) + e \rightarrow H^b + H^b + e$	[14]
26		$\rightarrow$ $H_2(c) + e \rightarrow H^b + H^b + e$	[14]
27		$\rightarrow$ $H_2(e) + e \rightarrow H^b + H^b + e$	[14]
28		$\rightarrow$ $H_2(d) + e \rightarrow H^b + H^b + e$	[14]
29	$h\nu + H_2$	$\rightarrow$ $H(1s)^b + H(1s)^b$	[36]
30		$\rightarrow$ $H(1s) + H(2s, 2p)$	[36]
31		$\rightarrow$ $H_2^+ + e$	[36]
32		$\rightarrow$ $H^b + H^+ + e$	[36]
33	$e + OH$	$\rightarrow$ $OH^+ + 2e$	[84]

Continued on next page

Table 2.1 – continued

Label	Reaction		Source
34		$\rightarrow O^{+} + H^{b} + 2e$	[84]
35		$\rightarrow H^{+} + O + 2e$	[84]
36		$\rightarrow O + H^{b} + e$	[84]
37	$h\nu + OH$	$\rightarrow O(3P) + H^{b}$	[36]
38		$\rightarrow O(1D) + H^{b}$	[36]
39		$\rightarrow O(1S) + H^{b}$	[36]
40		$\rightarrow OH^{+} + e$	[36]
41	OH	diffusion	
42	$e + H_3O^{+a}$	$\rightarrow H_2O^{b} + H^{b}$	[73]
243		$\rightarrow OH^{b} + H_2^{b}$	[73]
44		$\rightarrow OH^{b} + H^{b} + H^{b}$	[73]
45		$\rightarrow O^{b} + H_2^{b} + H^{b}$	[73]
46	$e + H$	$\rightarrow H^{+} + 2e$	[83]
47	$h\nu + H$	$\rightarrow H^{+} + e$	[36]
48	$O_2 + H$	$\rightarrow O + OH$	[114]
49	$e + O$	$\rightarrow O^{+} + 2e$	[10]
50	$O + OH$	$\rightarrow O_2 + H$	[114]
51	$h\nu + O(3P)$	$\rightarrow O^{+} + e$	[92]
52	O	diffusion	
53	$e + H_2O^{+a}$	$\rightarrow OH^{b} + H^{b}$	[84]
54		$\rightarrow OH^{+} + H^{b} + e$	[84]
55		$\rightarrow OH^{b} + H^{+} + e$	[84]
56	$H_2O^{+} + H_2O$	$\rightarrow H_3O^{+} + OH$	[114]
57	$e + OH^{+}$	$\rightarrow O^{b} + H^{b}$	[106]
58		$\rightarrow O^{+} + H^{b} + e$	[84]
59		$\rightarrow O^{b} + H^{+} + e$	[84]
60	$OH^{+} + H_2O$	$\rightarrow OH^{b} + H_2O^{+}$	[4], [59], [3]
61		$\rightarrow O^{b} + H_3O^{+}$	[4], [59], [3]
62	$e + H_2^{+}$	$\rightarrow H^{b} + H^{b}$	[66]

Continued on next page

Table 2.1 – continued

Label	Reaction		Source
63	$H^+ + H_2O$	$\rightarrow H_2O^+ + H^b$	[4], [27], [61]
64	$H^+ + O$	$\rightarrow O^+ + H^b$	[103], [75]
65	$H^+ + O_2$	$\rightarrow O_2^+ + H^b$	[62]
66	$H^+ + OH$	$\rightarrow H^b + OH^+$	[4], [27], [61]
67	$H^+ + H$	$\rightarrow H^b + H^+$	[4]
68	$H^+ + H_2$	$\rightarrow H^b + H_2^+$	[38]
69	$O^+ + H$	$\rightarrow O^b + H^+$	[103], [75]
70	$O^+ + H_2O$	$\rightarrow O^b + H_2O^+$	[4], [59]
71	$O^+ + OH$	$\rightarrow O^b + OH^+$	[109]
72	$O^+ + O$	$\rightarrow O^b + O^+$	[55]
73	$O^+ + H_2$	$\rightarrow O^b + H_2^+$	[38]
74	$O^+ + O_2$	$\rightarrow O^b + O_2^+$	[62]
75	$e + O_2^+$	$\rightarrow O^+ + O^b + e$	[84]
76		$\rightarrow O^b + O^b$	[70]

[a] Products were originally unspecified dissociation products *pd*.

[b] Product escapes.

2.2.1 Derivation of cross sections in the absence of experimental data

Reaction collision strengths (Equation 2.7) for the complete set of reactions are contained in the water chemistry architecture file. The rate coefficients are used in the energy budget calculations as well as the chemistry calculations. The collision strength coefficients are fitted from experimental cross section and/or rate coefficient data when available. Experimental cross section data are not published for every reaction listed. Theoretical cross sections are used where necessary.

2.3 Rate equations

The rate equations for each species are written out in Appendix B.

The calculation requires a steady state. The loss terms and production terms for each species can be combined into a total loss rate and a total production rate, which are used to solve for the population in that iteration. In the $(j+1)$th iteration, the population for species i, $[N_{j+1,i}]$ is given by

$$[N_{j+1,i}] = \frac{R_{j,i}}{Q_{j,i}} \times S \tag{2.8}$$

where $R_{j,i}$ is the total production rate (cm^{-3} s^{-1}) and $Q_{j,i}$ is the total loss rate (s^{-1}) of species i, as in e.g. Equation B.2; and S is a scaling factor introduced to conserve the number of atoms in the system. These total rates are summed over all processes involving the i and are calculated using the appropriate rate coefficients or transition probabilities and the calculated populations from the jth iteration.

2.4 Chemistry rate code

The water chemistry code, coreqg.f90, is based on the hydrogen chemistry model developed by Hallet et al. [30], [29]. A chemistry architecture file describes the reactions in the system and provides the collision strength coefficients needed to calculate the rates. Forcing electrons, either two populations of thermal electrons or one population of monoenergetic electrons, provide an energy input to the system. A set of input parameters consists of either the monoenergetic electrons' number density and energy or the number densities and temperatures of the two thermal electron populations. A listing of the water chemistry architecture file, h2og.mdf, appears in Appendix C.

A starting population of base species particles, H_2O in the case of the water chemistry system, is also specified. In the absence of the Saturn hydrogen forcing, the initial gas state is 100% H_2O; the populations of all other species start at zero, and all species' populations are solved by iterating the rate calculations. When the hydrogen forcing is present, [H] is not iterated, but fixed to the value specified in the input file, and the remaining populations are solved iteratively from the initial 100% H_2O state. The forcing electron populations are fixed in a given calculation. This determines the total heavy particle mass in the steady state gas, through the adjustment of the neutral source rate to obtain equilibrium.

The calculation is considered to have converged when both a statistical equilibrium condition and a charge neutrality condition are satisfied. The criterion which must be met for statistical equilibrium is that the iterated populations have stabilized, within a specified tolerance. Charge neutrality is achieved when the iterated population of ions matches the imposed electron populations, within a specified tolerance. If either condition is not satisfied, total number of atoms in the system is adjusted and the iterative process is restarted. The total number of iterations is capped at a value selected by the user; if the gas species populations have not converged after the maximum allowed number of iterations, the code terminates. In general, the code completes the iterative calculation rapidly (within a few thousand iterations). The maximum number of iterations was set to 10,000. The flowchart in Figure 2.1 illustrates the calculation procedure.

During the iterative rate calculations, the total number of atoms in the system is conserved. The calculations begin with an arbitrary initial number density for H_2O. As the chemistry proceeds, energetic neutral products which escape the magnetosphere and

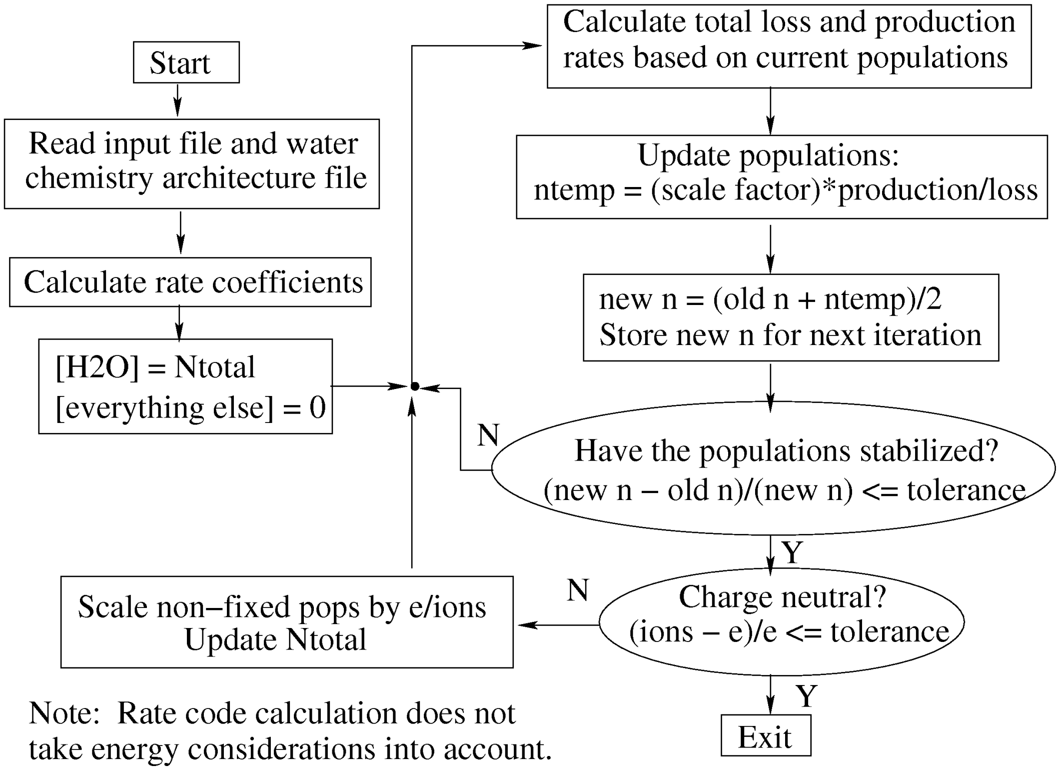

Figure 2.1 Flowchart for chemistry code coreqg.f90.

The water chemistry architecture file, h2og.mdf, contains rate coefficient data and specifies the product and reactant species for all chemical reactions (including photoprocesses) in the system. The input file specifies the number densities and temperatures for the two electron populations in the system: plasma sheet electrons and the heterogeneous electrons which are the primary energy source. The populations of all thirteen species in the system are iterated except in cases where the Saturn atmospheric H flux is modelled, in which case $[H]$ is fixed to the observed value of 500 cm^{-3}[94]. At each iteration, the total loss and production rates for each species are calculated from the rates of all reactions in the system, and new populations are calculated using input-output averaging. To conserve heavy particles, reaction products which are energetic enough to escape and particles lost to diffusion are replaced by diffused-in H_2O molecules. If the populations have stabilized into statistical equilibrium, charge neutrality is checked. If charge neutrality is not satisfied, the total number of heavy particles (non-electron species), Ntotal, is adjusted to bring the number of ions closer in line to the input electron populations, and the iterations begin again. When both statistical equilibrium and charge neutrality have been achieved, the calculation is complete. Energy balance is not taken into account.

O and OH which diffuse out are replaced on an atom-by-atom basis by H_2O. At each failed charge neutrality check, all iterated populations are multiplied by a scaling factor to reduce the disparity between the total number of ions and the input electron populations. The iterative calculation continues using the adjusted populations.

The inputs which govern the chemistry rate calculations are the electron parameters: the plasma sheet electron temperature T_{ec} and density n_{ec}, and the heterogeneous electron temperature T_{eh} and density n_{eh}. The heterogeneous electrons drive the chemistry through their energy input to the gas system; as a forcing function in the chemistry model, any hot electrons lost to chemistry and any energy lost to the gas during their passage through the magnetosphere are immediately replaced by the external source and n_{eh} and T_{eh} remain constant. The plasma sheet electrons are too cold to participate in the chemistry to any significant extent, but strongly influence the subsequent energy balance calculation. The chemistry code determines the statistically equilibrated gas species partitioning which would be required to support the presence of the input electron populations, however physically unrealistic the inputs may be.

2.5 Baseline gas phase chemistry

In this work, only gas phase chemistry is considered. The observed bimodal electron energy distribution in the E ring region is simulated with two thermal electron populations, a cold population representing plasma sheet electrons and a hot population representing heterogeneous electrons. The heterogeneous electrons are the primary source of energy for the plasma sheet. Because the cross sections for the chemical reactions under consideration do not vary strongly with temperature in the energy range of the heterogeneous electrons, the specific value of hot electron temperature is not critical. Calculations are carried out using user defined fixed electron populations and temperatures. The resulting statistically equilibrated state of the gas is recorded as part of a set of systematically varied electon constraints.

Observations are used as constraints for the model parameters, but the current data do not fully constrain the model. The cold plasma sheet electrons are not directly measurable by the Cassini *in situ* experiments because of spacecraft charging effects. To investigate how the total electron number density (and hence the total ion density) affects the outcome of the chemistry, the cold electron number density is set to one of three values, 50 or 75 or 100 cm^{-3}[97]. Although the cold electron temperature is an input to the chemistry code, the energy balance calculation must be done on the resulting species partitioning to determine whether the energy available to the gas system can sustain the input value of plasma sheet electron temperature. It is important to distinguish between the plasma sheet electron temperatures T_{ec} that are inputs to the chemistry code and the energy equilibrated plasma electron temperatures T_{eq} (c.f. Section 3.3) obtained from the net energy rate curves (see Figure 4.3) that are calculated from the chemistry code outputs in the energy balance calculation (described in Chapter 3).

To investigate the effects of the atomic hydrogen sourced from the Saturn atmosphere, two chemistry outputs are calculated for each set of hot and cold electron number density and temperature. Outputs where the population of is fixed to 500 cm^{-3} represent the chemistry in the presence of the heterogeneous H, while outputs where the HI population is iterated represent the chemistry in the absence of the hydrogen outflow from the atmosphere. Not all of the chemistry code outputs are valid, i.e., the net energy rate for the plasma electrons is zero. The energy budget calculation (discussed in the next chapter) is used to determine which chemistry outputs are energetically feasible, thus imposing constraints on the possible values of hot electron number densities and cold electron temperatures.

2.6 Other magnetospheric chemistry models

Two recent models based on Cassini observations form the basis for comparing this model's results against observed data. Two other chemistry models are also discussed briefly.

Schippers et al.[82] determine the magnetospheric electron density and temperature profiles inside 20 R_s using CAPS and MIMI data. The CAPS Electron Spectrometer (ELS) and MIMI Low Energy Magnetospheric Measurements System (LEMMS) collectively can detect electron energies ranging from a 0.6 eV to 10 MeV. The observations were performed on two consecutive days at latitudes of 0.23 and 0.35 degrees, with a long term objective of studying the latitudinal variations. The Schippers et al. analysis concludes the thermal electrons (energy $<$ 100 eV) originate from distributed sources in the inner magnetosphere, while suprathermal electrons (100 eV $<$ energy $<$ 10 keV) are likely sourced from the middle magnetosphere. The plasma sheet electrons originate from secondary production by the sustaining energy sources in the system, the heterogeneous electrons and solar input in the model calculation.

Sittler et al.[97] derive their ion and neutral model from CAPS observations. The rate equations in their chemistry model include terms for ion production, radial transport, recombination, and charge exchange, resulting in loss and production rates for H^+, W^+ (the ions are not broken out by species), and neutrals (H, O, OH, and H_2O, likewise not broken out by species). Energy is not a consideration in their calculations, which concluded water molecules are the primary source of ions in the inner magnetosphere.

Cassidy and Johnson[13] model the structure of the Saturn OH and O clouds using direct simulation Monte Carlo (DSMC). Earlier DSMC models included only charge exchange and dissociation (both electron impact and photo-), which alone were not sufficient to explain the broad distribution reported by the Melin et al. [67] UVIS Saturn system scans. Their addition of ion/neutral scattering brings the DSMC model in line with the UVIS observations. Because the DSMC model is oriented toward examining the dynamics leading to the extended neutral clouds and not toward chemistry per se, chemical processes such as ionization and recombination are not included. While the collisions modeled in the DSMC technique individually conserve energy, there is no comparison between the energy required by the modelled processes which spread the neutrals out in the magnetosphere and the energy inputs available to the system.

Fleshman et al. examine the physical chemistry of the Enceladus water torus in two papers, [23] and [24]. Their model solves number density and energy density rate equations for H, H_2, O, O_2, OH, H_2O, H^+, H_2^+, O^+, O^{++}, OH^+, H_2O^+, and H_3O^+ (O_2 is omitted). A set of constraints is chosen, the rate equations are solved using random walks to vary the input parameters, and the calculation is ended when the model values match the constraint values. Physical processes included in the source and loss terms are charge exchange, electron impact ionization, photoionization, photodissociation, electron impact dissociation, recombination, and radial transport. A full list of reactions in the system is not given, but must be inferred from the tables in the supplemental material for [23]. While Fleshman et al. perform an energy calculation for the chemical system as a whole, processes such as momentum transfer and Coulomb energy transfer between the hot and cold electrons appear to be missing. In addition, not every relevant species appears in the section for each of the processes considered in the energy flow and it is not clear whether there is an energy rate equation for the plasma electrons.

The chemistry rates in the Fleshman et al. model are questionable. For example, the rate coefficient of 2.1×10^{-9} cm^{-3} s^{-1} listed for the reaction $H_2O + H_2O^+ \rightarrow H_3O^+ + OH$ is the value listed by Huntress[37] at 300 K, with no adjustment made for gas temperatures which might be expected in the inner magnetosphere. The value used in this work is smaller by a factor of 100 [92]. In addition, the rate coefficient listed for the reaction $H_2O + H_2O^+ \rightarrow H_2O^+ + H_2O$ is based on data measured for $H_2O^+ + D_2{}^{18}O \rightarrow H_2O + D_2{}^{18}O^+$ and/or $D_2{}^{18}O^+ + H_2O \rightarrow D_2{}^{18}O + H_2O^+$ by Lishawa et al.[63]. In practice, $H_2O + H_2O^+$ charge exchange would not occur, as (analogous to the case of $e + H_2O^+$) the ion would undergo dissociative recombination rather than recombination[92]. A comparison of the Fleshman et al. chemistry output against the coreqg.f90 outputs for the same hot and cold electron parameters is in Chapter 4. According to the present calculations, the Fleshman et al. results are grossly out of energy balance.

Chapter 3

Energy budget calculation

The primary energy sources forcing the formation of the plasma sheet are the heterogeneous electrons and solar radiation. The current structure of the physical chemistry code does not internally determine the energy budget of the system. The input parameters are forced on the computational equilibrium in the plasma and the output does not necessarily represent an energy balanced plasma. A separate calculation is needed to determine the flow of energy in the system. If the calculated chemical equilibrium is out of energy balance, it represents a statistically equilibrated temporally transient state. Given the conditions placed on the sources, this means that only certain values of ambient and heterogeneous electron densities and temperatures will satisfy energy balance in the system. Energy balance is determined in this case by using a range of values for the forcing parameters and subsequently calculating the energy budget for the resulting statistical equilibrated states. The energy surplus or deficiency quantity is then parameterized to determine the energy balance condition. The results produce a family of balance points because changing the heterogeneous electron density forces the deposition of more or less energy into the system that must be balanced with internal sourcing and losses in the resulting statistical equilibrium.

The species populations calculated by the chemistry code represent the outcome of the system of chemical reactions for the values of plasma electron temperature and number density, and heterogeneous electron number density selected as inputs. The reaction rate coefficients do not depend strongly on temperature in the energy range of the heterogeneous electrons, so the exact value of the hot electron temperature is not critical in determining the outcome. Comparison against observations constrains the range of modeled energy balanced plasma states.

The energy equation for the plasma sheet electrons and for each ion species has the general form

$$\frac{dE_j}{dt} = S_j - L_j \tag{3.1}$$

where S_j are source terms and L_j are loss terms for species j. The hot electrons do not remain in the magnetosphere but act as an energy source as they pass through. Ions created by the heterogeneous electrons and the solar flux become a major source of energy for the plasma sheet through subsequent pickup in the Saturn magnetic field. Plasma lifetimes and ion temperatures are extracted from these calculations.

3.1 Energy loss processes

In an electron impact ionization of a neutral particle, the electron loses energy and the newly formed ion is captured by the magnetic field. Other processes included in the energy balance process are momentum transfer from charged particles to neutrals, Coulomb energy transfer between charged particles, and radiative losses due to electron impact excitation. Some processes, such as bremsstrahlung, produce energy losses which are small and are neglected in this model.

The rate coefficients in the chemistry-related energy loss and source terms are also used by the chemistry code. The calculation of energy rates requires somewhat more information than does the calculation of the chemistry rates. While multiple excited energy states and their corresponding branches in the chemical reactions could be collapsed as far as the chemistry code is concerned, the calculation of energy rates must take them into account.

3.1.1 Coulomb energy transfer

Charged particles exchange energy through the Coulomb potential. In this work, one of the particles, the test particle (no subscript), will generally have a higher kinetic energy than the other, which can be treated as a stationary field particle (denoted by the subscript f). For electron-electron Coulomb energy transfer, the heterogeneous electrons are the fast test particles while the plasma electrons are the field particles; for electron-ion interactions, the electrons (whether cold or hot) are the test particles and the ions the field particles.

Spitzer[104] gives the equilibration time (in seconds) between test and field particles as

$$t_{eq}(T, T_f) = 5.87 \frac{A A_f}{n_f Z^2 Z_f^2 \ln(\Lambda)} \left(\frac{T}{A} - \frac{T_f}{A_f} \right)^{\frac{3}{2}} \tag{3.2}$$

where A and A_f are the atomic weights of the test and field particles, respectively, Z and Z_f are the charges of the test and field particles, n_f is the field particle density, and the shielding parameter Λ is given by

$$\Lambda = \frac{3}{2ZZ_f e^3}\left(\frac{k^3T^3}{\pi n_e}\right) \tag{3.3}$$

where e is the electron charge (ESU), T is the test particle temperature, and n_e is the electron density. All quantities in this equation are in cgs units.

The rate coefficient for Coulomb energy transfer sums the contributions over the field particle species and is given by[86]

$$k_{eq}(T, T_f) = \frac{1}{\sum_f n_f} \cdot \sum_f \frac{1}{t_{eq}(T, T_f)} \tag{3.4}$$

where T_f = field particle temperature. Coulomb energy transfer from the hot electrons to the cold electrons appears as a source term for the plasma sheet electrons.

$$S_e = k_{eq}(T_{ec}, T_{eh}) \cdot n_{ec} \cdot n_{eh} \cdot (E_{eh} - E_{ec}) \tag{3.5}$$

where (T_{ec}, n_{ec}, E_{ec}) and (T_{eh}, n_{eh}, E_{ec}) are the temperature, number density, and energy of the cold and hot electrons, respectively. Coulomb energy transfer between plasma sheet electrons and ions appears as a source term

$$S_e = \sum_i k_{eq}(T_{ec}, T_i) \cdot n_{ec} \cdot n_i \cdot (E_i - E_{ec}) \tag{3.6}$$

for the cold electrons and as loss terms

$$L_i = k_{eq}(T_{ec}, T_i) \cdot n_{ec} \cdot n_i \cdot (E_i - E_{ec}) \tag{3.7}$$

for the ions. T_i, n_i, and E_i are the temperature, number density, and energy of the ion species under consideration.

3.1.2 Electron excitation-radiative loss

Although the current Saturn magnetospheric chemistry model does not keep track of excited states for either ionic or neutral species when evaluating the chemistry, the energy balance calculation must account for the energy lost by electrons to excitations. Line emissions occur through spontaneous emission. The energy loss term for the volume emission rate of such a transition is

$$L_e = N N_e \rho \tag{3.8}$$

where N and N_e are the number densities of the heavy species and the electrons, ρ is the radiative cooling coefficient in units of ergs cm^3 s^{-1}. The calculation of the radiative cooling coefficient includes both direct excitation as well as cascades, and de-excitations include radiative and non-radiative transitions[85].

The current work updates previous calculations for O and O$^+$ [85] [86] and introduces radiative cooling curves for H_2O, based on H$_2$O energy state data and transfer rates from [108], for H[91], and for OH[115].

3.1.3 Electron impact ionization loss

Electron impact ionization of the neutral species A,

$$e + A \rightarrow 2e + A^{+} \tag{3.9}$$

has an energy threshold equal to the ionization potential of A. The relatively cold plasma sheet electrons have much lower rate coefficients than the hot heterogeneous electrons[115]. The energy loss $\overline{\Delta E_{ion}}$ ranges from 35 to 39 eV per ion pair and is taken to be 35 eV per ion pair for ionizations of O, OH, O_2, and H_2O and 37 eV per ion pair for H_2 and H[91].

For the electrons, the energy loss term is

$$L_e = k \cdot [e] \cdot [A] \cdot \overline{\Delta E_{ion}} \tag{3.10}$$

while the source term for the newly created ion species, picked up by the planetary magnetic field, is

$$S_{A^+} = k \cdot [e] \cdot [A] \cdot E_{corot} \tag{3.11}$$

where E_{corot} is the corotation energy for A^{+}. k is the rate coefficient for the electron impact ionization reaction (c.f. Section 2.4).

Electron impacts on H_2O can be doubly ionized on electron impact, e.g.

$$e + H_2O \rightarrow H^+ + O^+ + H + 3e \tag{3.12}$$

$$\rightarrow H^+ + OH^+ + 3e \tag{3.13}$$

however rates for these reactions are negligible[54].

3.1.4 Electron impact molecular dissociation loss

Electron impact dissociation of the neutral molecule AB,

$$e + AB \rightarrow 2e + A^{(*)} + B^{(*)} \tag{3.14}$$

or

$$e + AB \rightarrow e + A^{+(*)} + B^{(*)} \tag{3.15}$$

has an energy threshold equal to the dissociation potential of AB. In the process, the dissociation fragments may enter excited states. For the electrons, the energy loss term is

$$L_e = k(T_e) \cdot [e] \cdot [AB] \cdot \Delta E \tag{3.16}$$

where k is the rate coefficient for the electron impact dissociation, $[e]$ and $[AB]$ are the number densities for the electrons and neutral molecule, and ΔE is the energy lost by the electron. ΔE must exceed the dissociation energy required to produce the fragments

A and B plus their excitation energy(ies). The corresponding source term for the ionic product, if any, is

$$S_{A^+} = k(T_e) \cdot [e] \cdot [AB] \cdot (E_{corot} + E^*) \tag{3.17}$$

where E_{corot} is the corotation energy for A^+ and E^* is any excitation energy which is present.

For dissociation reactions with multiple branches, such as H_2O which can have OH + H, OH + H^+, H + OH^+, or H_2 + O^+ as possible sets of products, branching ratio data are required as well as the product energies. In this case, the energy source and loss terms contain the ΔE appropriate to the particular branch, and the terms must also be scaled by the branching ratio.

For H_2O, cross sections for the photodissociation of H_2O[110] and branching ratios[110] obtained from calculations by van Harrevelt and van Hemert, and energy spectra calculated by Mordaunt et al.[68], were combined with spectra and cross sections measured by Müller et al.[71].

3.1.5 Secondary electron energy injection

Electron impact ionizations create secondary electrons. The secondary will carry off the impactor energy in excess of the target's ionization potential. If the secondary is created by a plasma electron of energy E_{ec}, its excess energy will be

$$E = E_{ec} - E_{ij} + E_{pickup} \tag{3.18}$$

where E_{ij} = ionization potential of the target and E_{pickup} is the corotation energy picked up by the newly created electron. The mean Maxwellian weighted excess energy is used to calculate the source term in the energy balance. The fractional excess energy of the secondary electron is defined as

$$Y(E,T) = \frac{E}{kT} \tag{3.19}$$

where T is the electron temperature. The Maxwellian weighted value of Y is

$$ffc(Y) = \frac{2}{\pi^{0.5}} \int_{Y}^{\infty} z^{0.5} e^{-z} dz \tag{3.20}$$

and the mean Maxwellian weighted value of Y is

$$\overline{Y(E,T)} = \frac{\int_{Y}^{\infty} z^{1.5} e^{-z} dz}{\int_{Y}^{\infty} z^{0.5} e^{-z} dz} \tag{3.21}$$

A secondary created by a heterogeneous electron which loses the energy $\overline{\Delta E_{ionpair}}$ (in range of 35 – 39 eV per ion pair as discussed above) will have an excess energy of

$$E = \overline{\Delta E_{ionpair}} - E_{ij} + E_{pkp} \tag{3.22}$$

The energy source term is the sum of the hot and cold electron source terms.

$$\begin{aligned} S_e &= k(T_{ec})[N][e_c](E_{pkp} + (\overline{Y(E_{ij},T_{ec})} - Y(E_{ij},T_{ec})) \cdot k_{th} \cdot T_{ec} \qquad (3.23) \\ &\quad + k(T_{eh})[N][e_h](E_{pkp} + \overline{\Delta E_{ion}} - E_{ij}) \end{aligned}$$

where $k(T)$ is the rate coefficient for ionization, $[N]$ is the number density of the species being ionized, $[e_c]$ and $[e_h]$ are the cold and hot electron number densities, and k_{th} is the Boltzmann constant.

Analogous source terms are constructed for electrons formed through photoprocesses. Coates et al.[15] examined Cassini electron spectra from main ring observations and concluded that photoprocesses explain some of the observed features. Their results have been applied to E ring conditions.

Electron pickup from the creation of secondary electrons accounts for roughly 30% of the plasma sheet electron energy injection, out of which about 10% is from solar photon ionization. Coulomb collisions between the ions and the electrons supply the rest of the plasma sheet electron energy injection. Coulomb energy transfer from ions is the main heating process for the plasma sheet electrons. The heterogeneous electrons are therefore directly or indirectly responsible for around 90% of the energy deposition into the plasma sheet electrons.

3.1.6 Electron-ion reactions

In recombination reactions

$$e + A^{+} \rightarrow A^{*} \tag{3.24}$$

and in dissociative recombination reactions

$$e + AB^{+} \rightarrow A^{*} + B^{*} \tag{3.25}$$

(these are effectively neutralizations where the neutral product escapes) the energies of the electron and ion which participated in the recombination must be accounted for in the energy loss terms. At the energy ranges of the heterogeneous electrons, recombination rates are insignificant and essentially, only the plasma sheet electrons will take part in recombinations. For the electrons,

$$L_e = k(T_{ec})[e_c][N_i]k_{th}T_{ec} \tag{3.26}$$

where k is the recombination rate coefficient and $[N_i]$ is the ion density, and for the ions,

$$L_i = k(T_{ec})[e_c][N_i]E_{corot_i} \tag{3.27}$$

Although the excited neutral products may be energetic enough to escape, any energy loss associated with them does not count toward the energy loss or source rates of the ions and plasma sheet electrons.

Dissociative excitation reactions, e.g.

$$\begin{aligned} e + AB^+ &\rightarrow A^+ + B + e \qquad (3.28) \\ e + AB^+ &\rightarrow A + B^+ + e \qquad (3.29) \end{aligned}$$

are endothermic and cause the electron to lose their respective dissociation energies E_{diss}. The source terms have the form

$$S_{prod} = k(T_{ec})[e_c][N_i]E_{diss} \tag{3.30}$$

Jensen et al.[42] measured cross sections and branching ratios for the dissociative recombination of H_2O^+. Cross sections and branching ratios for dissociative recombination and dissociative excitation of H_3O^+ were obtained from Andersen et al.[2] and Neau et al.[73].

3.1.7 Momentum transfer to neutrals

Momentum transfer occurs in elastic collisions between particles. Dalgarno[16] derived expressions for the momentum transfer cross section for collisions between hydrogen atoms. Electrons are far more mobile than the neutrals, therefore only electron-neutral collisions are considered in the low density plasma. Momentum transfer cross sections for electron-HI collisions were obtained through geometric scaling of the H-H momentum transfer cross sections, and cross sections for e-OI collisions obtained by scaling the e-HI cross sections.

Momentum transfer cross sections for electrons on water molecules were compiled by Itikawa and Mason[40]. The data were scaled by molecular size to obtain cross sections for OH, O_2, and H_2. Data from Itikawa et al.[41] were used for O_2.

3.1.8 Omitted processes

There are three energy loss processes omitted from the energy budget calculation.

Electron excitation of homonuclear molecules Although the electron impact excitation cross sections for H_2 X and O_2 X states (ground state H_2 and O_2) are large, radiative decay is forbidden. The only way for the excited H_2 X and O_2 X to de-excite is through collisions with electrons[92]. The plasma sheet electrons lose energy when they excite the H_2 X and O_2 X, but regain the energy through radiationless deactivation of the excited states. No net energy is lost by the plasma sheet electrons and this process is omitted from the energy balance equation.

Electron momentum transfer due to bulk motion The energy losses from momentum transfer by corotating electrons colliding with neutrals is cancelled by the acceleration compensation by ion drag[92]. The net momentum transfer losses due to bulk motion are therefore assumed to be zero, and the energy loss from electron momentrum transfer to the gas can be calculated on a local volume basis.

Bremsstrahlung The energy rate coefficient ϵ_{ff} radiated by bremsstrahlung, the emissions of photons in electron-ion collisions where the electrons are deflected but not captured by the ions, is given by

$$\epsilon_{ff} = 1.42 \times 10^{-27} Z^3 n_i^2 T^{\frac{1}{2}} \bar{g}_{ff} \tag{3.31}$$

in units of ergs cm^{-3} s^{-1}, where T is the temperature of the Maxwellian electrons, Z is the ion charge, and n_i is the ion number density[104]. The correction factor g_{ff} and its mean value $\bar{g}_{ff}$ are generally close to 1.0. The energy loss rate for bremsstrahlung is several orders of magnitude lower than the energy loss rates for other processes and can therefore be omitted.

3.2 Energy rate data files

To aid in the energy budget calculation process, Shemansky has compiled data files which contain either energy loss rate coefficients which contain $\log(k_{ij})$ as a function of $\log(T)$ where k_{ij} has units of erg cm^3 s^{-1} or chemistry rate coefficient data files containing $\log(k_{ij})$ where k_{ij} has units of cm^3 s^{-1}. T is the electron temperature, and where applicable, terms are summed over the hot and cold electrons. The chemistry rate coefficient data are not broken out by individual reaction channels as in the H_2O architecture file used by coreqg, but rather represent total rate coefficients for the process in question. These data files, which are listed in Table 3.1, will be archived as supplemental material for [115]. At present, the data files for electron pickup energy, radiative cooling, and ionization loss rates for H_2 are in the process of being compiled; the rates for these processes are small and the omission does not significantly affect the energy balance calculation[92].

The Coulomb energy transfer between hot and cold electrons is calculated according to Equation 3.4. Photoionization losses are not included with the electron impact ionization losses and must be calculated separately.

Momentum transfer The volumetric rate for plasma sheet electron momentum transfer energy relaxation is

$$L_{emt} = \sum_{i=c,h} \frac{1}{2} \cdot \frac{m_e}{m_N} \cdot k_{ij}(T_{e_i}) \cdot [e_i] \cdot [N] \cdot \left(\frac{4kT_N}{\pi} - \frac{4kT_{e_i}}{\pi} \right) \tag{3.32}$$

where k_{ij} is in cm^3 s^{-1} as interpolated from the values tabulated in the appropriate data file; m_e is the electron mass; m_N is the mass of the neutral species; $[e]$ is the electron

Table 3.1. Data files for energy loss rate calculations

Process	Species	Data file
Momentum transfer	H	HI_mt_log_rcf.csx
	O	OI_mt_log_rcf.csx
	H_2	h2_mt_log_rcf.csx
	OH	OH_mt_log_rcf.csx
	O_2	elst_t_col_o2_00_log_001.da4
	H_2O	e_h2o_02_MT_138_log.cs1
Total neutral losses	O_2	e_o2_erg_loss_neut_log.cs1
	H_2O	e_h2o_neut_tot_erg.csx
Ionization	H	e_HI_ion_log_erg.cs1
	O	Ee_loss_OI_ion_log_total.cs1
	OH	e_OH_ion_log_erg.cs1
	O_2	Ee_loss_O2_ion_tot_log.dax
	H_2O	e_h2o_totion_logerg.csx
Electron pickup	H	e_H_ion_rcf_col_h2o_02_120_log.cs1
	O	e_OI_ion_rcf_col_h2o_02_121_log.cs1
	OH	e_OH_ion_rcf_col_h2o_02_127_log.cs1
	O_2	e_O2_ion_rcf_col_h2o_02_174_log.cs1
	H_2O	e_h2o_ion_rcf_col_h2o_02_166_log.cs1
Recombination	H_2^+	e_H2p_rec_col_h2o_02_187_log.cs1
	OH^+	e_OHp_rec_col_h2o_02_112_log.cs1
	O_2^+	e_O2p_rec_col_h2o_02_112_log.cs1
	H_2O^+	e_H2Op_rec_col_h2o_02_186_log.cs1
	H_3O^+	e_H3Op_rec_col_h2o_02_178_log.cs1
Radiative cooling	H	cor52_rad_hi_9_2_41_048_1e_log_trd.cs1
	O	cor52_rad_oi_9_048_1e_log_trd.cs1
	O^+	cor52_rad_OII_8_048_1e_log_trd.cs1
	OH	e_OH_rad_log_trd.cs1

number density; $[N]$ is the number density of the neutral species; T_e is the electron temperature; and T_N is the temperature of the neutral species.

Figure 3.1 shows the momentum transfer energy loss rates used in the energy budget calculations, over the range of electron temperatures represented in the chemistry code outputs, for electrons on H, O, H_2, O_2, OH, and H_2O. With the exception of the rate for e-O_2 energy loss at low electron temperatures, polyatomic molecules dominate the electron momentum transfer losses. For the plasma sheet electrons in particular, H_2O is the primary energy sink. The momentum transfer energy losses are sustained predominantly by the cold electrons because of the dropoffs in the momentum transfer rate coefficients at hot electron temperatures and the scarcity of the heterogeneous electrons relative to plasma sheet electrons. To zeroth order, the momentum transfer losses of the hot electrons can be neglected.

Electron excitation-radiative energy losses The volumetric rate for electron excitation-radiative losses is

$$L_{eer} = \sum_{i=c,h} [N] \cdot [e_i] \cdot k_{ij}(T_{e_i}) \tag{3.33}$$

where $[N]$ is the neutral or ion species number density, $[e]$ is the electron number density and k_{ij} is the rate coefficient in erg cm^3 s^{-1}. For O_2 and H_2O, the dissociation energy losses and excitation-radiative losses have been combined into a total neutral energy loss.

Figure 3.2 shows the temperature dependence of the electron excitation-radiative energy loss rate coefficients. At cold electron energies, the rate coefficients vary significantly with temperature. The temperature dependence has largely leveled off in the hot electron energy range.

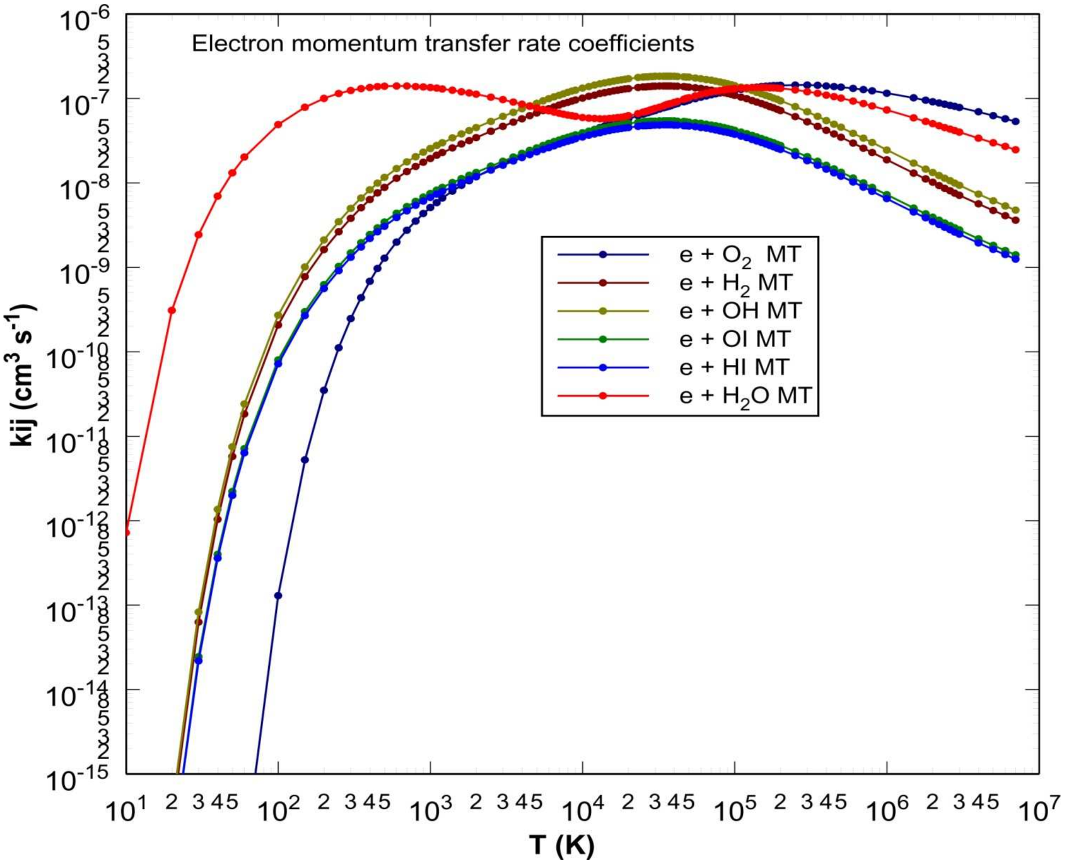

Figure 3.1 Momentum transfer energy loss rate coefficients for electrons on H, O, H_2, OH, O_2, and H_2O.

The momentum transfer energy loss rate coefficients are plotted over a temperature range spanning the hot and cold electron temperatures input to the chemistry code, coreqg.f90. Polyatomic molecules dominate the electron momentum transfer losses in the system, compared to losses for O and H. Water in particular dominates the electron momentum transfer losses at plasma sheet electron temperatures near 4 R_s ($\gtrsim 10^3$ K). The dropoff in momentum transfer rate coefficients at high temperatures causes the flattening of the curves in the heterogeneous electron temperature range ($> 10^6$ K). Data are taken from the momentum transfer data files compiled by Shemansky and listed in Table 3.1.

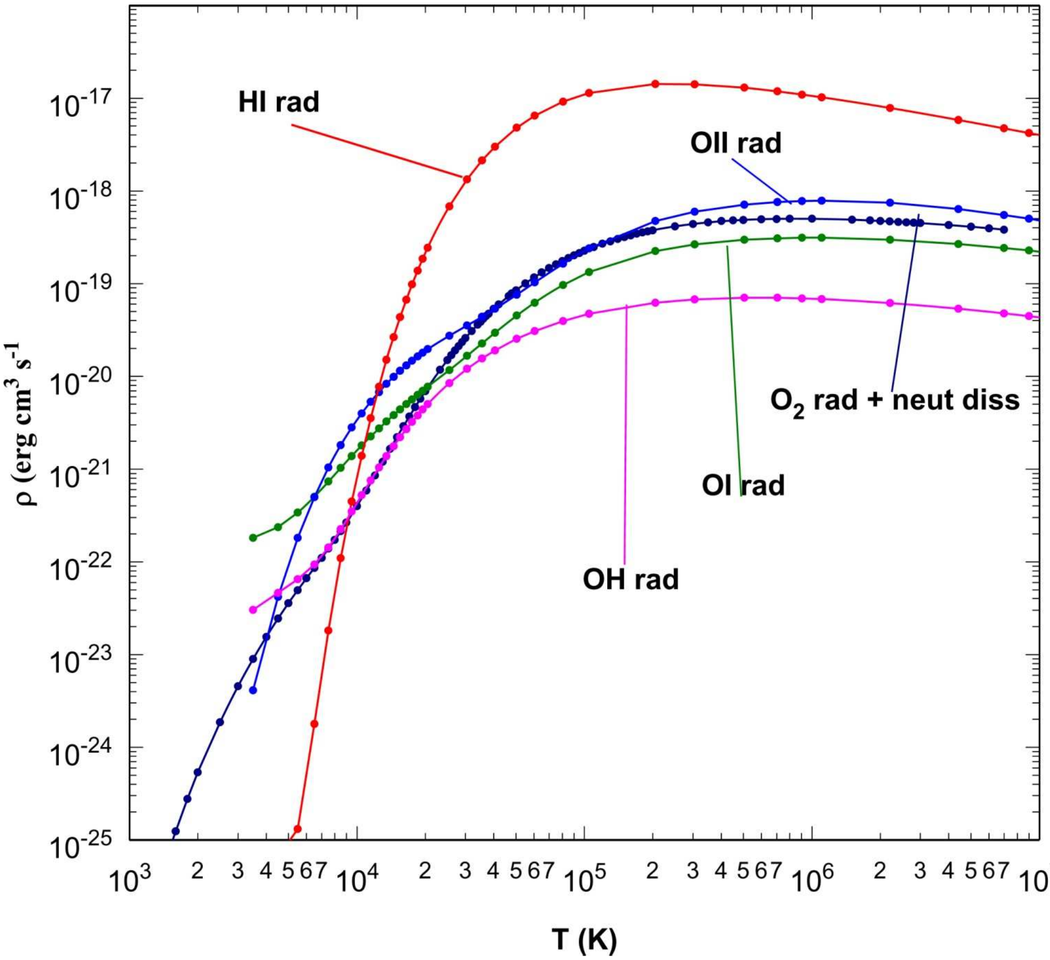

Figure 3.2 Electron excitation-radiative loss rate coefficients for neutral species. Electron excitation-radiative loss rate coefficients are plotted for H, O, O^+, and OH, and radiative + neutral dissociation loss rate coefficients for O_2. The rate coefficients vary significantly with temperature at plasma sheet electron temperatures ($\gtrsim 10^3$ K). In the temperature range of the heterogeneous electrons ($\gtrsim 10^6$ K), the temperature dependence has levelled off. Data taken from the radiative cooling data files compiled by Shemansky and listed in Table 3.1.

Ionization-related energy losses The volumetric rate coefficients $k_{ij}(T_e)$ for total electron impact ionization energy losses, in units of erg cm^3 s^{-1}, are tabulated in the data files listed in Table 3.1. Figure 3.3 shows the dependence of these rate coefficients on temperature, which is similar in form to that for radiative losses due to hot and cold electrons. The ionization loss rate coefficients are orders of magnitude smaller than the radiative cooling loss rate coefficients for plasma sheet electrons, but comparable for the heterogeneous electrons.

The electron pickup energy source rate is given by

$$S_{pkp} = [e_c] \cdot [N] \cdot k_{ion}(T_{ec})) \cdot (E_{pkp} + E_{ex}) \tag{3.34}$$

for impact ionization by plasma sheet electrons; by

$$S_{pkp} = [e_h] \cdot [N] \cdot k_{ion}(T_{eh}) \cdot (\overline{\Delta E_{ionpair}} - E_{ij} + E_{pkp}) \tag{3.35}$$

for impact ionization by heterogeneous electrons; and by

$$S_{pkp} = [N] \cdot g_{ij} \cdot (E_{ph} - E_{ij}) \tag{3.36}$$

for photoionization by photons with energy E_{ph}. Here, $[e]$ and $[N]$ are the electron and neutral number densities, respectively; $k_{ion}(T_e)$ is the total electron impact ionization rate coefficient as tabulated in the data files; E_{ij} is the ionization potential of the neutral species; E_{pkp} is the corotation energy of the plasma sheet electrons; $E_{ex} = \overline{Y} \cdot kT_{ec}$ is the Maxwellian weighted electron excess energy where $\overline{Y}$ is given by Equation 3.21;

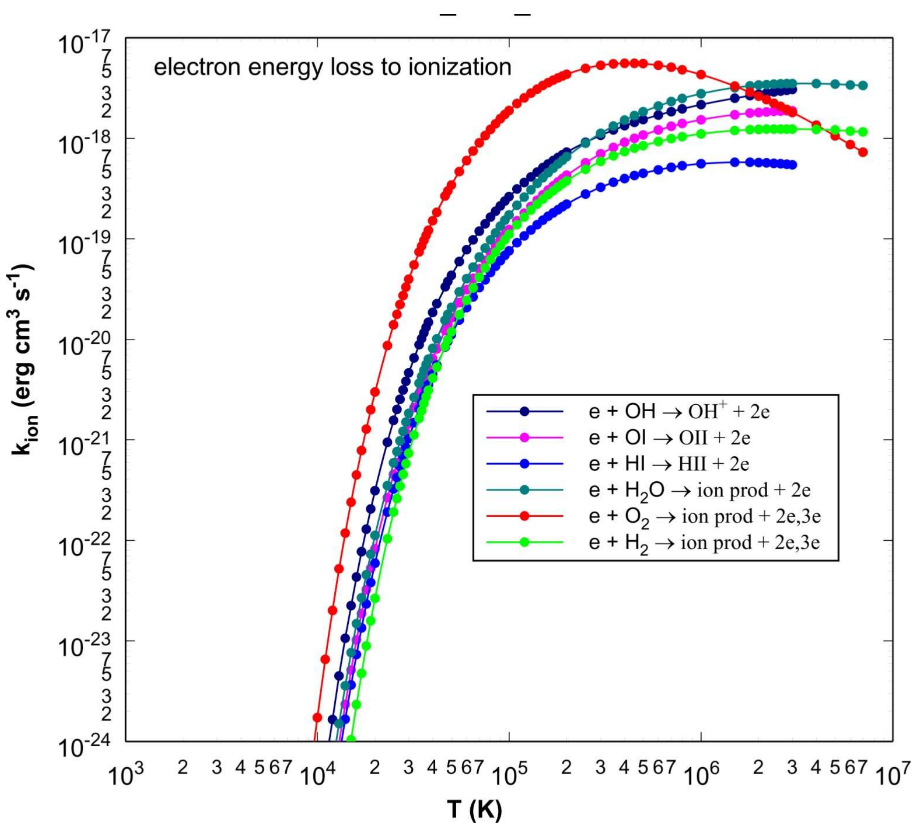

Figure 3.3 Electron ionization energy loss rate coefficients for neutral species. Curves are plotted for electron ionization losses on H, O, H_2, OH, O_2, and H_2O. As with the electron radiative cooling loss rate coefficients, the rate coefficients vary significantly with electron temperature for the plasma sheet electrons, but the temperature dependence levels off at the high heterogeneous electron temperatures. For the plasma sheet electrons, the ionization loss rate coefficients are a couple of orders of magnitude smaller than the radiative cooling loss rate coefficients. The rate coefficients are comparable for the heterogeneous electrons. Data are from the ionization and electron pickup energy data files compiled by Shemansky and listed in Table 3.1.

the energy quantity ($\overline{\Delta E_{ionpair}} - E_{ij} + E_{pkp}$) is the excess energy gained by the newly created cold electron from an ionization by a hot electron (c.f. Equation 3.22); g_{ij} is the photoionization rate; and E_{ph} is a mean photon energy, taken here to be the O 304 line (40.78 eV).

e-H_2O energy losses For H_2O, the electron energy losses for electron impact dissociation and radiative losses have been combined into a total neutral energy loss rate. Figure 3.4 compares the relative importance of the total neutral losses, total electron impact ionization losses, and the radiative losses over the temperature range spanned by the cold and hot electrons. The radiative loss curve is a byproduct of the calculations which went into the preparation of the total neutral energy loss rate data file; the radiative loss rate coefficient is not listed separately in the file. At hot electron temperatures, the impact ionization and dissociation losses predominate. On the other hand, the radiative loss is dominant for the cold electrons. The ionization loss is negligible for the plasma sheet electrons because their energies are below the ionization threshold for water. Water is the main energy sink in this chemical system.

3.3 Energy rate curves

A set of chemistry code outputs consists of simulations run with the input cold electron temperature and hot electron number densities varied over a selected range of values. The energy balance calculation is performed on each output in the set. The result is a set of curves for the plasma sheet electron energy rate, $\frac{dE_{ec}}{dt}$, vs. the hot electron density. The state of the gas at the plasma sheet electron energy equilibrium is evaluated

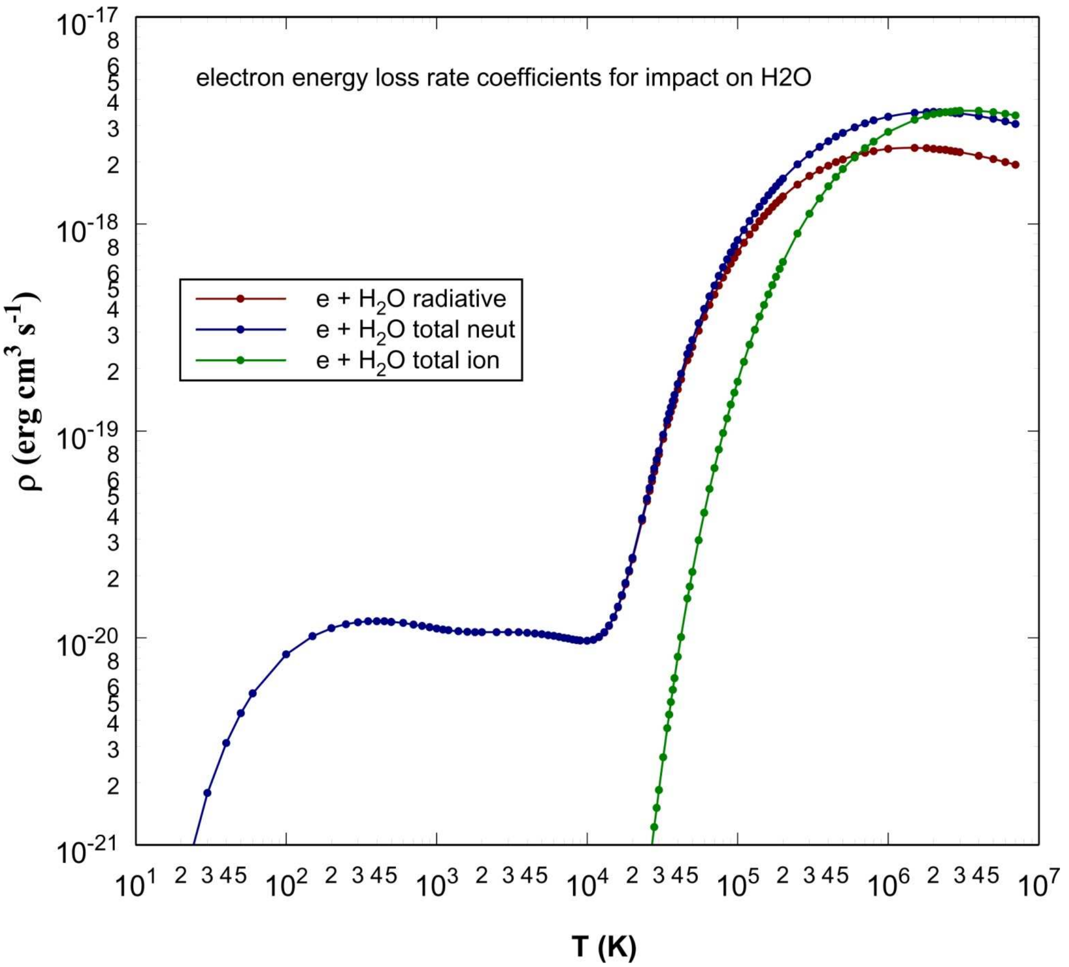

Figure 3.4 Comparison of energy loss rates for e-H_2O processes.
Energy loss rate coefficients for radiative, total neutral, and total ionization losses in electron impacts on H_2O. Total neutral process losses are the combination of radiative cooling and momentum transfer. At lower electron temperatures (i.e., plasma sheet electron temperatures), radiative cooling losses dominate the total neutral process losses, while total ionization losses (which include ionization and electron pickup energy losses) are insignificant below the ionization potential of water, 12.6 eV or 1.46×10^5 K. At higher temperatures, ionization losses and momentum transfer losses dominate while radiative cooling is a minor loss process. H_2O is the main energy sink in the inner magnetosphere. Data are from the H_2O energy data files compiled by Shemansky and listed in Table 3.1.

at the zero crossings, $\frac{dE_{ec}}{dt} = 0$ erg s^{-1}, by interpolating the gas species populations from the chemistry code outputs. The equilibrated plasma sheet electron temperature is interpolated at the zero crossing from the input cold electron temperatures.

Chapter 4

Results

The objectives of this research are to investigate the effects on the inner Saturn magnetosphere of the heterogeneous hydrogen sourced from the top of the atmosphere and to examine the sensitivity of the chemical system to the plasma sheet electron state and the system energy input. To this end, the chemistry code was run for a range of values in its input parameters.

4.1 Standard chemistry code input parameter set

Only three of the input parameters for the chemistry code are of importance: cold electron temperature and number density, and hot electron number density. A single value of heterogeneous electron temperature, $T_{eh} = 10^7$ K, was used because of the weak dependence on temperature of the rate coefficients for the reactions in the system at high temperatures.

The cold electron temperature in the chemistry code input files varied from 3500 K to 36,000 K based on the data of Schippers et al.[82] near 4 R_s. To explore the sensitivity to plasma sheet electron density n_{ec}, three values (50 cm^{-3}, 75 cm^{-3}, and 100 cm^{-3})

were selected based on the equatorial electron number densities ranging from 40 to 80 cm^{-3}[97]. To examine the effects of varying the energy input to the magnetospheric gas, the hot electron number density n_{eh} was varied from 0.004 cm^{-3}, extrapolated from Schippers et al., up to 20 cm^{-3}; a higher number density corresponds to a higher energy input into the system.

The initial state of the system was 100% H_2O. The populations of all species other than H were solved iteratively. The hydrogen forcing from the Saturn atmosphere was represented by fixing the population of atomic hydrogen in the input files for coreqg.f90 at a representative value of 500 cm^{-3}; the range cited by Shemansky et al.[94] is 450 to 1600 cm^{-3}. The H population was iterated in the calculations modelling the chemistry without the hydrogen forcing. The observed broad distribution of O and OH is indicative of the mean kinetic energy. The diffusion coefficients, D_O for O and D_{OH} for OH, in the water chemistry architecture file were treated as adjustable parameters. Simulations have been run for several sets of D_O and D_{OH}. One representative set of results is presented here.

4.2 A representative set of results

Results are shown for one set of diffusion coefficient values, $D_O = 2.0 \times 10^{-7}\ \mathrm{s}^{-1}$ and $D_{OH} = 1.4 \times 10^{-7}\ \mathrm{s}^{-1}$ based on estimated lifetimes of 60 and 83 days, respectively, for the O and OH. With higher energy inputs, higher ionization levels would be expected in the gas, in the absence of externally imposed energy sinks. Without the atmospheric hydrogen forcing, fully ionized plasma can be obtained. However, if the atmospheric hydrogen is present, ion-dominated states do not occur.

To represent graphically the effects of the atmospheric hydrogen forcing, total neutral to total ion ratios are plotted for each pair of (hot electron number density, cold electron temperature) values. The outcomes of the chemistry are binned into neutral/ion ratios of: greater than 100.0; between 1.0 and 100.0; between 0.01 and 1.0; and below 0.01. Chemistry code outputs which failed to converge are marked by an 'X'. A set of plots for a plasma sheet electron density of 50 cm^{-3} are shown here; Figure 4.1 shows outputs in the absence of the hydrogen forcing and Figure 4.2 the outputs in the presence of the forcing.

The hydrogen forcing also stabilizes the chemical system: with the forcing present, the gas does not attain a plasma-dominated state and remains neutral-dominated, even for large energy inputs. The plots for plasma sheet electron densities $n_{ec} = 75$ and 100 cm^{-3}, and for other values of D_O and D_{OH}, are qualitatively similar to Figures 4.1 and 4.2. Calculations limited by the measured heterogeneous H population are considered here, in order to maintain physical realism.

The net plasma sheet electron energy balance was calculated using the species populations in the chemistry code outputs. This energy calculation is based on the equatorial plasma sheet electron density of ~50 cm^{-3} reported at 4 R$_s$ by Sittler et al.[97]. Curves for plasma sheet electron energy rate $\frac{dE_{ec}}{dt}$ are plotted in Figure 4.3. Each curve represents a different value of hot electron number density. $\frac{dE_{ec}}{dt}$ curves which fail to attain a value of zero are not shown. Note that $\frac{dE_{ec}}{dt} \neq 0$ indicates a mismatch between the input values of T_{ec} and n_{eh}. If the plasma sheet electron energy rate is negative, the plasma

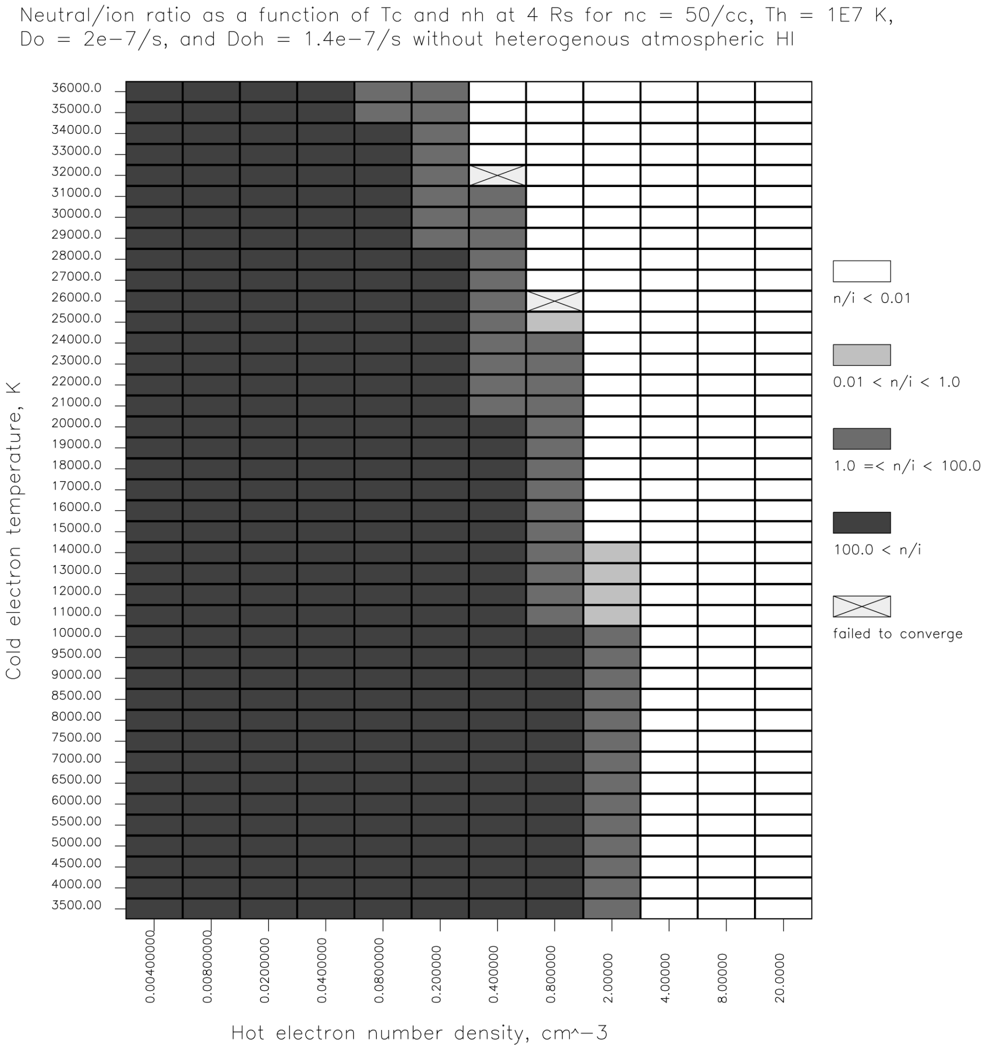
Neutral/ion ratio as a function of Tc and nh at 4 Rs for nc = 50/cc, Th = 1E7 K, Do = 2e−7/s, and Doh = 1.4e−7/s without heterogenous atmospheric HI

Figure 4.1 Neutral/ion ratios from chemistry code outputs in the absence of atmospheric hydrogen forcing.

The inputs to the chemistry code are: $n_{ec} = 50$ cm^{-3}, $T_{eh} = 10^7$ K, $D_O = 2 \times 10^{-7}$ s^{-1}, $D_{OH} = 1.4 \times 10^{-7}$ s^{-1}, $n_{eh} = 0.004$ to 20 cm^{-3}, and $T_{ec} = 3500$ to 36,000 K. Initial gas state is 100% H_2O. The population of H is iterated. Total neutral to ion ratios are plotted against T_{ec} and n_{eh}, drawn in darker to lighter shades of gray as the degree of ionization increases. Outputs which failed to converge are crossed out. At lower heterogenous electron densities, i.e. smaller energy inputs into the gas, the gas remains neutral. When the heterogenous electron density is high, i.e. larger energy input, the final state of the gas can be a plasma. The energy balance of the system is not taken into account by the chemistry code and must be calculated separately; only energy equilibrated outputs are valid.

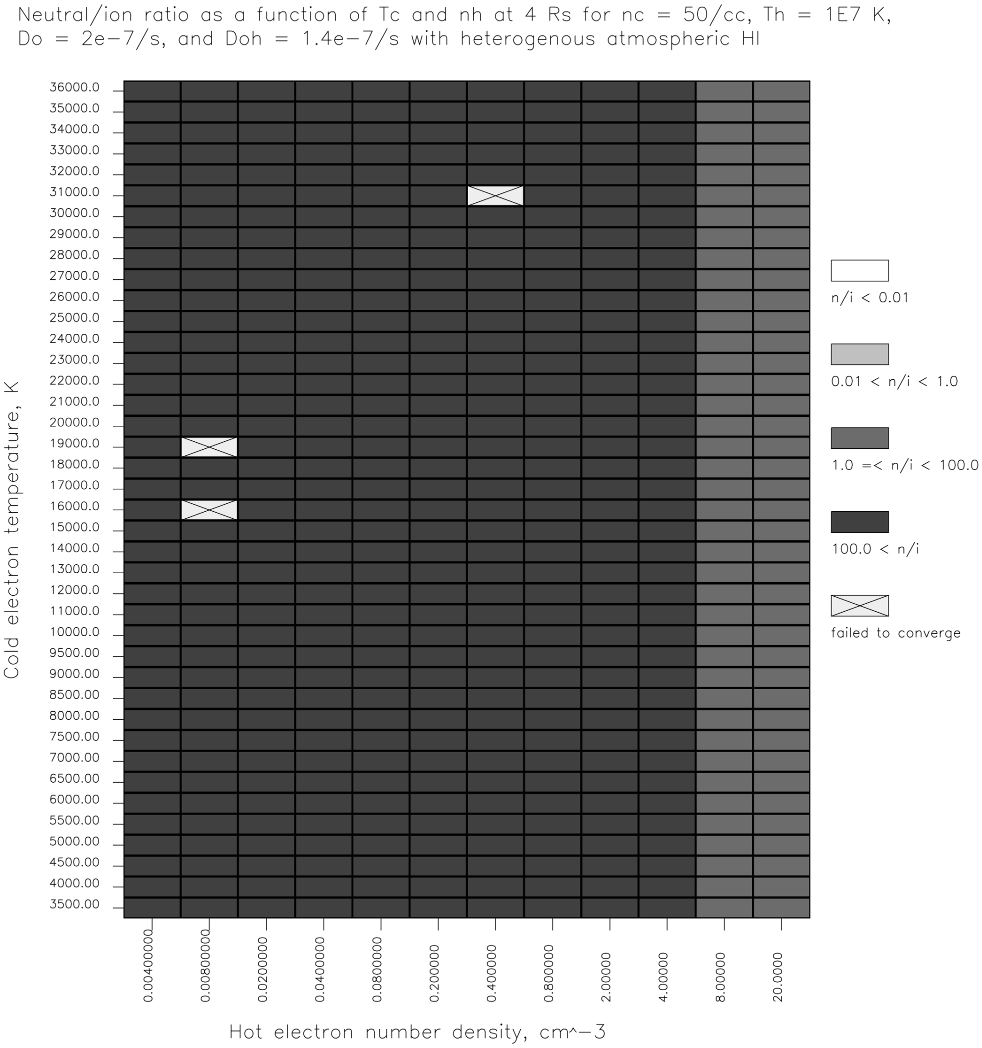

Figure 4.2 Neutral/ion ratios from chemistry code outputs in the presence of atmospheric hydrogen forcing.
The inputs to the chemistry code were the same as in Figure 4.1: $n_{ec} = 50$ cm^{-3}, $T_{eh} = 10^7$ K, $D_O = 2\times10^{-7}$ s^{-1}, $D_{OH} = 1.4\times10^{-7}$ s^{-1}, $n_{eh} = 0.004$ to 20 cm^{-3}, and $T_{ec} = 3500$ to 36,000 K. The initial state of the magnetospheric gas was 100% H_2O, and the population of H was fixed to the observed value of 500 cm^{-3} to represent the atmospheric hydrogen forcing. This large flux of hydrogen quenches the plasma: none of the chemistry code outputs are ion dominated. The atmospheric hydrogen maintains the neutral state of the inner magnetosphere. The energy balance of the system is not taken into account; a separate calculation is needed to determine which chemistry code outputs are in energy equilibrium.

sheet electrons lose energy; to achieve energy balance, T_{ec} must decrease and/or a higher energy input, i.e. n_{eh}, would be required. On the other hand, if $\frac{dE_{ec}}{dt} > 0$, the plasma sheet electrons have a net energy gain; the input T_{ec} is too low and/or the heterogeneous electrons supply an excess of energy to the system (n_{eh} is too high).

In the real-life magnetosphere, the only way to jump from one $\frac{dE_{ec}}{dt}$ curve to another would be if the heterogeneous electron flux were to change; if the hot electron flux is unchanged, the plasma sheet electron temperature must adjust to the imposed energy deposition. The tendency for T_{ec} is therefore to move along the appropriate curve toward the zero crossing point, if there is one. Not every value of n_{eh} has a curve which crosses $\frac{dE_{ec}}{dt} = 0$; in these cases, no energy equilibrated state exists for the corresponding energy deposition rate. The statistically equilibrated gas compositions with $\frac{dE_{ec}}{dt} \neq 0$ are interpreted as transient states which relax to the energy equilibrated state (zero crossing point on the appropriate plasma sheet electron energy rate curve) where possible.

The equilibrated plasma sheet electron temperatures T_{eq}, i.e. the temperatures at the zero crossings of the curves, are forced by the hot electrons. Increasing n_{eh}, i.e. increasing the energy available to the system, raises the cold electron temperature in the energy equilibrated state. Values of n_{eh} ranging from 0.02 to 0.8 cm^{-3} force plasma sheet electron temperatures of 14,000 to 18,500 K. Notably, each $\frac{dE_{ec}}{dt}$ curve crosses the net zero energy rate at a distinctly defined equilibrated value of T_{ec}. The high slope at the net zero energy rate crossings indicates that the physical system will show a rapid response to changes in the system forcing.

Figure 4.4 plots neutral species populations for the $\frac{dE_{ec}}{dt} = 0$ crossing points, as interpolated from the chemistry code outputs. Populations for the $n_{ec} = 100$ cm^{-3} cases

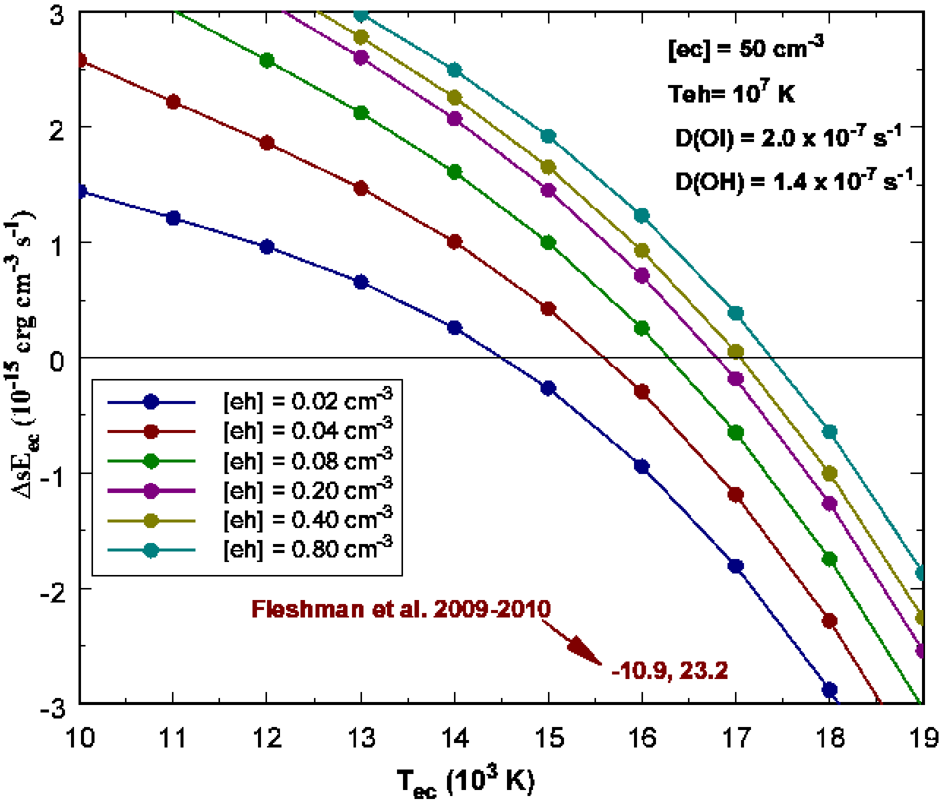

Figure 4.3 Net energy rate curves.
The energy balance calculation calculates the net energy rate, $\frac{dE_{ec}}{dt}$, into the magnetospheric gas. Plotted are curves for $n_{ec} = 50$ cm^{-3}, $D_O = 2.0 \times 10^{-7}$ s^{-1}, and $D_{OH} = 1.4 \times 10^{-7}$ s^{-1}. Each curve represents a different value of heterogeneous electron density. The plasma sheet electron temperatures at the net zero energy rate crossings, $\frac{dE_{ec}}{dt} = 0$, are the equilibrated plasma sheet electron temperatures T_{eq} that are forced by the heterogenous electrons. Curves which failed to provide equilibrated values of T_{eq} are not shown. When $\frac{dE_{ec}}{dt} \neq 0$, the tendency is for the plasma sheet electron temperature to relax along the curve to T_{eq}. Increasing the energy input (i.e., increasing n_{eh}) increases the equilibrated plasma sheet electron temperature. Each $\frac{dE_{ec}}{dt}$ curve has a distinctly defined value of T_{eq}. n_{eh} ranging from 0.02 to 0.8 cm^{-3} forces T_{eq} = 14,000 to 18,500 K. The high slope at the zero crossings indicates the gas system is highly sensitive to changes in the hot electron forcing. If the hot and cold electron parameters from the model output of Fleshman et al.[23] are used as inputs to the chemistry code and the energy balance is calculated on the chemistry output, the energy balance calculation yields $\frac{dE_{ec}}{dt}$ = -10.9 on the scale of the plot, at $T_{ec} = 2$ eV.

and the equilibrated plasma sheet electron temperatures for $n_{ec} = 50$ cm^{-3} are shown. At both plasma sheet electron population levels, higher heterogeneous electron densities, i.e. system energy inputs, result in lower total neutral densities and higher T_{eq} values. The major neutral species are O, H_2O, OH, and H. The only neutral species whose population does not decrease with increased energy deposition is H, which is maintained by the Saturn atmospheric ouflow. O_2 in particular is rapidly destroyed as the energy input increases. The O and OH populations track each other fairly closely.

Figure 4.5 plots the ion populations at the energy equilibrium points for $n_{ec} = 50$ cm^{-3}. On this scale, O_2^+ is below threshold. H_2O^+ and H_3O^+ dominate the ion populations. The equilibrated plasma sheet electron temperature is also shown. The dramatic increases in O^+ and H^+ with n_{eh} are explained as follows: the neutral gas is primarily responsible for destroying O^+ and H^+. As the energy input to the system increases, there is less neutral mass available to destroy these ions, and their populations increase as a result.

Figure 4.6 shows the energy relaxation time – a measure of how quickly a species respond to changes in conditions – as a function of n_{eh}. If the energy balanced magnetospheric gas suddenly had its energy inputs from the heterogeneous electrons and solar flux removed, the energy relaxation time represents the initial decay time. Charge neutrality requires that the electron density equals the total ion density; hence, the overall ion energy relaxation time must be equivalent to the plasma sheet electron energy relaxation time. Curves are shown for $n_{ec} = 50$ and 100 cm^{-3}.

As the hot electron number density increases, the decrease in the total neutral mass means the relaxation times for O^+ and H^+ increase. The inferred plasma sheet electron

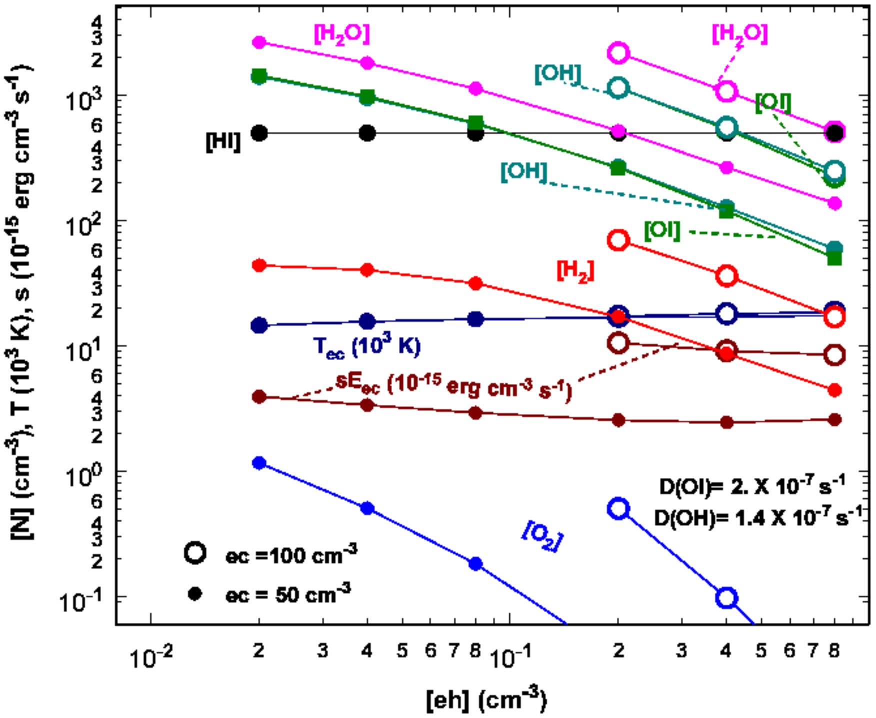

Figure 4.4 Neutral species partitioning for the plasma electron energy equilibrated system as a function of heterogeneous electron population.

The species partitioning is calculated at the zero crossing points in Figure 4.3. Plotted here are neutral populations as a function of hot electron density. Even though the curves are labelled by the value of the equilibrated plasma sheet electron temperature T_{eq} rather than by heterogeneous electron density as in the previous figure, the color coding is the same. Populations are plotted for the plasma sheet electron densities of 50 cm^{-3} and, for comparison, 100 cm^{-3}. O, H_2O, OH, and H are the major neutral species. Higher energy inputs, i.e. higher n_{eh}, lead to lower total neutral densities. In particular, O_2 is rapidly destroyed as the energy input increases. The only neutral species whose population does not decrease with increasing n_{eh} is H, which is maintained by the atmospheric flux. The O and OH populations track each other closely.

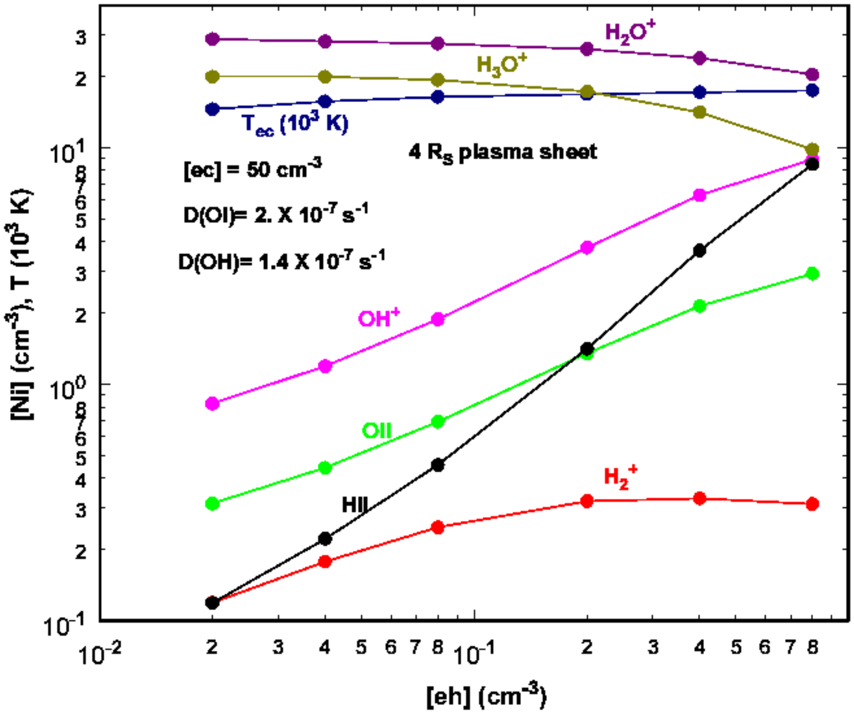

Figure 4.5 Ion species partitioning for the plasma sheet electron energy equilibrated system as a function of heterogeneous electron density.

Ion species partitioning corresponding to the neutral species partitioning plotted in Figure 4.4. The equilibrated plasma sheet electron temperatures T_{eq} are also shown. O_2^+ is too small to be plotted on this scale. The dominant ions are H_2O^+ and H_3O^+. As the energy input increases, T_{eq} also rises and the populations of O^+ and H^+ increases dramatically. The neutral gas is the main destroyer of O^+ and H^+. Because the total neutral density decreases as n_{eh} and hence the energy input increases, there is less neutral mass available to destroy these ions and their populations therefore increase. Despite the growth of the O^+ and H+ populations with increasing hot electron density, the molecular ions remain dominant, an unexpected result.

relaxation time is shorter (less than 10 days) than the relaxation times for the neutral species. The flatness of the curves for O and OH indicates that for these species, τ is driven by the diffusive losses, not by n_{eh}. The relaxation time for O, around $30 - 40$ days, is longer than the ∼14 day time scale seen in the 2004 oxygen surge detected by UVIS[20].

4.3 Comparison against other models

In order to allow comparison against other models, a nominal neutral to electron ratio of ∼60 was selected and the gas species populations interpolated from the energy equlibrated solutions. Table 4.1 compares the populations for this model with a neutral/electron ratio of 57 to observations. There is a substantial level of agreement, suggesting the pure gas phase H_2O chemistry is not strongly affected by the presence of water clusters or grains. However, Sittler et al.[97] report a higher density for H_3O^+ than for H_2O^+, in contrast to the current model.

Direct comparison to the Cassidy and Johnson model[13] is difficult, as the focus of their model is on the dynamics of the neutral gas particles rather than on the chemistry. The physical processes they consider, namely the plasma/UV processes of charge exchange, ion/neutral scattering, and molecular dissociation, and the neutral/neutral collisions introduced in their model, overlap to a large degree with the processes included in the current model. The exception is neutral/neutral collisions, which in the current model are considered only in the context of neutral-neutral chemical reactions. On the

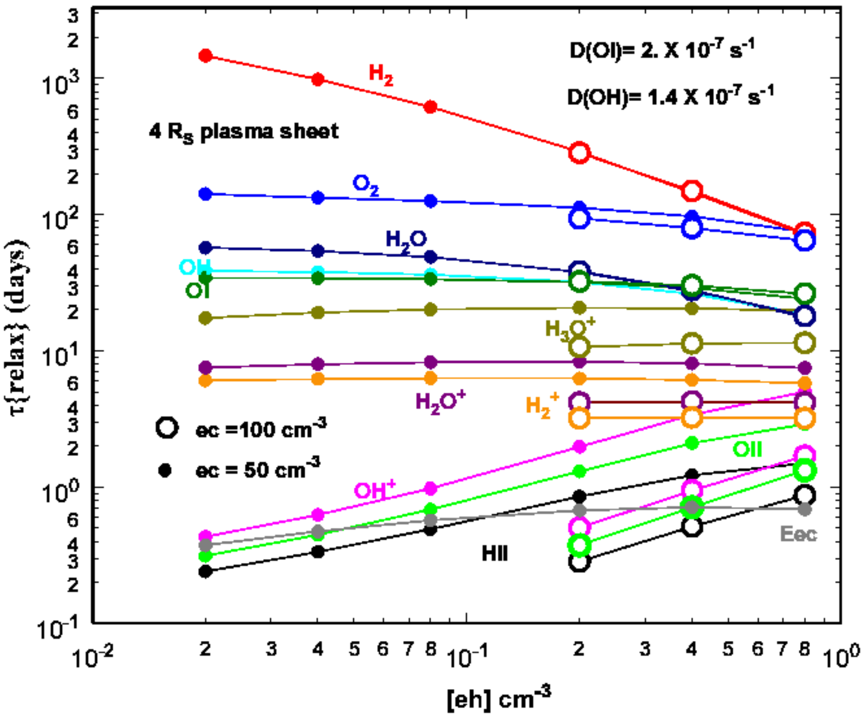

Figure 4.6 Energy relaxation times for the electron energy equilibrated system. The energy relaxation time τ represents the initial decay time of the energy equilibrated magnetospheric gas in the event the energy inputs (heterogeneous electrons and solar flux) were suddenly removed. The relaxation times for the individual species are plotted as functions of hot electron density. Plasma sheet electron densities are 50 and 100 cm^{-3}. The increase in relaxation times for O^+ and H^+ as the heterogeneous electron density increases is a consequence of the resulting decrease in the total neutral mass available to destroy these ions. The plasma sheet electron energy relaxation time must equal the overall ion energy relaxation time because of charge neutrality. The plasma sheet electron relaxation time inferred from the ion species relaxation times is less than 10 days, shorter than the relaxation times for the neutral species. The plasma electrons would be expected to disappear more rapidly than the neutrals cool down. The curves for O and OH are not strongly dependent on n_{eh}; diffusive losses are the main determinant of their relaxation times. The relaxation time for O is 30 to 40 days. The ∼14 day time scale for changes in the O 1304 Å emission during the 2004 oxygen surge (Figures 1.7 through 1.10) is less than half the relaxation time derived from the energy balance calculation. Further exploration of diffusion coefficient values for O and OH is warranted.

Table 4.1. Comparison of model and observation populations at 4 R_s

Item	Observed	Nominal model
[N]/[e]	60 – 30[a b]	57
T_{ec}, K	⋯	16,343
[e_c], cm^{-3}	50[a]	50
[H_2O], cm^{-3}	⋯	1128
[H_2O]ℓ[c] , 10^{13} cm^2	1.5 – 1.75[d]	1.69
[OH], cm^{-3}	670[b]	594
[O], cm^{-3}	750[b]	602
[H], cm^{-3}	500[e]	500[f]
[H_3O^+], cm^{-3}	23[a]	19.2
[H_2O^+], cm^{-3}	7.5[a]	27.5
[OH^+], cm^{-3}	11[a]	1.9
[O^+], cm^{-3}	10[a]	0.7
[H^+], cm^{-3}	⋯	0.5
Energy supplied to plasma sheet electrons, GW	⋯	4.1[g]
H_2O source rate, 10^{27} s^{-1}	6.5[h]	4.0

[a] Sittler et al.[97]

[b] Melin et al.[67]

[c] ℓ is the scale height, ∼2.5 R_s[97].

[d] Hartogh et al.[35]

[e] Shemansky et al.[94]

[f] Population of H was fixed to the observed value by Shemansky et al.[94] in Enceladus pointed observation.

[g] Earlier estimate from Esposito et al.[20] was 14 GW.

[h] Hansen et al.[33]

other hand, some key processes in the current model, specifically momentum transfer between electrons and other species, ionizations (electron impact or photo), recombinations, and neutral-neutral reactions are not included in their model, nor is the energy balance of the plasma sheet electrons considered. In addition, the function form of their charge exchange cross section,

$$\sigma_{CE} = 2 \times 10^{-14.8} E^{-0.18} \tag{4.1}$$

(where E is the center of mass reference frame energy of the ion/neutral pair and σ_{CE} is in cm^{-3}) is quite different from the analytic formulations, e.g. Equation 2.7, fitted to charge exchange cross section data from the literature.

The H_2O source rate calculated by Cassidy and Johnson is 10^{28} molecules s^{-1}, and the neutral water group density (consisting of H_2O, OH, and O) they report is 1 to a few 10^3 cm^{-3} around 4 R_s (and up to 10^4 cm^{-3} in the vicinity of Enceladus). These figures are compatible with the current model. On the other hand, their conclusion that neutral-neutral collisions are required alongside the plasma/UV processes to explain the morpohlogies of the O and OH clouds is not in agreement with the chemistry in this model, where such collisions are at best a minor component of the chemistry and play no role in the plasma sheet electron energy balance.

The species partitioning of the Fleshman et al. chemistry model[23] is shown in Table 4.2 along with the output of the present chemistry model run using the Fleshman et al. hot and cold electron parameters as inputs: T_e = thermal electron temperature = 2 eV (23,208 K), T_{eh} = hot electron temperature = 160 eV, n_e = total electron density = 60 cm^{-3}, and f_{eh} = fraction of total in hot electrons = 0.46%, from which n_{ec} =

59.724 cm^{-3} and $n_{eh} = 0.276\ \mathrm{cm}^{-3}$ in the present model. The Fleshman et al. model does not include heterogeneous atmospheric hydrogen, so $[H]$ was iterated in the present calculation rather than held to a fixed value. The Fleshman et al. model does not include reactions producing O_2 as a species.

While there is a fair degree of agreement in the populations of some species between the two models, e.g. H_2O and H_2O^+, there are order of magnitude discrepancies in the OH, H, and O populations. The chemistry code output yields a plasma sheet electron energy rate of $\frac{dE_{ec}}{dt} = -1.09 \times 10^{-14}$ erg cm^{-3} s^{-1} for the Fleshman et al. conditions, corresponding to a data point of (-10.9, 23.2) on the axis scales used in Figure 4.3. The imposed value of $T_{ec} = 2$ eV produces a large net energy loss and a depleted neutral population in the present model that is in fundamental disagreement with the Fleshman et al. model. Fleshman et al. state that their model solves density and energy rate equations for each species, but their energy calculations exclude momentum transfer. It is also not clear whether their stated rate equations apply to the hot and plasma sheet electrons: the number density of the plasma sheet electrons is a constraint in their model while the fraction of hot electrons is one of the free parameters which is varied in their random walk calculation, so there is a question about the degree to which the number density and energy rate equations apply to the two electron populations.

Given the aforementioned reservations about their methodology and the lack of details given about their calculations (c.f. Section 2.6), it is not possible at this time to resolve the discrepancies between the Fleshman et al. model output and the present calculation. Energy balance in the plasma sheet electrons is critical, and there is no indication that Fleshman et al. addressed this in their calculations. In any case, the plasma sheet electron

Table 4.2. Comparison of species partitioning (cm^{-3}) for Fleshman et al.[23] vs. current model

Species [a]	Fleshman [b]	Current model [c]
H_2O	190	203.4
O_2	··· [d]	35.4
H_2	$\ll 1$	2.1
OH	770	72.1
H_3O^+	9.8	15.5
H	720	178.2
O	700	263.9
H_2O^+	20	23.0
OH^+	17	7.2
H_2^+	$\ll 1$	0.14
H^+	4.6	5.0
O^+	8.4	7.6
O_2^+	··· [d]	1.6
O^{2+}	0.078	··· [e]

[a] Electron parameters: plasma sheet electron density is 59.724 cm^{-3} and temperature is 2 eV; heterogeneous electron density if 0.276 cm^{-3} and temperature is 160 eV. Total electron density is 60 cm^{-3}.

[b] Total neutral density: 2380 cm^{-3}

[c] Total neutral density: 754 cm^{-3}

[d] O_2 and O_2^+ are omitted in the Fleshman et al. model.

[e] O^{2+} is omitted from the current model.

temperature in the Fleshman et al. work was a value that was fixed without considering the plasma sheet electron energy balance, but on the basis of a very uncertain value from the Schippers et al.[82] observational data.

Chapter 5

Discussion and conclusions

This work presents a first examination of the role played in the chemistry of the inner magnetosphere by the hydrogen forcing from the top of Saturn's atmosphere and the plasma electron energy balance. These results model the required rate of H_2O injection and total power deposited in the plasma sheet at 4 R_s. For the first time, detailed energy balance calculations have been used to establish a direct relationship between the forcing energy input and the state of the ambient plasma sheet electrons in a magnetosphere model. The energy deposition rate required to maintain the magnetospheric gas system, basic lifetimes (to be compared against observation), and the state of the gas have been determined. This investigation based on a gas phase-only chemistry model has some limitations vis a vis water source rates given the likely presence of icy particulate matter in the Enceladus plume and uncertainties in the observed plasma state. Nevertheless, the current pure gas phase H_2O model shows basic agreement with observation for the core of the plasma sheet. As a preliminary work, there are a number of unresolved issues which have not yet been addressed.

5.1 Icy grains and the water source rate

Although the current model does not require the participation of chemically active icy particulates, the density of icy grains in the Enceladus plume does affect the water source rate calculation. The presence of the additional H_2O molecules in a cluster decreases the ionization potential of H_2O from the single-molecule value of 12.6 eV. Belau et al.[6] report VUV photoionization potentials for $(H_2O)_n$, with n ranging up to 79, converging to a value of 10.6 eV for $n = 23$. The cations $[(H_2O)_n]^+$ are unstable and tend to emit OH through

$$(H_2O)_n + h\nu \rightarrow [(H_2O)_n]^+ + e \rightarrow (H_2O)_{n-1}H^+ + OH^* + e \tag{5.1}$$

leaving protonated water clusters $(H_2O)_nH^+$. The proton attaches to one of the water molecules to form H_3O^+.

High dissociative recombination coefficients have been reported for cluster ions compared to molecular ions[5]. The rate coefficients are typically an order of magnitude or more larger than the corresponding molecular dissociative recombinations. In the case of $H_3O^+(H_2O)_n$, Johnsen [43] reported that measured recombination coefficients increased as the cluster size n increased. The dissociation energy to separate H_3O^+ from the H_2O molecules is low compared to the dissociation energy of H_2O (5.16 eV for dissociation into OH and H), with 1.56 eV reported for the separation of $H_2OH^+H_2O$ into H_2O and H_3O^+[5].

Bates concluded that the dissociative recombination of the H_3O^+ would only release 4.84 eV, not enough energy to produce electronic excitation in the products of the recombination[5]. The binding energy reported for water dimers is around 0.2 eV[72]; for larger clusters (up to $n = 19$), a typical binding energy per H_2O molecule is on the order of 0.4 eV based on theoretical calculations by Su et al.[107]. The implication is that the energy released by dissociative recombination of the H_3O^+ in a water cluster would tend to dissociate the clusters rather than creating subsequent dissociation products out of the H_2O molecules. This is borne out by the experimental data on dissociative recombination of $D^+(D_2O)_2$ clusters by Någård et al., who reported branching ratios of 0.94, 0.004, and 0.02 for the products 2 D_2O + D, D_2 + OD + D_2, and D_3O + D_2O, respectively.

If the Enceladus plume contains a substantial fraction of its output in the form of small water clusters, which are more easily ionized than water molecules and upon encountering an electron would recombine and break apart into n H_2O molecules, the current model would underestimate the source rate of H_2O. The effect of clusters large enough that the 4.84 eV of energy released from the recombination of H_3O^+ is insufficient to break apart all molecules in the cluster (perhaps on the order of $n \sim 25$; icy E ring grain-sized particles would fall into this category) is more difficult to quantify, but here too one could reasonably expect several water molecules to be produced rather than a single molecule, and thus the current model would again underestimate the water source rate. The caveat is that these icy particles would need to escape Enceladus and enter orbits in the magnetosphere to have any effect on the chemistry. Water molecules produced by the breakup of clusters would be indistinguishable from those originating from the vapor, so clusters could not be detected in this manner. Ionized water clusters can be detected, e.g. $H^+ \cdot (H_2O)_n$ and $Na^+ \cdot (H_2O)_n$ are present in the Enceladus plume[77]. However, because the results of the current model are compatible with the recent Enceladus water torus measurements by the ESA space observatory Herschel[35], the effects of icy particles on the chemistry are likely to be small.

5.2 Future directions at 4 R_s

This work should be considered a preliminary exploration of the parameter space governing the chemistry of the Saturn magnetosphere in the E ring region. Results for a single set of nonzero diffusion coefficients for O and OH has been presented here. Because a family of solutions for the electron energy equilibrated gas state is possible, observation data are required for guidance. The present model is thus limited by the observed electron, ion and neutral populations. The currently available measurements of OH, O, H, and H_2O provide basic limits to the model. Density maps are anticipated from the direct observation of H_2O from Herschel, which will complement the Cassini observations.

The calculation of the total energy deposition and H_2O source rates required to maintain the system depends on the observed spatial distribution of the plasma sheet; the spatial distribution of water is assumed to match that of the plasma sheet core. The heterogeneous electron forcing is measured at a statistically very low level, so mean energy deposition rates are not determined. The Sittler et al.[97] plasma electron contour map defines the basic spatial structure of the plasma sheet core. However, the plasma sheet electron temperatures cannot be precisely determined because of spacecraft charging effects, and electron densities are determined through charge neutrality rather than by direct observation. Model calculations are therefore required to determine the state of the plasma. Despite the uncertainties in the currently available plasma sheet measurements, the current model's water source rate is in satisfactory agreement with the Enceladus plume source rate as measured in the Casisni occultation measurements[33].

The lifetimes derived from the current model appear inadequate to explain rapid population changes such as the oxygen surge observed by UVIS in early 2004[20]. It is fairly likely that other reactions will need to be added to more closely model the observed behavior. Such experiments may help narrow down the possibilities for the as yet unknown process(es) responsible for such a rapid decay in the oxygen population. Determining these processes may involve altering the water chemistry architecture file to use species other than water as the diffused-in replacement for heavy particles lost from the system.

5.3 Future directions in the magnetosphere

In the longer term, water architecture files will be developed to model the conditions at other locations in the E ring region. Initial efforts would focus on other locations in the ring plane, such as the locations covered by the HST observations[95] or the Schippers et al. model[82]. The main differences with respect to conditions at 4 R_s would be: changes in the escape energy mean different products could be retained or lost; different kinetics mean diffusion coefficients would take on a different range of feasible values; and depending on the locally accessible gas sources, the input temperatures for both neutral and ionic species will vary with location. Eventually, off-plane simulations would need to be run, and the modelling extended to the outer magnetosphere, in order to produce maps similar to those derived from observations. Expansion of the model beyond 4 R_s will allow the refinement of neutral species diffusion rates and set limits on other sources.

5.4 Conclusions

This work presents a chemistry model and associated energy budget calculation for the inner Saturn magnetosphere. The outflow of heterogeneous HI from the top of the Saturn atmosphere quenches plasma formation to the extent that even with large energy inputs from heterogeneous electrons, the magnetospheric gas remains dominated by neutrals. The species partitioning derived from the current model, for plasma electron energy equilibrated solutions and the implied water source rate are compatible with observations. The gas phase water-based chemistry in the current model is sufficient to explain the observed inner magnetosphere populations without the need to add chemistry involving water clusters, E ring grains, or icy surfaces. The detailed energy balance calculations determine the energy deposition rate into the inner magnetosphere, and for the first time, to relate the heterogeneous electron forcing to the state of the ambient plasma sheet.

References

[1] M.H. Acuña, J.E.P. Connerney, and N.F. Ness. The Z_3 Zonal Harmonic Model of Saturn's Magnetic Field: Analyses and Implications. *J. Geophys. Res.*, 88:8771–8778, 1983.

[2] L.H. Andersen, O. Heber, D. Kella, H.B. Pedersen, L. Vejby-Christensen, and D. Zajfman. Production of Water Molecules from Dissociative Recombination of H_3O^+ with Electrons. *Phys. Rev. Lett.*, 77:4891–4894, 1996.

[3] V.G. Anicich and W.T. Huntress. A survey of bimolecular ion-molecule reactions for use in modeling the chemistry of planetary atmospheres, cometary comae, and interstellar clouds. *Ap. J. Suppl. Ser.*, 62:553–672, November 1986.

[4] C.F. Barnett. Atomic Data for Fusion. Volume 1: Collisions of H, H_2, He and Li atoms and ions with atoms and molecules. Technical Report ORNL-6086/V1, Oak Ridge National Laboratory, 1990. URL: http://www-cfadc.phy.ornl.gov/redbooks/one/1.html.

[5] D.R. Bates. Super dissociative recombination. *J. Phys. B*, 24:703–709, 1991.

[6] L. Belau, K.R. Wilson, S.R. Leone, and M. Ahmed. Vacuum Ultraviolet (VUV) Photoionization of Small Water Clusters. *J. Phys. Chem. A*, 111:10075–10083, 2007.

[7] H.S. Bridge, J.W. Belcher, A.J. Lazarus, S. Olbert, J.D. Sullivan, F. Bagenal, P.R. Gazis, R.E. Hartle, K.W. Ogilvie, J.D. Scudder, E.C. Sittler, A. Eviatar, G.L. Siscoe, C.K. Goertz, and V.M. Vasyliunas. Plasma Observations Near Saturn: Initial Results from Voyager 1. *Science*, 212:217–224, 1981.

[8] A.L. Broadfoot, B.R. Sandel, D.E. Shemansky, S.K. Atreya, T.M. Donahue, H.W. Moos, J.L. Bertaux, J.E. Blamont, J.M. Ajello, D.F. Strobel, J.C. McConnel, A. Dalgarno, R. Goody, M.B. McElroy, and Y.L. Yung. Ultraviolet Spectrometer Experiment for the Voyager Mission. *Space Sci. Rev.*, 21:183–205, 1977.

[9] A.L. Broadfoot, B.R. Sandel, D.E. Shemansky, J.B. Holberg, G.R. Smith, D.F. Strobel, J.C. McConnell, S. Kumar, D.M. Hunten, S.K. Atreya, T.M. Donahue, H.W. Moos, J.L. Bertaux, J.E. Blamont, R.B. Pomphrey, and S. Linick. Extreme Ultraviolet Observations from Voyager 1 Encounter with Saturn. *Science*, 212:206–211, 1981.

[10] E. Brook, M.F.A. Harrison, and A.C.H. Smith. Measurements of the electron impact ionisation cross sections of He, C, O, and N atoms. *J. Phys. B*, 11:3115–3132, 1978.

[11] R.H. Brown, K.H. Baines, G. Bellucci, J.P. Bibring, B.J. Buratti, F. Capaccioni, P. Cerroni, R.N. Clark, A. Coradini, D.P. Cruikshank, P. Drossart, V. Formisano, R. Jaumann, Y. Langevin, D.L. Matson, T.B. McCord, V. Mennella, E. Miller, R.M. Nelson, P.D. Nicholson, B. Sicardy, and C. Sotin. The Cassini Visual And Infrared Mapping Spectrometer (VIMS) Investigation. *Space Sci. Rev.*, 115:111–168, December 2004. See also VIMS website, http://wwwvims.lpl.arizona.edu.

[12] F. Capaccioni, A. Coradini, P. Cerroni, and S. Amici. Imaging spectroscopy of Saturn and its sattelites: VIMS-V onboard Cassini. *Planet. Space Sci.*, 46:1263–1276, 1998.

[13] T.A. Cassidy and R.E. Johnson. Collisional spreading of Enceladus' neutral cloud. *Icarus*, 2010.

[14] S. Chung, C.C. Lin, and E.T.P. Lee. Dissociation of the hydrogen molecule by electron impact. *Phys. Rev. A*, 12:1340–1349, 1975.

[15] A.J. Coates, H.J. McAndrews, A.M. Rymer, D.T. Young, F.J. Crary, S. Maurice, R.E. Johnson, R.A. Baragiola, R.L. Tokar, E.C. Sittler, and G.R. Lewis. Plasma electrons above Saturn's main rings: CAPS observations. *Geophys. Res. Lett.*, 32:L14S09, June 2005.

[16] A. Dalgarno. Low Energy Stopping Power of Atomic Hydrogen. *Proc. Phys. Soc.*, 75:374–377, 1960.

[17] I. de Pater and J.J. Lissauer. *Planetary Sciences*. Cambridge University Press, Cambridge, 2001.

[18] L.B. d'Hendecourt, L.J. Allamandola, and J.M. Greenberg. Time dependent chemistry in dense molecular clouds. I. Grain surface reactions, gas/grain interactions and infrared spectroscopy. *Astron. Astrophys.*, 152:130–150, 1985.

[19] L.W. Esposito, C.A. Barth, J.E. Colwell, G.M. Lawrence, W.E. McClintock, A.I.F. Stewart, H.U. Keller, A. Korth, H. Lauche, M.C. Festou, A.L. Lane, C.J. Hansen, J.N. Maki, R.A. West, H. Jahn, R. Reulke, K. Warlich, D.E. Shemansky, and Y.L. Yung. The Cassini Ultraviolet Imaging Spectrograph Investigation. *Space Sci. Rev.*, 115:299–361, December 2004. See also UVIS website, http://lasp.colorado.edu/cassini/.

[20] L.W. Esposito, J.E. Colwell, K. Larsen, W.E. McClintock, A.I.F. Stewart, J.T. Hallett, D.E. Shemansky, J.M. Ajello, C.J. Hansen, A.R. Hendrix, R.A. West, H.U. Keller, A. Korth, W.R. Pryor, R. Reulke, and Y.L. Yung. Ultraviolet Imaging Spectroscopy Shows an Active Saturnian System. *Science*, 307:1251–1255, 2005.

[21] L.W. Esposito, J.E. Colwell, and W.E. McClintock. Cassini UVIS observations of Saturn's rings. *Planet. Space Sci.*, 46:1221–1235, 1998.

[22] L.W. Esposito, J.N. Cuzzi, J.B. Holberg, E.A. Marouf, G.L. Tyler, and C.C. Porco. Saturn's rings: structure, dynamics, and particle properties. In T. Gehrels and M.S. Matthews, editors, *Saturn*, Space science series, pages 463–545. University of Arizona, Tucson, 1984.

[23] B.L. Fleshman, P.A. delamere, and F. Bagenal. A sensitivity study of the Enceladus torus. *J. Geophys. Res.*, 115:E04007, 2010.

[24] B.L. Fleshman, P.A. Delamere, and F. Bagenal. Modeling the Enceladus plume-plasma interaction. *Geophys. Res. Lett.*, 37:L03202, 2010.

[25] L.A. Frank, B.G. Burek, K.L. Ackerson, J.H. Wolfe, and J.D. Mihalov. Plasmas in Saturn's magnetosphere. *J. Geophys. Res.*, 85:5695–5708, November 1980.

[26] T.I. Gombosi, T.P. Armstrong, C.S. Arridge, K.K. Khurana, S.M Krimigis, N. Krupp, A.M. Persoon, and M.F. Thomsen. Saturn's Magnetospheric Configuration. In M.K. Dougherty, L.W. Esposito, and S.M. Krimigis, editors, *Saturn from Cassini-Huygens*, pages 203–256. Springer, Dordrecht, 2009.

[27] J.B. Greenwood, A. Chutjian, and S.J. Smith. Measurements of Absolute, Single Charge-Exchange Cross Sections of H^+, HE^+ and HE^{2+} with H_2O and CO_2. *Ap. J.*, 529:605–609, January 2000.

[28] E. Grün, H.A. Zook, H. Fechtig, and R.H. Giese. Collisional Balance of the Meteoritic Complex. *Icarus*, 62:244–272, 1985.

[29] J.T. Hallett, D.E. Shemansky, and X. Liu. A Rotational-Level Hydrogen Physical Chemistry Model for General Astrophysical Application. *Ap. J.*, 624:448–461, 2005.

[30] J.T. Hallett, D.E. Shemansky, and X. Liu. Fine-Structure Physical Chemistry Modeling of Uranus H_2 X Quadrupole Emission. *Geophys. Res. Lett.*, 32:L02204, 2005.

[31] C.J. Hansen, L. Esposito, A.I.F. Stewart, J. Colwell, A. Hendrix, W. Pryor, D. Shemansky, and R. West. Enceladus' Water Vapor Plume. *Science*, 311:1422–1425, 2006.

[32] C.J. Hansen, L.W. Esposito, A.I.F. Stewart, B. Meinke, B. Wallis, J.E. Colwell, A.R. Hendrix, K. Larsen, W. Pryor, and F. Tian. Water vapour jets inside the plume of gas leaving Enceladus. *Nature*, 456:477–479, 2008.

[33] C.J. Hansen, D.E. Shemansky, L.W. Esposito, A.I.F. Stewart, B.R. Lewis, J.E. Colwell, A.R. Hendrix, R.A. West, J.H. Waite, B. Teolis, and B.A. Magee. The composition and structure of the Enceladus plume. *Geophys. Res. Lett.*, 36:L11202, 2011.

[34] T. Harb, W. Kedzierski, and J.W. McConkey. Production of ground state OH following electron impact on H2O. *J. Chem. Phys.*, 115:5507–5512, September 2001.

[35] P. Hartogh, E. Lellouch, R. Moreno, D. Bockelée-Morvan, N. Biver, T. Cassidy, M. Rengel, C. Jarchow, T. Cavalié, J. Crovisier, F.P. Helmich, and M. Kidger. Direct detection of the Enceladus water torus with *Herschel*. *Astron. Astrophys.*, 2011. In press.

[36] W.F. Huebner, J.J. Keady, and S.P. Lyon. Solar photo rates for planetary atmospheres and atmospheric pollutants. *Ap. Space Sci.*, 195:1–294, 1992.

[37] W.T. Huntress. Laboratory studies of bimolecular reactions of positive ions in interstellar clouds, in comets, and in planetary atmospheres of reducing composition. *Ap. J. Suppl. Ser.*, 33:495–514, 1977.

[38] A. Ichihara, O. Iwamoto, and R.K. Janev. Cross sections for the reaction $H^+ + H_2$ (v = 0-14) $\rightarrow H + H_2^+$ at low collision energies. *Journal of Physics B Atomic Molecular Physics*, 33:4747–4758, November 2000.

[39] W.-H. Ip. On the Neutral Cloud Distribution in the Saturnian Magnetosphere. *Icarus*, 126:42–57, 1997.

[40] Y. Itikawa. Cross Sections for Electron Collisions with Water Molecules. *Journal of Physical and Chemical Reference Data*, 34:1–22, 2005.

[41] Y. Itikawa, A. Ichimura, K. Onda, K. Sakimoto, K. Takayanagi, Y. Hatano, M. Hayashi, H. Nishimura, and S. Tsurubuchi. Cross Sections for Collisions of Electrons and Photons with Oxygen Molecules. *J. Phys. Chem. Ref. Data*, 18:23–42, 1989.

[42] M.J. Jensen, R.C. Bilodeau, O. Heber, H.B. Pedersen, C.P. Safvan, X. Urbain, D. Zijfman, and L.H. Anderson. Dissociative recombination and excitation of H_2O^+ and HDO^+. *Phys. Rev. A*, 60:2970–2977, 1999.

[43] R. Johnsen. Electron-temperature dependence of the recombination of $H_3O^+(H_2O)_n$ ions with electrons. *J. Chem. Phys.*, 98:5390–5395, 1993.

[44] R.E. Johnson. Sputtering and desorption from icy surfaces. In B. Schmitt, C. de Bergh, and M. Festou, editors, *Solar System Ices*, Astrophysics and Space Science Library, pages 303–334. Kluser Academic Publishers, Netherlands, 1998.

[45] R.E. Johnson, J.G. Luhmann, R.L. Tokar, M. Bouhram, J.J. Berthelier, E.C. Sittler, J.F. Cooper, T.W. Hill, H.T. Smith, M. Micahel, M. Liu, F.J. Crary, and D.T. Young. Production, ionization and redistribution of O_2 in Saturn's ring atmosphere. *Icarus*, 180:393–402, 2006.

[46] G.H. Jones, C.S. Arridge, A.J. Coates, G.R. Lewis, S. Kanani, A. Wellbrock, D.T. Young, F.J. Crary, R.L. Tokar, R.J. Wilson, T.W. Hill, R.E. Johnson, D.G. Mitchell, J. Schmidt, S. Kempf, U. Beckmann, C.T. Russell, Y.D. Jia, M.K. Dougherty, J.H. Waite, and B.A. Magee. Fine jet structure of electrically charged grains in Enceladus' plume. *Geophys. Res. Lett.*, 36:L16204, 2009.

[47] A. Juhász and M. Horányi. Saturn's E ring: A dynamical approach. *J. Geophys. Res.*, 107(A6):doi:10.1029/2001JA000182, 2002.

[48] S. Jurac, R.E. Johnson, and B. Donn. Monte Carlo calculations of the sputtering of grains: enhanced sputtering of small grains. *Ap. J.*, 503:247–252, 1998.

[49] S. Jurac, R.E. Johnson, and J.D. Richardson. Saturn's E Ring and Production of the Neutral Torus. *Icarus*, 149:384–396, 2001.

[50] S. Jurac, R.E. Johnson, J.D. Richardson, and C. Paranicas. Satellite Sputtering in Saturn's Magnetosphere. *Planet. Space Sci.*, 49:319–326, 2001.

[51] S. Kempf, U. Beckmann, G. Moragas-Klostermeyer, F. Postberg, R. Srama, T. Economou, J. Schmidt, F. Spahn, and E. Grün. The E ring in the vicinity of Enceladus. I. Spatial distribution and properties of the ring particles. *Icarus*, 193:420–437, 2008.

[52] S.W. Kieffer, X. Lu, G. McFarquhar, and K.H. Wohletz. A redetermination of the ice/vapor ratio of Enceladus' plumes: Implications for sublimation and the lack of a liquid water reservoir. *Icarus*, 203:238–241, 2009.

[53] R. Killen, D.E. Shemansky, and N. Mouawad. Expected Emission from Mercury's Exospheric Species, and their Ultraviolet-Visible Signatures. *Ap. J. Suppl. Ser.*, 181:351–359, April 2009.

[54] S.J. King and S.D. Price. Electron ionization of H_2O. *International Journal of Mass Spectrometry*, 277:84–90, November 2008.

[55] H. Knof, E.A. Mason, and J.T. Vanderslice. Interaction Energies, Charge Exchange Cross Sections, and Diffusion Cross Sections For N^+-N and O^+-O Collisions. *J. Chem. Phys.*, 40:3548–3553, June 1964.

[56] S.M. Krimigis, T.P. Armstrong, W.I. Axford, C.O. Bostrom, G. Gloeckler, E.P. Keath, L.J. Lanzerotti, J.F. Carbary, D.C. Hamilton, and E.C. Roelof. Low-Energy Charged Particles in Saturn's Magnetosphere: Results from Voyager I. *Science*, 212:225–231, 1981.

[57] S.M. Krimigis, D.G. Mitchell, D.C. Hamilton, S. Livi, J. Dandouras, S. Jaskulek, T.P. Armstrong, J.D. Boldt, A.F. Cheng, G. Gloeckler, J.R. Hayes, K.C. Hsieh, W.-H. Ip, E.P. Keath, E. Kirsch, N. Krupp, L.J. Lanzerotti, R. Lundgren, B.H. Mauk, R.W. McEntire, E.C. Roelof, C.E. Schlemm, B.E. Tossman, B. Wilken, and D.J. Williams. Magnetosphere Imaging Instrument (MIMI) on the Cassini Mission to Saturn/Titan. *Space Sci. Rev.*, 114:233–329, September 2004. See also MIMI webpage: http://sd-www.jhuapl.edu/CASSINI/index.html.

[58] G.M. Lancaster, F. Honda, Y. Fukuda, and J.W. Rabalais. Secondary Ion Mass Spectrometry of Molecular Solids. Cluster Formation during Ion Bombardment of Frozen Water, Benzene, and Cyclohexane. *J. Am. Chem. Soc.*, 101:1951–1958, 1979.

[59] X. Li, Y.-L. Huang, G.D. Flesch, and C.Y. Ng. A state-selected study of the ion-molecule reactions $O^+(^2D, ^2P) + H_2O$. *J. Chem. Phys.*, 106:928–933, 1997.

[60] B.G. Lindsay and M.A. Mangan. 5.1 Ionization. In Y. Itikawa, editor, *Photon and Electron Interactions with Atoms, Molecules and Ions*, Landolt-Börnstein, vol. I/17, subvolume C. Springer, New York, 2003.

[61] B.G. Lindsay, D.R. Sieglaff, K.A. Smith, and R.F. Stebbings. Charge transfer of 0.5-, 1.5-, and 5-keV protons with H_2O:mAbsolute differential and integral cross sections. *Phys. Rev. A*, 55:3945–3946, May 1997.

[62] B.G. Lindsay and R.F. Stebbings. Charge transfer cross sections for energetic neutral atom data analysis. *J. Geophys. Res.*, 110(A9):A12213, December 2005.

[63] C.R. Lishawa, R.A. Dressler, J.A. Gardner, R.H. Salter, and E. Murad. Cross sections and product kinetic energy analysis of H_2O^+-H_2O collisions at suprathermal energies. *J. Chem. Phys.*, 93:3196–3206, 1990.

[64] X. Liu and D.E. Shemansky. Ionization of Molecular Hydrogen. *Ap. J.*, 614:1132–1142, October 2004.

[65] J.W. McConkey, C.P. Malone, P.V. Johnson, C. Winstead, V. McKoy, and I. Kanik. Electron impact dissociation of oxygen-containing molecules A critical review. *Phys. Rep.*, 466:1–103, September 2008.

[66] J.W. McGowan, P.M. Mul, V.S. D'Angelo, J.B.A. Mitchell, P. Defrance, and H.R. Froelich. Energy Dependence of Dissociative Recombination below 0.08 eV Measured with (Electron-Ion) Merged-Beam Technique. *Phys. Rev. Lett.*, 42:373–375, 1979.

[67] H. Melin, D.E. Shemansky, and X. Liu. The distribution of atomic hydrogen and oxygen in the magnetosphere of Saturn. *Planet. Space Sci.*, 57:1743–1753, December 2009.

[68] D.H. Mordaunt, M.N.R. Ashfold, and R.N. Dixon. Dissociation dynamics of $H_2O(D_2O)$ following photoexcitation at the Lyman-α wavelength (121.6 nm). *J. Chem. Phys.*, 100:7360–7375, May 1994.

[69] D. Morrison, T.V. Johnson, E.M. Shoemaker, L.A. Soderbloom, P. Thomas, J. Veverka, and B.A. Smith. Satellites of Saturn. In T. Gehrels and M.S. Matthews, editors, *Saturn*, Space science series, pages 609–663. University of Arizona Press, Tucson, 1984.

[70] P.M. Mul and J.W. McGowan. Merged electron-ion beam experiments III. Temperature dependence of dissociative recombination for atmospheric ions NO^+, O_2^+ and N_2^+. *J. Phys. B*, 12:1591–1601, 1979.

[71] U. Müller, T. Bubel, and G. Schulz. Electron impact dissociation of H_2O: emission cross sections for OH^*, OH^{+*}, H^*, and H_2O^{+*} fragments. *Zeitschrift fur Physik D Atoms Molecules Clusters*, 25:167–174, June 1993.

[72] M.B. Någård, J.B.C. Pettersson, A.M. Derkatch, A. Al Khalili, A. Neau, S. Rosén, M. Larsson, J. Semaniak, H. Danared, A. Källberg, F. Österdahl, and M. af Ugglas. Dissociative recombination of $D^+(D_2O)_2$ water cluster ions with free electrons. *J. Chem. Phys.*, 117:5264–5270, 2002.

[73] A. Neau, A. Al Khalili, S. Rosén, A. Le Padellec, A.M. Derkatch, W. Shi, L. Vikor, M. Larsson, J. Semaniak, R. Thomas, M.B. Någård, K. Andersson, H. Danared, and M. Af Ugglas. Dissociative recombination of $D3O^+$ and $H3O^+$: Absolute cross sections and branching ratios. *J. Chem. Phys.*, 113:1762–1770, August 2000.

[74] T.M. Orlando and M.T. Sieger. The role of electron-stimulated production of O_2 from water ice in the radiation processing of outer solar system surfaces. *Surf. Sci.*, 528:1–7, 2003.

[75] R.A. Phaneuf, R.K. Janev, and M.W. Pindzola. Atomic data for fusion. Volume V: Collisions of carbon and oxygen ions with electrons, H, H_2 and He. Technical Report ORNL-6090/V5, Oak Ridge National Laboratory, 1987.

[76] C.C. Porco, P. Helfenstein, P.C. Thomas, A.P. Ingersoll, J. Wisdom, R. West, G. Neukum, T. Denk, R. Wagner, T. Roatsch, S. Kieffer, E. Turtle, A. McEwen, T.V. Johnson, J. Rathbun, J. Veverka, D. Wilson, J. Perry, J. Spitale, A. Brahic, J.A. Burns, A.D. Del Genio, L. Dones, C.D. Murray, and S. Squyres. Cassini Observes the Active South Pole of Enceladus. *Science*, 311:1393–1401, March 2006.

[77] F. Postberg, S. Kempf, J. Schmidt, N. Brilliantov, A. Beinsen, B. Abel, U. Buck, and R. Srama. Sodium salts in E-ring ice grains from an ocean below the surface of Enceladus. *Nature*, 459:1098–1101, 2009.

[78] F. Postberg, J. Schmidt, J. Hillier, S. Kempf, and R. Srama. A salt-water reservoir as the source of a compositionally stratified plume on enceladus. *Nature*, 473:620–622, 2011.

[79] J.D. Richardson, A. Eviatar, and G.L. Siscoe. Satellite Tori at Saturn. *J. Geophys. Res.*, 91:8749–9755, 1986.

[80] A.M. Rymer, B.H. Mauk, T.W. Hill, C. Paranicas, N. André, E.C. Sittler, D.G. Mitchell, H.T. Smith, R.E. Johnson, A.J. Coates, D.T. Young, S.J. Bolton, M.F. Thomsen, and M.K. Dougherty. Electron sources in Saturn's magnetosphere. *J. Geophys. Res.*, 112(A11):A02201, February 2007.

[81] B.R. Sandel, D.E. Shemansky, A.L. Broadfoot, J.B. Holberg, G.R. Smith, J.C. McConnell, D.F. Strobel, S.K. Atreya, T.M. Donahue, H.W. Moos, D.M. Hunten, R.B. Pomphrey, and S. Linick. Extreme Ultraviolet Observations from the Voyager 2 Encounter with Saturn. *Science*, 215:548–553, 1982.

[82] P. Schippers, M. Blanc, N. André, I. Dandouras, G.R. Lewis, L.K. Gilbert, A.M. Persoon, N. Krupp, D.A. Gurnett, A.J. Coates, S.M. Krimigis, D.T. Young, and M.K. Dougherty. Multi-instrument analysis of electron populations in Saturn's magnetosphere. *J. Geophys. Res.*, 113(A12):A07208, July 2008.

[83] M.B. Shah, D.S. Elliott, and H.B. Gilbody. Pulsed crossed-beam study of the ionization of atomic-hydrogen by electron-impact. *J. Phys. B*, 20:3501–3514, 1987.

[84] D.E. Shemansky. Unpublished research notebooks.

[85] D.E. Shemansky. Radiative cooling efficiencies and predicted spectra of species of the Io plasma torus. *Ap. J.*, 236:1043–1054, 1980.

[86] D.E. Shemansky. Energy Branching in the Io Plasma Torus: The Failure of Neutral Cloud Theory. *J. Geophys. Res.*, 93:1773–1784, 1988.

[87] D.E. Shemansky. Neutral species in the Saturn magnetosphere. Unpublished, 1997.

[88] D.E. Shemansky. Atomic oxygen in the Saturn magnetosphere. Unpublished, 2005.

[89] D.E. Shemansky. Private communication. 2008.

[90] D.E. Shemansky. Reaction Rate Equations. Unpublished, 2009.

[91] D.E. Shemansky. Private communication. 2010.

[92] D.E. Shemansky. Private communication. 2011.

[93] D.E. Shemansky and D.T. Hall. The Distribution of Atomic Hydrogen in the Magnetosphere of Saturn. *J. Geophys. Res.*, 97:4143–4161, 1992.

[94] D.E. Shemansky, X. Liu, and H. Melin. The Saturn hydrogen plume. *Planet. Space Sci.*, 57:1659–1670, December 2009.

[95] D.E. Shemansky, P. Matheson, D.T. Hall, H.-Y. Hu, and T.M. Tripp. Detection of the hydroxyl radical in the Saturn magnetosphere. *Nature*, 3636:329–331, 1993.

[96] M. Shi, R.A. Baragiola, D.E. Grosjean, R.E. Johnson, S. Jurac, and J. Schou. Sputtering of water ice surfaces and the production of extended neutral atmospheres. *J. Geophys. Res.*, 100:26387–26395, 1995.

[97] E.C. Sittler, N. Andre, M. Blanc, M. Burger, R.E. Johnson, A. Coates, A. Rymer, D. Reisenfeld, M.F. Thomsen, A. Persoon, M. Dougherty, H.T. Smith, R.A. Baragiola, R.E. Hartle, D. Chornay, M.D. Shappirio, D. Simpson, D.J. McComas, and D.T. Young. Ion and neutral sources and sinks within Saturn's *inner* magnetosphere: Cassini results. *Planet. Space Sci.*, 56:3–18, 2008.

[98] E.C. Sittler, J.D. Scudder, and H.S. Bridge. Distribution of neutral gas and dust near Saturn. *Nature*, 292:711–714, 1981.

[99] E.C. Sittler, M. Thomsen, D. Chornay, M.D. Shappirio, D. Simpson, R.E. Johnson, H.T. Smith, A.J. Coates, A.M. Rymer, F. Crary, D.J. McComas, D.T. Young, D. Reisenfeld, M. Dougherty, and N. Andre. Preliminary results on Saturn's inner plasmasphere as observed by Cassini: Comparison with Voyager. *Geophys. Res. Lett.*, 32:L14S07, jun 2005.

[100] H.T. Smith, R.E. Johnson, E. C. Sittler, M. Shappirio, D. Reisenfeld, O.J. Tucker, M. Burger, F.J. Crary, D.J. McComas, and D.T. Young. Enceladus: The likely dominant nitrogen source in Saturn's magnetosphere. *Icarus*, 188:356–366, 2007.

[101] H.T. Smith, M. Shappirio, E.C. Sittler, D. Reisenfeld, R.E. Johnson, R.A. Baragiola, F.J. Crary, D.J. McComas, and D.T. Young. Discovery of nitrogen in Saturn's inner magnetosphere. *Geophys. Res. Lett.*, 32:L14S03, 2005.

[102] F. Spahn, J. Schmidt, N. Albers, M. Hörning, M. Makuch, M. Seiß, S. Kempf, R. Srama, V. Dikarev, S. Helfert, G. Moragas-Klostermeyer, A.V. Krivov, M. Sremčević, A.J. Tuzzolino, T. Economou, and E. Grün. Cassini Dust Measurements at Enceladus and Implications for the Origin of the E Ring. *Science*, 311:1416–1418, March 2006.

[103] J.A. Spirko, J.J. Zirbel, and A.P. Hickman. Quantum mechanical scattering calculations for charge exchange: $O + H^+ \leftrightarrow O^+ + H$. *J. Phys. B*, 36:1645–1662, 2003.

[104] L. Spitzer. *Physics of Fully Ionized Gases.* Dover Publications, 1962. Unabridged republication of 1962 second revised edition originally published by John Wiley & Sons.

[105] S.K. Srivastava. Private communication. 1991.

[106] C. Strömholm, H. Danared, Å. Larson, M. Larsson, C. Marian, S. Rosén, B. Schimmelpfennig, I.F. Schneider, J. Semaniak, A. Suzor-Weiner, U. Wahlgren, and W.J. van der Zande. Imaging spectroscopy of recombination fragments of OH^+. *Journal of Physics B Atomic Molecular Physics*, 30:4919–4933, November 1997.

[107] J.T. Su, X. Xu, and W.A. Goddard. Accurate Energies and Structures for Large Water Clusters Using the X3LYP Hybrid Density Functional. *J. Phys. Chem.*, 108:10518–10526, 2004.

[108] P. Thorn, L. Campbell, and M. Brunger. Electron excitation and energy transfer rates for H2O in the upper atmosphere. *PMC Physics B*, 2:1, 2009.

[109] B.R. Turner and J.A. Rutherford. Charge Transfer and Ion-Atom Interchange Reactions of Water Vapor Ions. *J. Geophys. Res.*, 73:6751–6758, 1968.

[110] R. van Harrevelt and M.C. van Hemert. Photodissociation of water in the $\tilde{A}$ band revisited with new potential energy surfaces. *J. Chem. Phys.*, 114:9453–, 2001.

[111] J.H. Waite, M.R. Combi, W.-H. Ip, T.E. Cravens, R.L. McNutt, W. Kasprzak, R. Yelle, J. Luhmann, H. Niemann, D. Gell, B. Magee, G. Fletcher, J. Lunine, and W.-L. Tseng. Cassini Ion and Neutral Mass Spectrometer: Enceladus Plume Composition and Structure. *Science*, 311:1419–1422, March 2006.

[112] J.H. Waite, W.S. Lewis, W.T. Kasprzak, V.G. Anicich, B.P. Block, T.E. Cravens, G.G. Fletcher, W.-H. Ip, J.G. Luhmann, R.L. McNutt, H.B. Niemann, J.K. Parejko, J.E. Richards, R.L. Thorpe, E.M. Walter, and R.V. Yelle. The Cassini Ion and Neutral Mass Spectrometer (INMS) Investigation. *Space Sci. Rev.*, 114:113–231, September 2004. See also INMS webpage: http://inms.gsfc.nasa.gov/.

[113] J.H. Waite, W.S. Lewis, B.A. Magee, J.I. Lunine, W.B. McKinnon, C.R. Glein, O. Mousis, D.T. Young, T. Brockwell, J. Westlake, M.-J. Nguyen, B.D. Teolis, H.B. Niemann, R.L. McNutt, M. Perry, and W.-H. Ip. Liquid water on Enceladus from observations of ammonia and ^{40}Ar in the plume. *Nature*, 460:487–490, 2009.

[114] J. Woodall, M. Agúndez, A.J. Markwick-Kemper, and T.J. Millar. The UMIST database for astrochemistry 2006. *Astron. Astrophys.*, 466:1197–1204, May 2007.

[115] J.M. Yoshii, D.E. Shemansky, and X. Liu. Saturn magnetosphere paper. In preparation, 2011.

[116] D.T. Young, J.-J. Berthelier, M. Blanc, J.L. Burch, S. Bolton, A.J. Coates, F.J. Crary, R. Goldstein, M. Grande, T.W. Hill, R.E. Johnson, R.A. Baragiola, V. Kelha, D.J. mcComas, K. Mursula, E.C. Sittler, K.R. Svenes, K. Szegö, P. Tanskanen, M.F. Thomsen, S. Bakshi, B.L. Barraclough, Z. Bebesi, D. Delapp, M.W. Dunlop, J.T. Gosling, J.D. Furman, L.K. Gilbert, D. Glenn, C. Holmlund, J.-M. Illiano, G.R. Lewis, D.R. Linder, S. Maurice, H.J. McAndrews, B.T. Narheim, E. Pallier, D. Reisenfeld, A.M. Rymer, H.T. Smith, R.L. Tokar, J. Vilppola, and C. Zinsmeyer. Composition and Dynamics of Plasma in Saturn's Magnetosphere. *Science*, 307:1262–1266, 2005.

[117] D.T. Young, J.J. Berthelier, M. Blanc, J.L. Burch, A.J. Coates, R. Goldstein, M. Grande, T.W. Hill, R.E. Johnson, V. Kelha, D.J. McComas, E.C. Sittler, K.R. Svenes, K. Szegö, P. Tanskanen, K. Ahola, D. Anderson, S. Bakshi, R.A. Baragiola, B.L. Barraclough, R.K. Black, S. Bolton, T. Booker, R. Bowman, P. Casey, F.J. Crary, D. Delapp, G. Dirks, N. Eaker, H. Funsten, J.D. Furman, J.T. Gosling, H. Hannula, C. Holmlund, H. Huomo, J.M. Illiano, P. Jensen, M.A. Johnson, D.R. Linder, T. Luntama, S. Maurice, K.P. McCabe, K. Mursula, B.T. Narheim, J.E. Nordholt, A. Preece, J. Rudzki, A. Ruitberg, K. Smith, S. Szalai, M.F. Thomsen, K. Viherkanto, J. Vilppola, T. Vollmer, T.E. Wahl, M. Wüest, T. Ylikorpi, and C. Zinsmeyer. Cassini Plasma Spectrometer Investigation. *Space Sci. Rev.*, 114:1–112, September 2004. See also CAPS webpage: http://caps.space.swri.edu.

[118] Y.L. Yung and M.B. McElroy. Stability of an Oxygen Atmosphere on Ganymede. *Icarus*, 30:97–103, 1977.

Appendix A

Further details on collision strengths and rate coefficients

The chemical reactions in the Saturn magnetosphere system generally have one reactant, the impactor, which carries most of the energy in the interaction, while the other reactant, the target, moves at a much lower velocity than the impactor and can be considered to be stationary. The rate equations as described in [90] assume electrons as impactors. To adapt the equations for use with heavy impactors (i.e., ions or neutrals) a mass scaling factor must be introduced. For an impactor population of $N(v)$ with temperature T and effective mass M, and a target population N_x is

$$R = \left(\frac{m_e}{M}\right)^{\frac{1}{2}} N_x \int_0^{\infty} v \cdot N(v) \cdot \sigma(v) \cdot dv \tag{A.1}$$

where v is the relative velocity between the target and impactor particles, $\sigma(v)$ is the cross section (in cm^2) for the reaction, and m_e is the electron mass. The cross section and the nondimensional collision strength are related[90] by

$$\sigma(v) = \frac{\pi \hbar^2}{m^2 v^2}\ \Omega(v) \tag{A.2}$$

The generalized rate theory describes the system in terms of an initial state i and a transition to a final state j. The terminology readily applies to processes such as electron impact excitation, where i describes the initial, lower energy state of an atom or molecule and the excitation causes a transition to the final, higher energy state. For the Saturn magnetosphere chemistry considered in this work, the "transition" is a reaction, the initial state consists of the reactants, and the final state is the products. The collision strength $\Omega_{ij}(v)$ is a measure of the probability that a given pair of reactants undergoes the reaction described by i and j.

E_{ij}, the threshold energy for the transition from state i to state j, can be used to rewrite the rate equation using the relative energy of the reactants, $E = \frac{1}{2}mv^2$ (monoenergetic impactor) or $E = kT$ (thermal impactor), in terms of the nondimensional energies $X = \frac{E}{E_{ij}}$ for monoenergetic impactors and $Y = \frac{E_{ij}}{kT}$ for thermal impactors. The degeneracy ω_i must be factored in, so that $\frac{\Omega_{ij}(E)}{\omega_i}$ replaces $\Omega(v)$.

The thermally averaged collision strength, $\Omega_{ij}(Y)$, is defined by

$$\int_0^\infty \frac{\Omega_{ij}(X)}{\omega_i} \cdot e^{-XY} dX = \frac{\Omega_{ij}(Y)}{\omega_i} \int_0^\infty e^{-XY} dX = \frac{\Omega_{ij}(Y)}{\omega_i} \cdot \frac{1}{Y} \tag{A.3}$$

for exothermic reactions or by

$$\int_0^\infty \frac{\Omega_{ij}(X)}{\omega_i} \cdot e^{-XY} dX = \frac{\Omega_{ij}(Y)}{\omega_i} \int_0^\infty e^{-XY} dX = \frac{\Omega_{ij}(Y)}{\omega_i} \cdot \frac{1}{Ye^Y} \tag{A.4}$$

for endothermic reactions, which must satisfy $E \geq E_{ij}$ in order to take place. The rate coefficient k_{ij} relates to the rate by

$$R_{ij} = N \cdot N_x \cdot k_{ij} \tag{A.5}$$

The impactors may be modelled either as Maxwellian particles, represented by a temperature T, or as a monoenergetic population represented by a single energy. If the impactors are monoenergetic,

$$N(v) = N\delta(v) \tag{A.6}$$

and the rate coefficient reduces to

$$k_{ij}(X) = \frac{\pi\hbar^2}{\sqrt{2}\ m^{\frac{3}{2}}} \frac{1}{E^{\frac{1}{2}}} \frac{\Omega_{ij}(X)}{\omega_i} \tag{A.7}$$

In this work, the ions in ion-neutral reactions are monoenergetic impactors.

On the other hand, for thermally distributed impactors,

$$\frac{N(v)}{N} dv = 4\pi \left(\frac{m}{2\pi kT}\right)^{\frac{3}{2}} v^2 e^{-\frac{mv^2}{kT}} dv \tag{A.8}$$

and the rate coefficient reduces to, in its most basic forms,

$$k_{ij}(Y) = \frac{h^2}{(2\pi m)^{\frac{3}{2}}} \left(\frac{Y}{E_{ij}}\right)^{\frac{1}{2}} \frac{\Omega_{ij}(Y)}{\omega_i} \tag{A.9}$$

for exothermic reactions or

$$k_{ij}(Y) = \frac{h^2}{(2\pi m)^{\frac{3}{2}}} \left(\frac{Y}{E_{ij}}\right)^{\frac{1}{2}} \frac{\Omega_{ij}(Y)}{\omega_i} e^{-Y} \tag{A.10}$$

for endothermic reactions[90]. In this work, electrons in either electron-ion or electron-neutral reactions, and neutrals in neutral-neutral reactions, are thermal impactors.

The equations for $k_{ij}(Y)$ may contain additional factors depending on the processes involved. For example, if momentum transfer is included, the integral in the definition of $\Omega_{ij}(Y)$, the integral $\int_0^\infty \frac{\Omega_{ij}(X)}{\omega_i} \cdot e^{-XY} dX$ becomes $\int_0^\infty \frac{X}{X+1} \frac{\Omega_{ij}(X)}{\omega_i} \cdot e^{-XY} dX$. Various computational simplications, such as truncating the energy range of the integration over X at a finite value, may also be made. Several different analytic formulations for $k_{ij}(Y)$ have been defined by Shemansky[90].

For photoprocesses, the volumetric excitation rate of the state j from state i in units of cm^{-3} s^{-1} is given by

$$\mathcal{G}_{ij} = \int \pi\mathcal{F}_\nu \cdot \frac{r_0^2}{r^2} \cdot k_\nu^{ij} d\nu \tag{A.11}$$

where $\pi\mathcal{F}_\nu$ is the differential solar flux at 1 AU (in units of photons cm^{-2} s^{-1} (cm^{-1})$^{-1}$), $r_0 = 1$ AU, $r =$ distance of the gas volume from the Sun in AU, k_ν^{ij} is the absorption coefficient for the process (which, despite the name, can be any photoprocess such as photoionization or photodissociation) in cm^{-1}, and ν is the wavenumber (in cm^{-1})[53]. In terms of the population of the target state i, $[N_i]$, Eq. A.11 can be written as

$$\mathcal{G}_{ij} = [N_i] \cdot g_{ij} \tag{A.12}$$

where g_{ij} is the transition probability for the photoprocess. Transition probabilities are tabulated in e.g. Huebner et al. [36].

Appendix B

Chemical rate equations

Rate equations for the system of chemical reactions at 4 R_s, as currently represented by the water architecture file h2og.mdf and solved by the chemistry code coreqg.f90, are listed below. The quantities in square brackets are populations, and the subscripts of the rate coefficients k and photoprocess transition probabilities g are the numbers of the reactions as they appear in Table 2.1. D_O and D_{OH} are the diffusion coefficients for O and OH, respectively. The total loss rates Q and production rates R are the ones which appear in Equation 2.8.

In reactions where neutral products are able to escape, the number of heavy particles is conserved by diffusing in the appropriate fraction of water molecules to replace the lost products, i.e. $\frac{1}{3}$ of an H_2O molecule replaces a monatomic species while $\frac{2}{3}$ of an H_2O replaces a diatomic species.

$$
\begin{aligned}
\frac{d[H_2O]}{dt} \quad = \quad & -\{(k_1 + k_2 + k_3 + k_4 + k_5) \cdot [e] + g_6 + g_7 + g_8 \\
& + g_9 + g_{10} + g_{11} + g_{12} + k_{56} \cdot [H_2O^+] + (k_{60} + k_{61}) \cdot [OH^+] \\
& + k_{63} \cdot [H^+] + k_{70} \cdot [O^+]\} \cdot [H_2O] \\
& + \left\{ \frac{1}{3} \cdot (k_2 + k_5) \cdot [e] \cdot [H_2O] + \left(\frac{1}{3} \cdot g_6 + \frac{2}{3} \cdot g_7 + \frac{1}{3} \cdot g_{10} + \frac{2}{3} \cdot g_{11} \right) \cdot [H_2O] \right. \\
& + \left(\frac{2}{3} \cdot k_{13} + \frac{1}{3} \cdot k_{15} \right) \cdot [e] \cdot [O_2] + (2 \cdot g_{16} + 2 \cdot g_{17} + 2 \cdot g_{18} + g_{20}) \cdot [O_2] \\
& + \left(\frac{2}{3} \cdot k_{21} + \frac{1}{3} \cdot k_{22} + \frac{2}{3} \cdot k_{24} + \frac{2}{3} \cdot k_{25} + \frac{2}{3} \cdot k_{26} \right. \\
& \left. + \frac{2}{3} \cdot k_{27} + \frac{2}{3} \cdot k_{28} \right) \cdot [e] \cdot [H_2] \\
& + \left(\frac{2}{3} \cdot g_{29} + \frac{1}{3} \cdot g_{32} \right) \cdot [H_2] + (k_{34} + k_{36}) \cdot [e] \cdot [OH] \\
& + \left(\frac{1}{3} \cdot g_{37} + \frac{1}{3} \cdot g_{38} + \frac{1}{3} \cdot g_{39} \right) \cdot [OH] \\
& + \frac{2}{3} \cdot D_{OH} \cdot [OH] + \left(\frac{4}{3} \cdot k_{42} + \frac{4}{3} \cdot k_{43} + \frac{4}{3} \cdot k_{44} + \frac{4}{3} \cdot k_{45} \right) \cdot [e] \cdot [H_3O^+] \\
& + \frac{1}{3} \cdot D_O \cdot [O] + \left(k_{53} + \frac{1}{3} \cdot k_{54} + \frac{2}{3} \cdot k_{55} \right) \cdot [e] \cdot [H_2O^+] \\
& + \left(\frac{2}{3} \cdot k_{57} + \frac{1}{3} \cdot k_{58} + \frac{1}{3} \cdot k_{59} \right) \cdot [e] \cdot [OH^+] \\
& + \left(\frac{2}{3} \cdot k_{60} + \frac{1}{3} \cdot k_{61} \right) \cdot [OH^+] \cdot [H_2O] + \frac{2}{3} \cdot k_{62} \cdot [e] \cdot [H_2^+] \\
& + \frac{1}{3} \cdot k_{63} \cdot [H^+] \cdot [H_2O] + \frac{1}{3} \cdot k_{64} \cdot [H^+] \cdot [O] + \frac{1}{3} \cdot k_{65} \cdot [H^+] \cdot [O_2] \\
& + \frac{1}{3} \cdot k_{66} \cdot [H^+] \cdot [OH] + \frac{1}{3} \cdot k_{67} \cdot [H^+] \cdot [H] + \frac{1}{3} \cdot k_{68} \cdot [H^+] \cdot [H_2] \\
& + \frac{1}{3} \cdot k_{69} \cdot [O^+] \cdot [H] + \frac{1}{3} \cdot k_{70} \cdot [O^+] \cdot [H_2O] + \frac{1}{3} \cdot k_{71} \cdot [O^+] \cdot [OH] \\
& + \frac{1}{3} \cdot k_{72} \cdot [O^+] \cdot [O] + \frac{1}{3} \cdot k_{73} \cdot [O^+] \cdot [H_2] + \frac{1}{3} \cdot k_{74} \cdot [O^+] \cdot [O_2] \\
& \left. + \frac{1}{3} \cdot k_{75} \cdot [e] \cdot [O_2^+] + \frac{2}{3} \cdot k_{76} \cdot [e] \cdot [O_2^+] \right\} \\
= \quad & -Q_{H_2O} \cdot [H_2O] + R_{H_2O}
\end{aligned}
\tag{B.1}
$$

$$\begin{aligned}\frac{d[O_2]}{dt} &= -\{(k_{13}+k_{14}+k_{15})\cdot[e]+g_{16}+g_{17}+g_{18}+g_{19}+g_{20} \\ &\quad +k_{48}\cdot[H]+k_{65}\cdot[H^+]+k_{74}\cdot[O^+]\big\}\cdot[O_2] \\ &\quad +\{k_{50}\cdot[O]\cdot[OH]\} \\ &= -Q_{O_2}\cdot[O_2]+R_{O_2}\end{aligned} \tag{B.2}$$

$$\begin{aligned}\frac{d[H_2]}{dt} &= -\{(k_{21}+k_{22}+k_{23}+k_{24}+k_{25}+k_{26}+k_{27}+k_{28})\cdot[e] \\ &\quad +g_{29}+g_{30}+g_{31}+g_{32}+k_{68}\cdot[H^+]+k_{73}\cdot[O^+]\big\}\cdot[H_2] \\ &\quad +\{k_4\cdot[e]\cdot[H_2O]\} \\ &= -Q_{H_2}\cdot[H_2]+R_{H_2}\end{aligned} \tag{B.3}$$

$$\begin{aligned}\frac{d[OH]}{dt} &= -\{(k_{33}+k_{34}+k_{35}+k_{36})\cdot[e]+g_{37}+g_{38}+g_{39}+g_{40}+D_{OH} \\ &\quad +k_{50}\cdot[O]+k_{66}\cdot[H^+]+k_{71}\cdot[O^+]\big\}\cdot[OH] \\ &\quad +\{(k_3+k_5)\cdot[e]\cdot[H_2O]+(g_6+g_{12})\cdot[H_2O]+k_{48}\cdot[O_2]\cdot[H] \\ &\quad +k_{56}\cdot[H_2O]\cdot[H_2O^+]\} \\ &= -Q_{OH}\cdot[OH]+R_{OH}\end{aligned} \tag{B.4}$$

$$\begin{aligned}\frac{d[H_3O^+]}{dt} &= -\{(k_{42}+k_{43}+k_{44}+k_{45})\cdot[e]\}\cdot[H_3O^+] \\ &\quad +\big\{k_{56}\cdot[H_2O]\cdot[H_2O^+]+k_{61}\cdot[OH^+]\cdot[H_2O]\big\} \\ &= -Q_{H_3O^+}\cdot[H_3O^+]+R_{H_3O^+}\end{aligned} \tag{B.5}$$

$$\begin{aligned}\frac{d[H]}{dt} &= -\big\{k_{46}\cdot[e]+g_{47}+k_{48}\cdot[O_2]+k_{67}\cdot[H^+]+k_{69}\cdot[O^+]\big\}\cdot[H] \\ &\quad +\{2\cdot g_8\cdot[H_2O]+2\cdot g_{30}\cdot[H_2]+k_{50}\cdot[O]\cdot[OH]\} \\ &= -Q_H\cdot[H]+R_H\end{aligned} \tag{B.6}$$

$$\begin{aligned}
\frac{d[O]}{dt} &= -\Big\{k_{49}\cdot[e]+k_{50}\cdot[OH]+g_{51}+D_O+k_{64}\cdot[H^+] \\
&\quad +k_{72}\cdot[O^+]\Big\}\cdot[O] \\
&\quad +\{(g_7+g_8)\cdot[H_2O]+(k_{35}+k_{36})\cdot[e]\cdot[OH]+(g_{37}+g_{38}+g_{39})\cdot[OH] \\
&\quad +k_{48}\cdot[O_2]\cdot[H]\} \\
&= -Q_O\cdot[O]+R_O
\end{aligned} \tag{B.7}$$

$$\begin{aligned}
\frac{d[H_2O^+]}{dt} &= -\{(k_{53}+k_{54}+k_{55})\cdot[e]+k_{56}\cdot[H_2O]\}\cdot[H_2O^+] \\
&\quad +\Big\{k_1\cdot[e]\cdot[H_2O]+g_9\cdot[H_2O]+k_{60}\cdot[OH^+]\cdot[H_2O] \\
&\quad +\cdot k_{63}\cdot[H^+]\cdot[H_2O]+k_{70}\cdot[O^+]\cdot[H_2O]\Big\} \\
&= -Q_{H_2O^+}\cdot[H_2O^+]+R_{H_2O^+}
\end{aligned} \tag{B.8}$$

$$\begin{aligned}
\frac{d[OH^+]}{dt} &= -\{(k_{57}+k_{58}+k_{59})\cdot[e]+(k_{60}+k_{61})\cdot[H_2O]\}\cdot[OH^+] \\
&\quad +\{k_2\cdot[e]\cdot[H_2O]+g_{10}\cdot[H_2O]+k_{33}\cdot[e]\cdot[OH]+g_{40}\cdot[OH] \\
&\quad +k_{54}\cdot[e]\cdot[H_2O^+]+k_{66}\cdot[H^+]\cdot[OH]+k_{71}\cdot[O^+]\cdot[OH]\Big\} \\
&= -Q_{OH^+}\cdot[OH^+]+R_{OH^+}
\end{aligned} \tag{B.9}$$

$$\begin{aligned}
\frac{d[H_2^+]}{dt} &= -\{\cdot k_{62}\cdot[e]\}\cdot[H_2^+] \\
&\quad +\Big\{k_{23}\cdot[e]\cdot[H_2]+g_{31}\cdot[H_2]+k_{68}\cdot[H^+]\cdot[H_2]+k_{72}\cdot[O^+]\cdot[H_2]\Big\} \\
&= -Q_{H_2^+}\cdot[H_2^+]+R_{H_2^+}
\end{aligned} \tag{B.10}$$

$$\begin{aligned}
\frac{d[H^+]}{dt} &= -\{k_{63}\cdot[H_2O]+k_{64}\cdot[O]+k_{65}\cdot[O_2]+k_{66}\cdot[OH] \\
&\quad +k_{67}\cdot[H]+k_{68}\cdot[H_2]\}\cdot[H^+] \\
&\quad +\{k_3\cdot[e]\cdot[H_2O]+g_{12}\cdot[H_2O]+k_{22}\cdot[e]\cdot[H_2]+g_{32}\cdot[H_2] \\
&\quad +k_{35}\cdot[e]\cdot[OH]+k_{46}\cdot[e]\cdot[H]+g_{47}\cdot[H] \\
&\quad +k_{55}\cdot[e]\cdot[H_2O^+]+k_{59}\cdot[e]\cdot[OH^+] \\
&\quad +k_{67}\cdot[H^+]\cdot[H]+k_{69}\cdot[O^+]\cdot[H]\Big\} \\
&= -Q_{H^+}\cdot[H^+]+R_{H^+}
\end{aligned} \tag{B.11}$$

$$
\begin{aligned}
\frac{d[O^+]}{dt} &= -\{k_{69}\cdot[H] + k_{70}\cdot[H_2O] + k_{71}\cdot[OH] + k_{72}\cdot[O] \\
&\quad +k_{73}\cdot[H_2] + k_{74}\cdot[O_2]\}\cdot[O^+] \\
&\quad +\{k_4\cdot[e]\cdot[H_2O] + g_{11}\cdot[H_2O] + k_{15}\cdot[e]\cdot[O_2] + g_{20}\cdot[O_2] \\
&\quad +k_{34}\cdot[e]\cdot[OH] + k_{49}\cdot[e]\cdot[O] + g_{51}\cdot[O] + k_{58}\cdot[e]\cdot[OH^+] \\
&\quad +k_{64}\cdot[H^+]\cdot[O] + k_{72}\cdot[O^+]\cdot[O] + k_{76}\cdot[e]\cdot[O_2^+]\big\} \\
&= -Q_{O_2^+}\cdot[O_2^+] + R_{O_2^+}
\end{aligned}
\tag{B.12}
$$

$$
\begin{aligned}
\frac{d[O_2^+]}{dt} &= -\{(k_{75}+k_{76})\cdot[e]\}\cdot[O_2^+] \\
&\quad +\big\{k_{14}\cdot[e]\cdot[O_2] + g_{19}\cdot[O_2] + k_{65}\cdot[H^+]\cdot[O_2] + k_{74}\cdot[O^+]\cdot[O_2]\big\} \\
&= -Q_{O_2^+}\cdot[O_2^+] + R_{O_2^+}
\end{aligned}
\tag{B.13}
$$

Appendix C

Water chemistry architecture file

The water chemistry architecture file, h2og.mdf, describes all of the chemical reactions used by the chemistry code. A listing of the file follows this description of its contents.

The header lines contain the name of the base species for the chemistry and the multiplicity.

The remaining data are divided into blocks of lines and labelled by species. Table C.1 lists the species and their labels. There are three different kinds of lines of data in the file, labelled either 'A', 'B', or 'C'. The 'A' lines identify the primary species with which each reaction is associated. The 'B' line pairs describe the species involved in a reaction, and the 'C' line pairs contain rate coefficient data.

For each reaction, the first pair of 'C' lines for each reaction encodes the number of 'C' line pairs which must be read to obtain all of the rate coefficients defined for the reaction. Multiple collision strength terms Ω may be needed to model the shape of the cross section data, and each term will have a pair of 'C' lines containing the nine rate coefficients C and threshold energy E_{ij} fitted in the analytic formulation of Ω, e.g. Equation 2.7. The 'C' line pair also indicates the procedure used to calculate the rate coefficient k_{ij} for the reaction (c.f. Appendix A); specifies the analytic formulation used to calculate Ω_{ij} from the rate coefficients C_n (e.g. Equation 2.7); and identifies the impactor species, i.e. the faster of the two reactants (the other reactant is the target species).

Each reaction has one pair of 'B' lines which encodes the reactant species and the number(s) of each reactant involved in the reaction; the product species and the number(s)

Table C.1. Species in the inner magnetospheric chemistry system and their labels

Label	Species
1	H_2O
2	O_2
3	H_2
4	OH
5	H_3O^++
6	H
7	O
8	H_2O^++
9	OH^+
10	H_2^+
11	H^+
12	O^+
13	O_2^+

of each product; and how many of the products are retained. If there are energetic neutral products which escape the inner magnetosphere, the diffused-in replacement species (H_2O in this work) and a mass factor used to conserve the number of heavy particles (i.e., atoms; if OH is lost, it is replaced by two heavy particles while O or H would be replaced by one heavy particle) are specified. The 'B' line pair also contains the degeneracy for the reaction.

```
*** H2O  - Molec  DATA *** 4 Rs  most recently updated:  15 Mar. 2011
 5,0,I.P.=13.618 eV

  1A,H2O             ,0, 0, 0,      0.000,
  1C, .0000000E+00, .0000000E+00, .0000000E+00, .0000000E+00, .0000000E+00,
0300, .0000000E+00, .0000000E+00, .0000000E+00, .0000000E+00, .3674986E+06,
  1C, .6155910E+01, .1229022E+01, .0000000E+00, .0000000E+00, .1682829E+01,
1000,-.1423998E+02, .1423998E+02, .7425393E+01, .9418800E-01, .1463845E+06,satmag_col0(12)
  1C, .3693547E+01, .7374133E+00, .0000000E+00, .0000000E+00, .1009697E+01,
1000,-.8543989E+01, .8543989E+01, .4455236E+01, .9418800E-01, .1605878E+06,satmag_col0(13)
  1C, .2462365E+01, .4916088E+00, .0000000E+00, .0000000E+00, .6731315E+00,
1000,-.5695993E+01, .5695993E+01, .2970157E+01, .9418800E-01, .1969547E+06,satmag_col0(14)
  1B, 1234.56,OM(  1,  0: 1, 0)/GJJ=.1000E+01,A(  0,  0: 0, 0)=.0000E+00,.0000E+00,
  1B, 1234.56,OM(  8,  0: 1, 0)/GJJ=.1000E+01,A(  0,  0: 0, 0)=.0000E+00,.0000E+00,
  1C, .0000000E+00, .0000000E+00, .0000000E+00, .0000000E+00, .0000000E+00,
0100, .0000000E+00, .0000000E+00, .0000000E+00, .0000000E+00, .3674986E+06,
  1C, .6218600E+01, .1241538E+01, .0000000E+00, .0000000E+00, .1699660E+01,
1000,-.1438499E+02, .1438499E+02, .7501008E+01, .9418800E-01, .2030700E+06,satmag_col0(15)
  1B, 1234.56,OM(  1,  1: 1, 0)/GJJ=.1000E+01,A(  0,  0: 0, 0)=.0000E+00,.0000E+00,
  1B, 1234.56,OM(  9,  0: 1, 0)/GJJ=.1000E+01,A(  6,  1: 1, 0)=.0000E+00,.0000E+00,
  1C, .0000000E+00, .0000000E+00, .0000000E+00, .0000000E+00, .0000000E+00,
0100, .0000000E+00, .0000000E+00, .0000000E+00, .0000000E+00, .3674986E+06,
  1C, .5240675E+01, .1046296E+01, .0000000E+00, .0000000E+00, .1432632E+01,
1000,-.1212284E+02, .1212284E+02, .6321414E+01, .9418800E-01, .2610900E+06,satmag_col0(16)
  1B, 1234.56,OM(  1,  0: 1, 0)/GJJ=.1000E+01,A(  0,  0: 0, 0)=.0000E+00,.0000E+00,
  1B, 1234.56,OM( 11,  0: 1, 0)/GJJ=.1000E+01,A(  4,  0: 1, 0)=.0000E+00,.0000E+00,
  1C, .0000000E+00, .0000000E+00, .0000000E+00, .0000000E+00, .0000000E+00,
0100, .0000000E+00, .0000000E+00, .0000000E+00, .0000000E+00, .3674986E+06,
  1C, .1303900E+01, .2603224E+00, .0000000E+00, .0000000E+00, .3564444E+00,
1000,-.3016208E+01, .3016208E+01, .1572792E+01, .9418800E-01, .3307140E+06,satmag_col0(17)
  1B, 1234.56,OM(  1,  0: 1, 0)/GJJ=.1000E+01,A(  0,  0: 0, 0)=.0000E+00,.0000E+00,
```

```
  1B, 1234.56,OM( 12,  0: 1, 0)/GJJ=.1000E+01,A(  3,  0: 1, 0)=.0000E+00,.0000E+00,
  1C, .0000000E+00, .0000000E+00, .0000000E+00, .0000000E+00, .0000000E+00,
0400, .0000000E+00, .0000000E+00, .0000000E+00, .0000000E+00, .3674986E+06,
  1C, .0000000E+00,-.3849280E-01, .1014720E-05, .0000000E+00,-.7253520E-01,
1000,-.1303360E-01, .1303360E-01, .8844800E-01, .1698200E+00, .6788340E+05,col_h2o_02(80)
  1C, .0000000E+00,-.4811600E-01, .1268400E-05, .0000000E+00,-.9066900E-01,
1000,-.1629200E-01, .1629200E-01, .1105600E+00, .1698200E+00, .7771199E+05,col_h2o_02(81)
  1C, .0000000E+00,-.5773920E-01, .1522080E-05, .0000000E+00,-.1088028E+00,
1000,-.1955040E-01, .1955040E-01, .1326720E+00, .1698200E+00, .8072903E+05,col_h2o_02(82)
  1C, .0000000E+00,-.4667252E+01, .1230348E-03, .0000000E+00,-.8794893E+01,
1000,-.1580324E+01, .1580324E+01, .1072432E+02, .1698200E+00, .1101220E+06,col_h2o_02(83)
  1B, 1234.56,OM(  1,  1: 1, 0)/GJJ=.1000E+01,A(  0,  0: 0, 0)=.0000E+00,.0000E+00,
  1B, 1234.56,OM(  4,  0: 1, 0)/GJJ=.1000E+01,A(  6,  1: 1, 0)=.0000E+00,.0000E+00,
  1C, .0000000E+00, .0000000E+00, .0000000E+00, .0000000E+00, .0000000E+00,
0100, .0000000E+00, .0000000E+00, .0000000E+00, .0000000E+00, .1578621E+04,h2oph(18)
  1C, .0000000E+00, .0000000E+00, .0000000E+00, .0000000E+00, .0000000E+00
5000, .0000000E+00, .0000000E+00, .0000000E+00, .0000000E+00, .1578621E+04,
  1B, 2426.60,OM(  1,  1: 1, 0)/GJJ=.1000E+01,A(  0,  0: 0, 0)=.1546E-06,.0000E+00,
  1B, 2426.60,OM(  4,  0: 1, 0)/GJJ=.1000E+01,A(  6,  1: 1, 0)=.1546E-06,.0000E+00,
  1C, .0000000E+00, .0000000E+00, .0000000E+00, .0000000E+00, .0000000E+00,
0100, .0000000E+00, .0000000E+00, .0000000E+00, .0000000E+00, .1151471E+04,h2oph(19)
  1C, .0000000E+00, .0000000E+00, .0000000E+00, .0000000E+00, .0000000E+00
5000, .0000000E+00, .0000000E+00, .0000000E+00, .0000000E+00, .1151471E+04,
  1B, 1770.00,OM(  1,  1: 1, 0)/GJJ=.1000E+01,A(  0,  0: 0, 0)=.1151E-07,.0000E+00,
  1B, 1770.00,OM(  7,  0: 1, 0)/GJJ=.1000E+01,A(  3,  1: 1, 0)=.1151E-07,.0000E+00,
  1C, .0000000E+00, .0000000E+00, .0000000E+00, .0000000E+00, .0000000E+00,
0100, .0000000E+00, .0000000E+00, .0000000E+00, .0000000E+00, .8483152E+03,h2oph(20)
  1C, .0000000E+00, .0000000E+00, .0000000E+00, .0000000E+00, .0000000E+00
5000, .0000000E+00, .0000000E+00, .0000000E+00, .0000000E+00, .8483152E+03,
  1B, 1304.00,OM(  1,  0: 1, 0)/GJJ=.1000E+01,A(  0,  0: 0, 0)=.1476E-07,.0000E+00,
  1B, 1304.00,OM(  7,  0: 1, 0)/GJJ=.1000E+01,A(  6,  0: 2, 0)=.1476E-07,.0000E+00,
```

```
  1C, .0000000E+00, .0000000E+00, .0000000E+00, .0000000E+00, .0000000E+00,
0100, .0000000E+00, .0000000E+00, .0000000E+00, .0000000E+00, .6401397E+03,h2oph(21)
  1C, .0000000E+00, .0000000E+00, .0000000E+00, .0000000E+00, .0000000E+00
5000, .0000000E+00, .0000000E+00, .0000000E+00, .0000000E+00, .6401397E+03,
  1B,  984.00,OM(  1,  0: 1, 0)/GJJ=.1000E+01,A(  0,  0: 0, 0)=.6421E-08,.0000E+00,
  1B,  984.00,OM(  8,  0: 1, 0)/GJJ=.1000E+01,A(  0,  0: 0, 0)=.6421E-08,.0000E+00,
  1C, .0000000E+00, .0000000E+00, .0000000E+00, .0000000E+00, .0000000E+00,
0100, .0000000E+00, .0000000E+00, .0000000E+00, .0000000E+00, .4452354E+03,h2oph(22)
  1C, .0000000E+00, .0000000E+00, .0000000E+00, .0000000E+00, .0000000E+00
5000, .0000000E+00, .0000000E+00, .0000000E+00, .0000000E+00, .4452354E+03,
  1B,  684.40,OM(  1,  1: 1, 0)/GJJ=.1000E+01,A(  0,  0: 0, 0)=.1143E-08,.0000E+00,
  1B,  684.40,OM(  9,  0: 1, 0)/GJJ=.1000E+01,A(  6,  1: 1, 0)=.1143E-08,.0000E+00,
  1C, .0000000E+00, .0000000E+00, .0000000E+00, .0000000E+00, .0000000E+00,
0100, .0000000E+00, .0000000E+00, .0000000E+00, .0000000E+00, .4324846E+03,h2oph(23)
  1C, .0000000E+00, .0000000E+00, .0000000E+00, .0000000E+00, .0000000E+00
5000, .0000000E+00, .0000000E+00, .0000000E+00, .0000000E+00, .4324846E+03,
  1B,  664.80,OM(  1,  1: 1, 0)/GJJ=.1000E+01,A(  0,  0: 0, 0)=.1548E-09,.0000E+00,
  1B,  664.80,OM( 12,  0: 1, 0)/GJJ=.1000E+01,A(  3,  1: 1, 0)=.1548E-09,.0000E+00,
  1C, .0000000E+00, .0000000E+00, .0000000E+00, .0000000E+00, .0000000E+00,
0100, .0000000E+00, .0000000E+00, .0000000E+00, .0000000E+00, .4308583E+03,h2oph(24)
  1C, .0000000E+00, .0000000E+00, .0000000E+00, .0000000E+00, .0000000E+00
5000, .0000000E+00, .0000000E+00, .0000000E+00, .0000000E+00, .4308583E+03,
  1B,  662.30,OM(  1,  0: 1, 0)/GJJ=.1000E+01,A(  0,  0: 0, 0)=.2327E-09,.0000E+00,
  1B,  662.30,OM(  4,  0: 1, 0)/GJJ=.1000E+01,A( 11,  0: 1, 0)=.2327E-09,.0000E+00,

  2A,O2              ,0, 0, 0,  35407.725,
  2C, .0000000E+00, .0000000E+00, .0000000E+00, .0000000E+00, .0000000E+00,
0500, .0000000E+00, .0000000E+00, .0000000E+00, .0000000E+00, .3674986E+06,
  2C, .0000000E+00,-.2628600E-04, .0000000E+00, .0000000E+00, .0000000E+00,
1010,-.3450100E+00, .4760700E+00, .1409300E+01, .3981100E-01, .8219113E+05,col_O2_00(19)
  2C, .0000000E+00, .3993500E+00,-.1529600E+01, .2719500E+01,-.1796900E+01,
```

```
1010, .1440100E-01, .2381800E-01, .0000000E+00, .2187800E+00, .5935446E+05,col_O2_00(20)
  2C, .0000000E+00,-.4892100E-01, .5684400E+00,-.1045500E+01, .5696100E+00,
1010, .4758000E-02,-.2591500E-01, .0000000E+00, .1023300E+00, .5935446E+05,col_O2_00(21)
  2C, .0000000E+00, .2170500E+01,-.2837900E+02, .9750000E+02,-.1080500E+03,
1010, .1264600E+00, .4539200E-01, .0000000E+00, .1023300E+01, .5944729E+05,col_O2_00(22)
  2C, .0000000E+00, .4158800E+00, .0000000E+00, .0000000E+00, .0000000E+00,
1000,-.6387100E+00, .6387100E+00, .5145900E+00, .3890400E+00, .1160400E+06,col_O2_00(23)
  2B, 1234.56,OM(  2,  2: 1, 0)/GJJ=.1000E+01,A(  0,  0: 0, 0)=.0000E+00,.0000E+00,
  2B, 1234.56,OM(  7,  1: 1, 0)/GJJ=.1000E+01,A(  7,  1: 1, 0)=.0000E+00,.0000E+00,
  2C, .0000000E+00, .0000000E+00, .0000000E+00, .0000000E+00, .0000000E+00,
0100, .0000000E+00, .0000000E+00, .0000000E+00, .0000000E+00, .3674986E+06,
  2C,-.2316100E+02, .3079500E+01, .4029000E+01, .0000000E+00, .4734700E+02,
1000, .1134500E+01,-.1134490E+01, .0000000E+00, .1230300E+00, .1400603E+06,col_h2o_02(109)
  2B, 1234.56,OM(  2,  0: 1, 0)/GJJ=.1000E+01,A(  0,  0: 0, 0)=.0000E+00,.0000E+00,
  2B, 1234.56,OM( 13,  0: 1, 0)/GJJ=.1000E+01,A(  0,  0: 0, 0)=.0000E+00,.0000E+00,
  2C, .0000000E+00, .0000000E+00, .0000000E+00, .0000000E+00, .0000000E+00,
0200, .0000000E+00, .0000000E+00, .0000000E+00, .0000000E+00, .3674986E+06,
  2C,-.1554600E+02, .1089600E+01, .1476700E+01,-.1908200E+01, .2229400E+02,
1000, .7650500E-04, .0000000E+00, .0000000E+00, .1174900E+00, .2173429E+06,col_h2o_02(107)
  2C, .0000000E+00, .4295400E+01,-.3684100E+02, .1422400E+03,-.1699200E+03,
1000, .0000000E+00, .0000000E+00, .0000000E+00, .7585700E+00, .5778792E+07,col_h2o_02(108)
  2B, 1234.56,OM(  2,  1: 1, 0)/GJJ=.1000E+01,A(  0,  0: 0, 0)=.0000E+00,.0000E+00,
  2B, 1234.56,OM( 12,  0: 1, 0)/GJJ=.1000E+01,A(  7,  1: 1, 0)=.0000E+00,.0000E+00,
  2C, .0000000E+00, .0000000E+00, .0000000E+00, .0000000E+00, .0000000E+00,
0100, .0000000E+00, .0000000E+00, .0000000E+00, .0000000E+00, .1576734E+04,h2oph(13)
  2C, .0000000E+00, .0000000E+00, .0000000E+00, .0000000E+00, .0000000E+00
5000, .0000000E+00, .0000000E+00, .0000000E+00, .0000000E+00, .1576734E+04,
  2B, 2423.70,OM(  2,  2: 1, 0)/GJJ=.1000E+01,A(  0,  0: 0, 0)=.1994E-08,.0000E+00,
  2B, 2423.70,OM(  7,  1: 1, 0)/GJJ=.1000E+01,A(  7,  1: 1, 0)=.1994E-08,.0000E+00,
  2C, .0000000E+00, .0000000E+00, .0000000E+00, .0000000E+00, .0000000E+00,
0100, .0000000E+00, .0000000E+00, .0000000E+00, .0000000E+00, .1144315E+04,h2oph(14)
```

```
  2C, .0000000E+00, .0000000E+00, .0000000E+00, .0000000E+00, .0000000E+00
5000, .0000000E+00, .0000000E+00, .0000000E+00, .0000000E+00, .1144315E+04,
  2B, 1759.00,OM(  2,  2: 1, 0)/GJJ=.1000E+01,A(  0,  0: 0, 0)=.5828E-07,.0000E+00,
  2B, 1759.00,OM(  7,  1: 1, 0)/GJJ=.1000E+01,A(  7,  1: 1, 0)=.5828E-07,.0000E+00,
  2C, .0000000E+00, .0000000E+00, .0000000E+00, .0000000E+00, .0000000E+00,
0100, .0000000E+00, .0000000E+00, .0000000E+00, .0000000E+00, .6004562E+03,h2oph(15)
  2C, .0000000E+00, .0000000E+00, .0000000E+00, .0000000E+00, .0000000E+00
5000, .0000000E+00, .0000000E+00, .0000000E+00, .0000000E+00, .6004562E+03,
  2B,  923.00,OM(  2,  2: 1, 0)/GJJ=.1000E+01,A(  0,  0: 0, 0)=.7341E-09,.0000E+00,
  2B,  923.00,OM(  7,  1: 1, 0)/GJJ=.1000E+01,A(  7,  1: 1, 0)=.7341E-09,.0000E+00,
  2C, .0000000E+00, .0000000E+00, .0000000E+00, .0000000E+00, .0000000E+00,
0100, .0000000E+00, .0000000E+00, .0000000E+00, .0000000E+00, .6686337E+03,h2oph(16)
  2C, .0000000E+00, .0000000E+00, .0000000E+00, .0000000E+00, .0000000E+00
5000, .0000000E+00, .0000000E+00, .0000000E+00, .0000000E+00, .6686337E+03,
  2B, 1027.80,OM(  2,  0: 1, 0)/GJJ=.1000E+01,A(  0,  0: 0, 0)=.9108E-08,.0000E+00,
  2B, 1027.80,OM( 13,  0: 1, 0)/GJJ=.1000E+01,A(  0,  0: 0, 0)=.9108E-08,.0000E+00,
  2C, .0000000E+00, .0000000E+00, .0000000E+00, .0000000E+00, .0000000E+00,
0100, .0000000E+00, .0000000E+00, .0000000E+00, .0000000E+00, .3805709E+03,h2oph(17)
  2C, .0000000E+00, .0000000E+00, .0000000E+00, .0000000E+00, .0000000E+00
5000, .0000000E+00, .0000000E+00, .0000000E+00, .0000000E+00, .3805709E+03,
  2B,  585.00,OM(  2,  1: 1, 0)/GJJ=.1000E+01,A(  0,  0: 0, 0)=.2532E-08,.0000E+00,
  2B,  585.00,OM( 12,  0: 1, 0)/GJJ=.1000E+01,A(  7,  1: 1, 0)=.2532E-08,.0000E+00,

  3A,H2              ,0, 0, 0,  39918.621,
  3C, .0000000E+00, .0000000E+00, .0000000E+00, .0000000E+00, .0000000E+00,
0100, .0000000E+00, .0000000E+00, .0000000E+00, .0000000E+00, .3674986E+06,
  3C,-.2216000E+01, .7859000E+01, .0000000E+00, .0000000E+00, .0000000E+00,
1000, .1000000E-01,-.1000000E-01, .0000000E+00, .7900000E+00, .1021152E+06,satmag_col0(10)
  3B, 1234.56,OM(  3,  2: 1, 0)/GJJ=.1000E+01,A(  0,  0: 0, 0)=.0000E+00,.0000E+00,
  3B, 1234.56,OM(  6,  1: 1, 0)/GJJ=.1000E+01,A(  6,  1: 1, 0)=.0000E+00,.0000E+00,
  3C, .0000000E+00, .0000000E+00, .0000000E+00, .0000000E+00, .0000000E+00,
```

```
0200, .0000000E+00, .0000000E+00, .0000000E+00, .0000000E+00, .3674986E+06,
  3C, .0000000E+00, .1458990E-01, .2005560E-01, .0000000E+00, .1893150E-01,
1000,-.7269390E-01, .7269390E-01, .4176720E-01, .8669600E-01, .2159504E+06,satmag_col0(26)
  3C, .0000000E+00, .1475201E+00, .2027844E+00, .0000000E+00, .1914185E+00,
1000,-.7350161E+00, .7350161E+00, .4229680E+00, .8669600E-01, .3272328E+06,satmag_col0(27)
  3B, 1234.56,OM(  3,  1: 1, 0)/GJJ=.1000E+01,A(  0,  0: 0, 0)=.0000E+00,.0000E+00,
  3B, 1234.56,OM( 11,  0: 1, 0)/GJJ=.1000E+01,A(  6,  1: 1, 0)=.0000E+00,.0000E+00,
  3C, .0000000E+00, .0000000E+00, .0000000E+00, .0000000E+00, .0000000E+00,
0100, .0000000E+00, .0000000E+00, .0000000E+00, .0000000E+00, .3674986E+06,
  3C, .0000000E+00,-.1659200E+01, .0000000E+00, .0000000E+00, .0000000E+00,
1000,-.3232400E+01, .3232400E+01, .5690300E+01, .5754400E+00, .1794744E+06,satmag_col0(28)
  3B, 1234.56,OM(  3,  0: 1, 0)/GJJ=.1000E+01,A(  0,  0: 0, 0)=.0000E+00,.0000E+00,
  3B, 1234.56,OM( 10,  0: 1, 0)/GJJ=.1000E+01,A(  0,  0: 0, 0)=.0000E+00,.0000E+00,
  3C, .0000000E+00, .0000000E+00, .0000000E+00, .0000000E+00, .0000000E+00,
0100, .0000000E+00, .0000000E+00, .0000000E+00, .0000000E+00, .3674986E+06,
  3C,-.6891500E+00, .2444100E+01, .0000000E+00, .0000000E+00, .0000000E+00,
1000, .3110000E-02,-.3110000E-02, .0000000E+00, .7900000E+00, .1021152E+06,satmag_col0(143)
  3B, 1234.56,OM(  3,  2: 1, 0)/GJJ=.1000E+01,A(  0,  0: 0, 0)=.0000E+00,.0000E+00,
  3B, 1234.56,OM(  6,  1: 1, 0)/GJJ=.1000E+01,A(  6,  1: 1, 0)=.0000E+00,.0000E+00,
  3C, .0000000E+00, .0000000E+00, .0000000E+00, .0000000E+00, .0000000E+00,
0100, .0000000E+00, .0000000E+00, .0000000E+00, .0000000E+00, .3674986E+06,
  3C,-.1274200E+01, .2010680E+02,-.1964120E+02, .1407080E+04,-.3865930E+01,
1000, .1688930E+00,-.1688930E+00, .0000000E+00, .1830000E+01, .1365095E+06,satmag_col0(144)
  3B, 1234.56,OM(  3,  2: 1, 0)/GJJ=.1000E+01,A(  0,  0: 0, 0)=.0000E+00,.0000E+00,
  3B, 1234.56,OM(  6,  1: 1, 0)/GJJ=.1000E+01,A(  6,  1: 1, 0)=.0000E+00,.0000E+00,
  3C, .0000000E+00, .0000000E+00, .0000000E+00, .0000000E+00, .0000000E+00,
0100, .0000000E+00, .0000000E+00, .0000000E+00, .0000000E+00, .3674986E+06,
  3C, .6806130E+00, .7347900E+00,-.5991950E+02, .1021350E+04,-.4259010E+04,
1000, .3512180E-04,-.3512180E-04, .0000000E+00, .1780000E+01, .1367879E+06,satmag_col0(145)
  3B, 1234.56,OM(  3,  2: 1, 0)/GJJ=.1000E+01,A(  0,  0: 0, 0)=.0000E+00,.0000E+00,
  3B, 1234.56,OM(  6,  1: 1, 0)/GJJ=.1000E+01,A(  6,  1: 1, 0)=.0000E+00,.0000E+00,
```

```
  3C, .0000000E+00, .0000000E+00, .0000000E+00, .0000000E+00, .0000000E+00,
0100, .0000000E+00, .0000000E+00, .0000000E+00, .0000000E+00, .3674986E+06,
  3C, .1463130E+02,-.4959010E+00,-.2771830E+02, .9389070E+02,-.2251870E+03,
1000, .0000000E+00, .0000000E+00, .0000000E+00, .6200000E+00, .1542752E+06,satmag_col0(146)
  3B, 1234.56,OM(  3,  2: 1, 0)/GJJ=.1000E+01,A(  0,  0: 0, 0)=.0000E+00,.0000E+00,
  3B, 1234.56,OM(  6,  1: 1, 0)/GJJ=.1000E+01,A(  6,  1: 1, 0)=.0000E+00,.0000E+00,
  3C, .0000000E+00, .0000000E+00, .0000000E+00, .0000000E+00, .0000000E+00,
0100, .0000000E+00, .0000000E+00, .0000000E+00, .0000000E+00, .3674986E+06,
  3C, .2220490E+00, .1050470E+00,-.3875900E+00,-.8474000E+01, .8726170E+02,
1000, .0000000E+00, .0000000E+00, .0000000E+00, .1170000E+01, .1614232E+06,satmag_col0(147)
  3B, 1234.56,OM(  3,  2: 1, 0)/GJJ=.1000E+01,A(  0,  0: 0, 0)=.0000E+00,.0000E+00,
  3B, 1234.56,OM(  6,  1: 1, 0)/GJJ=.1000E+01,A(  6,  1: 1, 0)=.0000E+00,.0000E+00,
  3C, .0000000E+00, .0000000E+00, .0000000E+00, .0000000E+00, .0000000E+00,
0100, .0000000E+00, .0000000E+00, .0000000E+00, .0000000E+00, .1801271E+04,h2oph(5)
  3C, .0000000E+00, .0000000E+00, .0000000E+00, .0000000E+00, .0000000E+00
5000, .0000000E+00, .0000000E+00, .0000000E+00, .0000000E+00, .1801271E+04,
  3B, 2768.85,OM(  3,  2: 1, 0)/GJJ=.1000E+01,A(  0,  0: 0, 0)=.8698E-09,.0000E+00,
  3B, 2768.85,OM(  6,  1: 1, 0)/GJJ=.1000E+01,A(  6,  1: 1, 0)=.8698E-09,.0000E+00,
  3C, .0000000E+00, .0000000E+00, .0000000E+00, .0000000E+00, .0000000E+00,
0100, .0000000E+00, .0000000E+00, .0000000E+00, .0000000E+00, .5495768E+03,h2oph(6)
  3C, .0000000E+00, .0000000E+00, .0000000E+00, .0000000E+00, .0000000E+00
5000, .0000000E+00, .0000000E+00, .0000000E+00, .0000000E+00, .5495768E+03,
  3B,  844.79,OM(  3,  2: 1, 0)/GJJ=.1000E+01,A(  0,  0: 0, 0)=.6454E-09,.0000E+00,
  3B,  844.79,OM(  6,  1: 1, 0)/GJJ=.1000E+01,A(  6,  1: 1, 0)=.6454E-09,.0000E+00,
  3C, .0000000E+00, .0000000E+00, .0000000E+00, .0000000E+00, .0000000E+00,
0100, .0000000E+00, .0000000E+00, .0000000E+00, .0000000E+00, .5228263E+03,h2oph(7)
  3C, .0000000E+00, .0000000E+00, .0000000E+00, .0000000E+00, .0000000E+00
5000, .0000000E+00, .0000000E+00, .0000000E+00, .0000000E+00, .5228263E+03,
  3B,  803.67,OM(  3,  0: 1, 0)/GJJ=.1000E+01,A(  0,  0: 0, 0)=.3634E-09,.0000E+00,
  3B,  803.67,OM( 10,  0: 1, 0)/GJJ=.1000E+01,A(  0,  0: 0, 0)=.3634E-09,.0000E+00,
  3C, .0000000E+00, .0000000E+00, .0000000E+00, .0000000E+00, .0000000E+00,
```

```
0100, .0000000E+00, .0000000E+00, .0000000E+00, .0000000E+00, .4526516E+03,h2oph(8)
  3C, .0000000E+00, .0000000E+00, .0000000E+00, .0000000E+00, .0000000E+00
5000, .0000000E+00, .0000000E+00, .0000000E+00, .0000000E+00, .4526516E+03,
  3B,  695.80,OM(  3,  1: 1, 0)/GJJ=.1000E+01,A(  0,  0: 0, 0)=.2073E-09,.0000E+00,
  3B,  695.80,OM( 11,  0: 1, 0)/GJJ=.1000E+01,A(  6,  1: 1, 0)=.2073E-09,.0000E+00,

  4A,OH              ,0, 0, 0,  41243.950,
  4C, .0000000E+00, .0000000E+00, .0000000E+00, .0000000E+00, .0000000E+00,
0100, .0000000E+00, .0000000E+00, .0000000E+00, .0000000E+00, .3674986E+06,
  4C, .0000000E+00, .0000000E+00, .0000000E+00, .0000000E+00, .0000000E+00,
1000,-.1302800E+02, .1302800E+02, .1302800E+02, .0000000E+00, .1496916E+06,satmag_col0(29)
  4B, 1234.56,OM(  4,  0: 1, 0)/GJJ=.1000E+01,A(  0,  0: 0, 0)=.0000E+00,.0000E+00,
  4B, 1234.56,OM(  9,  0: 1, 0)/GJJ=.1000E+01,A(  0,  0: 0, 0)=.0000E+00,.0000E+00,
  4C, .0000000E+00, .0000000E+00, .0000000E+00, .0000000E+00, .0000000E+00,
0100, .0000000E+00, .0000000E+00, .0000000E+00, .0000000E+00, .3674986E+06,
  4C, .0000000E+00, .0000000E+00, .0000000E+00, .0000000E+00, .0000000E+00,
1000,-.8690000E+01, .8690000E+01, .8690000E+01, .0000000E+00, .2088952E+06,satmag_col0(32)
  4B, 1234.56,OM(  4,  1: 1, 0)/GJJ=.1000E+01,A(  0,  0: 0, 0)=.0000E+00,.0000E+00,
  4B, 1234.56,OM( 12,  0: 1, 0)/GJJ=.1000E+01,A(  6,  1: 1, 0)=.0000E+00,.0000E+00,
  4C, .0000000E+00, .0000000E+00, .0000000E+00, .0000000E+00, .0000000E+00,
0100, .0000000E+00, .0000000E+00, .0000000E+00, .0000000E+00, .3674986E+06,
  4C, .0000000E+00, .0000000E+00, .0000000E+00, .0000000E+00, .0000000E+00,
1000,-.4000000E+01, .4000000E+01, .4000000E+01, .0000000E+00, .2088256E+06,satmag_col0(33)
  4B, 1234.56,OM(  4,  0: 1, 0)/GJJ=.1000E+01,A(  0,  0: 0, 0)=.0000E+00,.0000E+00,
  4B, 1234.56,OM(  7,  0: 1, 0)/GJJ=.1000E+01,A( 11,  0: 1, 0)=.0000E+00,.0000E+00,
  4C, .0000000E+00, .0000000E+00, .0000000E+00, .0000000E+00, .0000000E+00,
0300, .0000000E+00, .0000000E+00, .0000000E+00, .0000000E+00, .3674986E+06,
  4C, .0000000E+00, .0000000E+00, .0000000E+00, .0000000E+00, .0000000E+00,
1000,-.1383750E+00, .1383750E+00, .1383750E+00, .0000000E+00, .1003862E+06,satmag_col0(34)
  4C, .0000000E+00, .0000000E+00, .0000000E+00, .0000000E+00, .0000000E+00,
1000,-.2305750E+00, .2305750E+00, .2305750E+00, .0000000E+00, .1286884E+06,satmag_col0(35)
```

```
  4C, .0000000E+00, .0000000E+00, .0000000E+00, .0000000E+00, .0000000E+00,
1000,-.4296000E+01, .4296000E+01, .4296000E+01, .0000000E+00, .1322856E+06,satmag_col0(36)
  4B, 1234.56,OM(  4,  1: 1, 0)/GJJ=.1000E+01,A(  0,  0: 0, 0)=.0000E+00,.0000E+00,
  4B, 1234.56,OM(  7,  0: 1, 0)/GJJ=.1000E+01,A(  6,  1: 1, 0)=.0000E+00,.0000E+00,
  4C, .0000000E+00, .0000000E+00, .0000000E+00, .0000000E+00, .0000000E+00,
0100, .0000000E+00, .0000000E+00, .0000000E+00, .0000000E+00, .1836498E+04,h2oph(9)
  4C, .0000000E+00, .0000000E+00, .0000000E+00, .0000000E+00, .0000000E+00
5000, .0000000E+00, .0000000E+00, .0000000E+00, .0000000E+00, .1836498E+04,
  4B, 2823.00,OM(  4,  1: 1, 0)/GJJ=.1000E+01,A(  0,  0: 0, 0)=.1429E-06,.0000E+00,
  4B, 2823.00,OM(  7,  0: 1, 0)/GJJ=.1000E+01,A(  6,  1: 1, 0)=.1429E-06,.0000E+00,
  4C, .0000000E+00, .0000000E+00, .0000000E+00, .0000000E+00, .0000000E+00,
0100, .0000000E+00, .0000000E+00, .0000000E+00, .0000000E+00, .3326905E+04,h2oph(10)
  4C, .0000000E+00, .0000000E+00, .0000000E+00, .0000000E+00, .0000000E+00
5000, .0000000E+00, .0000000E+00, .0000000E+00, .0000000E+00, .3326905E+04,
  4B, 5114.00,OM(  4,  1: 1, 0)/GJJ=.1000E+01,A(  0,  0: 0, 0)=.1363E-06,.0000E+00,
  4B, 5114.00,OM(  7,  0: 1, 0)/GJJ=.1000E+01,A(  6,  1: 1, 0)=.1363E-06,.0000E+00,
  4C, .0000000E+00, .0000000E+00, .0000000E+00, .0000000E+00, .0000000E+00,
0100, .0000000E+00, .0000000E+00, .0000000E+00, .0000000E+00, .3989163E+05,h2oph(11)
  4C, .0000000E+00, .0000000E+00, .0000000E+00, .0000000E+00, .0000000E+00
5000, .0000000E+00, .0000000E+00, .0000000E+00, .0000000E+00, .3989163E+05,
  4B,61320.00,OM(  4,  1: 1, 0)/GJJ=.1000E+01,A(  0,  0: 0, 0)=.1631E-07,.0000E+00,
  4B,61320.00,OM(  7,  0: 1, 0)/GJJ=.1000E+01,A(  6,  1: 1, 0)=.1631E-07,.0000E+00,
  4C, .0000000E+00, .0000000E+00, .0000000E+00, .0000000E+00, .0000000E+00,
0100, .0000000E+00, .0000000E+00, .0000000E+00, .0000000E+00, .6037090E+03,h2oph(12)
  4C, .0000000E+00, .0000000E+00, .0000000E+00, .0000000E+00, .0000000E+00
5000, .0000000E+00, .0000000E+00, .0000000E+00, .0000000E+00, .6037090E+03,
  4B,  928.00,OM(  4,  0: 1, 0)/GJJ=.1000E+01,A(  0,  0: 0, 0)=.4909E-08,.0000E+00,
  4B,  928.00,OM(  9,  0: 1, 0)/GJJ=.1000E+01,A(  0,  0: 0, 0)=.4909E-08,.0000E+00,
  4C, .0000000E+00, .0000000E+00, .0000000E+00, .0000000E+00, .0000000E+00,
0100, .0000000E+00, .0000000E+00, .0000000E+00, .0000000E+00, .1098370E+06,DESemail14mar2011,
  4C, .0000000E+00, .0000000E+00, .0000000E+00, .0000000E+00, .0000000E+00,
```

```
6000, .0000000E+00, .0000000E+00, .0000000E+00, .0000000E+00, .1098370E+06,
  4B,  928.00,OM(  7,  1: 1, 0)/GJJ=.1000E+01,A(  0,  0: 0, 0)=.1400E-06,.0000E+00,
  4B,  928.00,OM(  7,  1: 1, 0)/GJJ=.1000E+01,A(  0,  0: 0, 0)=.1400E-06,.0000E+00,

  5A,H3O+            ,0, 0, 0,  65830.946,
  5C, .0000000E+00, .0000000E+00, .0000000E+00, .0000000E+00, .0000000E+00,
0200, .0000000E+00, .0000000E+00, .0000000E+00, .0000000E+00, .3674986E+06,
  5C,-.3138300E+00,-.8785800E+00,-.3921120E+00, .0000000E+00, .0000000E+00,
10b0, .0000000E+00, .1608552E+01, .0000000E+00, .4168700E+00, .1160400E+03,satmag_col0(1)
  5C, .3884940E-01,-.6611580E-01, .1037898E+00,-.1417068E+00, .0000000E+00,
1010, .0000000E+00, .0000000E+00, .0000000E+00, .3981100E+00, .4525560E+04,satmag_col0(2)
  5B, 1234.56,OM(  5,  2: 1, 0)/GJJ=.1000E+01,A(  0,  0: 0, 0)=.0000E+00,.0000E+00,
  5B, 1234.56,OM(  1,  1: 1, 0)/GJJ=.1000E+01,A(  6,  1: 1, 0)=.0000E+00,.0000E+00,
  5C, .0000000E+00, .0000000E+00, .0000000E+00, .0000000E+00, .0000000E+00,
0200, .0000000E+00, .0000000E+00, .0000000E+00, .0000000E+00, .3674986E+06,
  5C,-.1917850E+00,-.5369100E+00,-.2396240E+00, .0000000E+00, .0000000E+00,
10b0, .0000000E+00, .9830040E+00, .0000000E+00, .4168700E+00, .1160400E+03,satmag_col0(3)
  5C, .2374130E-01,-.4040410E-01, .6342710E-01,-.8659860E-01, .0000000E+00,
1010, .0000000E+00, .0000000E+00, .0000000E+00, .3981100E+00, .4525560E+04,satmag_col0(4)
  5B, 1234.56,OM(  5,  2: 1, 0)/GJJ=.1000E+01,A(  0,  0: 0, 0)=.0000E+00,.0000E+00,
  5B, 1234.56,OM(  3,  1: 1, 0)/GJJ=.1000E+01,A(  4,  1: 1, 0)=.0000E+00,.0000E+00,
  5C, .0000000E+00, .0000000E+00, .0000000E+00, .0000000E+00, .0000000E+00,
0200, .0000000E+00, .0000000E+00, .0000000E+00, .0000000E+00, .3674986E+06,
  5C,-.1168145E+01,-.3270270E+01,-.1459528E+01, .0000000E+00, .0000000E+00,
10b0, .0000000E+00, .5987388E+01, .0000000E+00, .4168700E+00, .1160400E+03,satmag_col0(5)
  5C, .1446061E+00,-.2460977E+00, .3863287E+00,-.5274642E+00, .0000000E+00,
1010, .0000000E+00, .0000000E+00, .0000000E+00, .3981100E+00, .4525560E+04,satmag_col0(6)
  5B, 1234.56,OM(  5,  2: 1, 0)/GJJ=.1000E+01,A(  0,  0: 0, 0)=.0000E+00,.0000E+00,
  5B, 1234.56,OM(  4,  1: 1, 0)/GJJ=.1000E+01,A(  6,  1: 2, 0)=.0000E+00,.0000E+00,
  5C, .0000000E+00, .0000000E+00, .0000000E+00, .0000000E+00, .0000000E+00,
0200, .0000000E+00, .0000000E+00, .0000000E+00, .0000000E+00, .3674986E+06,
```

```
  5C,-.6974000E-01,-.1952400E+00,-.8713600E-01, .0000000E+00, .0000000E+00,
10b0, .0000000E+00, .3574560E+00, .0000000E+00, .4168700E+00, .1160400E+03,satmag_col0(7)
  5C, .8633200E-02,-.1469240E-01, .2306440E-01,-.3149040E-01, .0000000E+00,
1010, .0000000E+00, .0000000E+00, .0000000E+00, .3981100E+00, .4525560E+04,satmag_col0(8)
  5B, 1234.56,OM(  5,  2: 1, 0)/GJJ=.1000E+01,A(  0,  0: 0, 0)=.0000E+00,.0000E+00,
  5B, 1234.56,OM(  7,  1: 2, 0)/GJJ=.1000E+01,A(  3,  1: 1, 0)=.0000E+00,.0000E+00,

  6A,H               ,0, 0, 0,  76667.807,
  6C, .0000000E+00, .0000000E+00, .0000000E+00, .0000000E+00, .0000000E+00,
0100, .0000000E+00, .0000000E+00, .0000000E+00, .0000000E+00, .3674986E+06,
  6C, .0000000E+00, .1396200E+01,-.4567100E+01, .7680500E+01,-.4665500E+01,
1000,-.1555200E+01, .1555500E+01, .2335650E+01, .1288200E+00, .1578608E+06,satmag_col0(9)
  6B, 1234.56,OM(  6,  0: 1, 0)/GJJ=.1000E+01,A(  0,  0: 0, 0)=.0000E+00,.0000E+00,
  6B, 1234.56,OM( 11,  0: 1, 0)/GJJ=.1000E+01,A(  0,  0: 0, 0)=.0000E+00,.0000E+00,
  6C, .0000000E+00, .0000000E+00, .0000000E+00, .0000000E+00, .0000000E+00,
0100, .0000000E+00, .0000000E+00, .0000000E+00, .0000000E+00, .5931376E+03,h2oph(1)
  6C, .0000000E+00, .0000000E+00, .0000000E+00, .0000000E+00, .0000000E+00
5000, .0000000E+00, .0000000E+00, .0000000E+00, .0000000E+00, .5931376E+03,
  6B,  911.75,OM(  6,  0: 1, 0)/GJJ=.1000E+01,A(  0,  0: 0, 0)=.1355E-08,.0000E+00,
  6B,  911.75,OM( 11,  0: 1, 0)/GJJ=.1000E+01,A(  0,  0: 0, 0)=.1355E-08,.0000E+00,
  6C, .0000000E+00, .0000000E+00, .0000000E+00, .0000000E+00, .0000000E+00,
0100, .0000000E+00, .0000000E+00, .0000000E+00, .0000000E+00, .3674986E+06,
  6C, .0000000E+00, .0000000E+00, .0000000E+00, .0000000E+00, .0000000E+00,
1016, .7789035E-02,-.2596345E-02, .0000000E+00, .0000000E+00, .1392480E+05,col_O2_00(25)
  6B, 1234.56,OM(  6,  0: 1, 0)/GJJ=.1000E+01,A(  2,  0: 1, 0)=.0000E+00,.0000E+00,
  6B, 1234.56,OM(  4,  0: 1, 0)/GJJ=.1000E+01,A(  7,  0: 1, 0)=.0000E+00,.0000E+00,

  7A,O               ,0, 0, 0,  76667.807,
  7C, .0000000E+00, .0000000E+00, .0000000E+00, .0000000E+00, .0000000E+00,
0300, .0000000E+00, .0000000E+00, .0000000E+00, .0000000E+00, .3674986E+06,
  7C, .3200000E+00, .0000000E+00, .0000000E+00, .0000000E+00, .0000000E+00,
```

```
1000,-.2060000E+01, .2060000E+01, .3120000E+01, .0000000E+00, .1579328E+06,collstr1(67)
  7C, .0000000E+00, .0000000E+00, .0000000E+00, .0000000E+00, .0000000E+00,
1000,-.4700000E+01, .4700000E+01, .4350000E+01, .0000000E+00, .1806685E+06,collstr1(68)
  7C, .0000000E+00, .0000000E+00, .0000000E+00, .0000000E+00, .0000000E+00,
1000,-.4000000E+01, .4000000E+01, .3000000E+01, .0000000E+00, .2065547E+06,collstr1(69)
  7B, 1234.56,OM(  7,  0: 1, 0)/GJJ=.1000E+01,A(  0,  0: 0, 0)=.0000E+00,.0000E+00,
  7B, 1234.56,OM( 12,  0: 1, 0)/GJJ=.1000E+01,A(  0,  0: 0, 0)=.0000E+00,.0000E+00,
  7C, .0000000E+00, .0000000E+00, .0000000E+00, .0000000E+00, .0000000E+00,
0100, .0000000E+00, .0000000E+00, .0000000E+00, .0000000E+00, .3674986E+06,
  7C, .0000000E+00, .0000000E+00, .0000000E+00, .0000000E+00, .0000000E+00,
1007, .5628941E-01,-.5628941E-01, .0000000E+00, .0000000E+00, .1972680E+05,col_O2_00(24)
  7B, 1234.56,OM(  7,  0: 1, 0)/GJJ=.1000E+01,A(  4,  0: 1, 0)=.0000E+00,.0000E+00,
  7B, 1234.56,OM(  2,  0: 1, 0)/GJJ=.1000E+01,A(  6,  0: 1, 0)=.0000E+00,.0000E+00,
  7C, .0000000E+00, .0000000E+00, .0000000E+00, .0000000E+00, .0000000E+00,
0100, .0000000E+00, .0000000E+00, .0000000E+00, .0000000E+00, .1098370E+06,DES10feb2011(0),
  7C, .0000000E+00, .0000000E+00, .0000000E+00, .0000000E+00, .0000000E+00,
5000, .0000000E+00, .0000000E+00, .0000000E+00, .0000000E+00, .1098370E+06,
  7B,  910.44,OM(  7,  0: 1, 0)/GJJ=.1000E+01,A(  0,  0: 0, 0)=.3546E-08,.0000E+00,
  7B,  910.44,OM( 12,  0: 1, 0)/GJJ=.1000E+01,A(  0,  0: 0, 0)=.3546E-08,.0000E+00,
  7C, .0000000E+00, .0000000E+00, .0000000E+00, .0000000E+00, .0000000E+00,
0100, .0000000E+00, .0000000E+00, .0000000E+00, .0000000E+00, .1098370E+06,DESemail14mar2011,
  7C, .0000000E+00, .0000000E+00, .0000000E+00, .0000000E+00, .0000000E+00,
6000, .0000000E+00, .0000000E+00, .0000000E+00, .0000000E+00, .1098370E+06,
  7B,  910.44,OM(  7,  1: 1, 0)/GJJ=.1000E+01,A(  0,  0: 0, 0)=.2000E-06,.0000E+00,
  7B,  910.44,OM(  7,  1: 1, 0)/GJJ=.1000E+01,A(  0,  0: 0, 0)=.2000E-06,.0000E+00,

  8A,H2O+            ,0, 0, 0, 101770.996,
  8C, .0000000E+00, .0000000E+00, .0000000E+00, .0000000E+00, .0000000E+00,
0100, .0000000E+00, .0000000E+00, .0000000E+00, .0000000E+00, .3674986E+06,
  8C, .0000000E+00, .0000000E+00, .0000000E+00, .0000000E+00, .0000000E+00,
1030, .0000000E+00, .6707000E+01, .0000000E+00, .0000000E+00, .3481200E+03,satmag_col0(20)
```

```
  8B, 1234.56,OM(  8,  2: 1, 0)/GJJ=.1000E+01,A(  0,  0: 0, 0)=.0000E+00,.0000E+00,
  8B, 1234.56,OM(  6,  1: 1, 0)/GJJ=.1000E+01,A(  4,  1: 1, 0)=.0000E+00,.0000E+00,
  8C, .0000000E+00, .0000000E+00, .0000000E+00, .0000000E+00, .0000000E+00,
0100, .0000000E+00, .0000000E+00, .0000000E+00, .0000000E+00, .3674986E+06,
  8C, .0000000E+00, .5090000E+00, .0000000E+00, .0000000E+00, .1170700E+02,
1010,-.2036000E+01, .0000000E+00, .5090000E+01, .2660000E+00, .6266160E+05,satmag_col0(30)
  8B, 1234.56,OM(  8,  1: 1, 0)/GJJ=.1000E+01,A(  0,  0: 0, 0)=.0000E+00,.0000E+00,
  8B, 1234.56,OM(  9,  0: 1, 0)/GJJ=.1000E+01,A(  6,  1: 1, 0)=.0000E+00,.0000E+00,
  8C, .0000000E+00, .0000000E+00, .0000000E+00, .0000000E+00, .0000000E+00,
0100, .0000000E+00, .0000000E+00, .0000000E+00, .0000000E+00, .3674986E+06,
  8C, .0000000E+00, .1568000E+00, .0000000E+00, .0000000E+00, .3606400E+01,
1010,-.6272000E+00, .0000000E+00, .1568000E+01, .2660000E+00, .7086563E+05,satmag_col0(31)
  8B, 1234.56,OM(  8,  1: 1, 0)/GJJ=.1000E+01,A(  0,  0: 0, 0)=.0000E+00,.0000E+00,
  8B, 1234.56,OM( 11,  0: 1, 0)/GJJ=.1000E+01,A(  4,  1: 1, 0)=.0000E+00,.0000E+00,
  8C, .0000000E+00, .0000000E+00, .0000000E+00, .0000000E+00, .0000000E+00,
0100, .0000000E+00, .0000000E+00, .0000000E+00, .0000000E+00, .3674986E+06,
  8C, .0000000E+00, .0000000E+00, .0000000E+00, .0000000E+00, .0000000E+00,
1038, .8615000E+00, .0000000E+00, .0000000E+00, .0000000E+00, .1160400E+02,col_h2o_02(192)
  8B, 1234.56,OM(  8,  0: 1, 0)/GJJ=.1000E+01,A(  1,  0: 1, 0)=.0000E+00,.0000E+00,
  8B, 1234.56,OM(  5,  0: 1, 0)/GJJ=.1000E+01,A(  4,  0: 1, 0)=.0000E+00,.0000E+00,

  9A,OH+               ,0, 0, 0, 145289.429,
  9C, .0000000E+00, .0000000E+00, .0000000E+00, .0000000E+00, .0000000E+00,
0800, .0000000E+00, .0000000E+00, .0000000E+00, .0000000E+00, .3674986E+06,
  9C, .1356600E-01,-.3157700E-02, .7591700E-01,-.1097100E+00, .5315300E-01,
1030, .0000000E+00, .0000000E+00, .0000000E+00, .1202300E-01, .1160400E+03,col_h2o_02(68)
  9C, .2888770E-02, .4902000E+01, .1352100E+01, .0000000E+00, .0000000E+00,
1040, .0000000E+00, .0000000E+00, .0000000E+00, .0000000E+00, .3481200E+03,col_h2o_02(69)
  9C, .2347000E-02, .1006600E+02, .1150900E+01, .0000000E+00, .0000000E+00,
1040, .0000000E+00, .0000000E+00, .0000000E+00, .0000000E+00, .1241628E+04,col_h2o_02(70)
  9C, .8300000E-03, .1006600E+02, .1070700E+01, .0000000E+00, .0000000E+00,
```

```
1040, .0000000E+00, .0000000E+00, .0000000E+00, .0000000E+00, .2060870E+04,col_h2o_02(71)
  9C, .2480000E-02, .1006600E+02, .1089540E+01, .0000000E+00, .0000000E+00,
1040, .0000000E+00, .0000000E+00, .0000000E+00, .0000000E+00, .2283203E+04,col_h2o_02(72)
  9C, .1600000E-02, .1006600E+02, .1064710E+01, .0000000E+00, .0000000E+00,
1040, .0000000E+00, .0000000E+00, .0000000E+00, .0000000E+00, .2436840E+04,col_h2o_02(73)
  9C, .3200000E-02, .1006600E+02, .1219400E+01, .0000000E+00, .0000000E+00,
1040, .0000000E+00, .0000000E+00, .0000000E+00, .0000000E+00, .2552880E+04,col_h2o_02(74)
  9C, .5200000E-02, .9006600E+00, .2000000E+01, .0000000E+00, .0000000E+00,
1050, .0000000E+00, .0000000E+00, .0000000E+00, .0000000E+00, .1160400E+03,col_h2o_02(75)
  9B, 1234.56,OM(  9,  2: 1, 0)/GJJ=.1000E+01,A(  0,  0: 0, 0)=.0000E+00,.0000E+00,
  9B, 1234.56,OM(  6,  1: 1, 0)/GJJ=.1000E+01,A(  7,  1: 1, 0)=.0000E+00,.0000E+00,
  9C, .0000000E+00, .0000000E+00, .0000000E+00, .0000000E+00, .0000000E+00,
0100, .0000000E+00, .0000000E+00, .0000000E+00, .0000000E+00, .3674986E+06,
  9C, .0000000E+00, .5345000E+00, .0000000E+00, .0000000E+00, .1229350E+02,
1010,-.2138000E+01, .0000000E+00, .5345000E+01, .2660000E+00, .5906436E+05,satmag_col0(38)
  9B, 1234.56,OM(  9,  1: 1, 0)/GJJ=.1000E+01,A(  0,  0: 0, 0)=.0000E+00,.0000E+00,
  9B, 1234.56,OM( 12,  0: 1, 0)/GJJ=.1000E+01,A(  6,  1: 1, 0)=.0000E+00,.0000E+00,
  9C, .0000000E+00, .0000000E+00, .0000000E+00, .0000000E+00, .0000000E+00,
0100, .0000000E+00, .0000000E+00, .0000000E+00, .0000000E+00, .3674986E+06,
  9C, .0000000E+00, .5345000E+00, .0000000E+00, .0000000E+00, .1229350E+02,
1010,-.2138000E+01, .0000000E+00, .5345000E+01, .2660000E+00, .5906436E+05,satmag_col0(39)
  9B, 1234.56,OM(  9,  1: 1, 0)/GJJ=.1000E+01,A(  0,  0: 0, 0)=.0000E+00,.0000E+00,
  9B, 1234.56,OM( 11,  0: 1, 0)/GJJ=.1000E+01,A(  7,  1: 1, 0)=.0000E+00,.0000E+00,
  9C, .0000000E+00, .0000000E+00, .0000000E+00, .0000000E+00, .0000000E+00,
0400, .0000000E+00, .0000000E+00, .0000000E+00, .0000000E+00, .3674986E+06,
  9C, .3026408E+01,-.8823000E+00, .9411765E+03, .0000000E+00, .0000000E+00,
1079, .0000000E+00, .0000000E+00, .7696393E-02, .0000000E+00, .1232925E+05,col_h2o_02(98)
  9C, .4370319E+03,-.8838491E+00,.10000000E+01, .0000000E+00, .0000000E+00,
1069,-.1580161E+03, .1052722E+04, .1597144E+04, .0000000E+00, .1160400E+08,col_h2o_02(99)
  9C,-.4276160E+04,-.8838491E+00,.10000000E+01, .0000000E+00, .0000000E+00,
1069, .2918060E+04, .8327659E+04, .1506038E+05, .0000000E+00, .1160400E+09,col_h2o_02(100)
```

```
  9C, .0000000E+00, .4176613E+03, .3923055E+04,-.1502099E+05, .3640379E+05,
1019, .0000000E+00, .6325786E+02, .0000000E+00, .3738600E+00, .1160400E+10,col_h2o_02(101)
  9B, 1234.56,OM(  9,  1: 1, 0)/GJJ=.1000E+01,A(  1,  0: 1, 0)=.0000E+00,.0000E+00,
  9B, 1234.56,OM(  8,  0: 1, 0)/GJJ=.1000E+01,A(  4,  1: 1, 0)=.0000E+00,.0000E+00,
  9C, .0000000E+00, .0000000E+00, .0000000E+00, .0000000E+00, .0000000E+00,
0400, .0000000E+00, .0000000E+00, .0000000E+00, .0000000E+00, .3674986E+06,
  9C, .2476152E+01,-.8823000E+00, .9411765E+03, .0000000E+00, .0000000E+00,
1079, .0000000E+00, .0000000E+00, .6297049E-02, .0000000E+00, .1232925E+05,col_h2o_02(102)
  9C, .3575716E+03,-.8838491E+00,.10000000E+01, .0000000E+00, .0000000E+00,
1069,-.1292859E+03, .8613181E+03, .1306754E+04, .0000000E+00, .1160400E+08,col_h2o_02(103)
  9C,-.3498677E+04,-.8838491E+00,.10000000E+01, .0000000E+00, .0000000E+00,
1069, .2387504E+04, .6813539E+04, .1232213E+05, .0000000E+00, .1160400E+09,col_h2o_02(104)
  9C, .0000000E+00, .3417228E+03, .3209773E+04,-.1228990E+05, .2978492E+05,
1019, .0000000E+00, .5175643E+02, .0000000E+00, .3738600E+00, .1160400E+10,col_h2o_02(105)
  9B, 1234.56,OM(  9,  1: 1, 0)/GJJ=.1000E+01,A(  1,  0: 1, 0)=.0000E+00,.0000E+00,
  9B, 1234.56,OM(  5,  0: 1, 0)/GJJ=.1000E+01,A(  7,  1: 1, 0)=.0000E+00,.0000E+00,

 10A,H2+              ,0, 0, 0, 164665.117,
 10C, .0000000E+00, .0000000E+00, .0000000E+00, .0000000E+00, .0000000E+00,
0100, .0000000E+00, .0000000E+00, .0000000E+00, .0000000E+00, .3674986E+06,
 10C, .0000000E+00, .0000000E+00, .0000000E+00, .0000000E+00, .0000000E+00,
1030, .6690982E+00, .0000000E+00, .0000000E+00, .0000000E+00, .1160400E+04,satmag_col0(159)
 10B, 1234.56,OM( 10,  2: 1, 0)/GJJ=.1000E+01,A(  0,  0: 0, 0)=.0000E+00,.0000E+00,
 10B, 1234.56,OM(  6,  1: 1, 0)/GJJ=.1000E+01,A(  6,  1: 1, 0)=.0000E+00,.0000E+00,

 11A,H+               ,0, 0, 0, 186391.426,
 11C, .0000000E+00, .0000000E+00, .0000000E+00, .0000000E+00, .0000000E+00,
0400, .0000000E+00, .0000000E+00, .0000000E+00, .0000000E+00, .3674986E+06,
 11C, .3570000E+01,-.8823000E+00, .9900990E+03, .0000000E+00, .0000000E+00,
107b, .0000000E+00, .0000000E+00, .9078789E-02, .0000000E+00, .1172004E+05,col_h2o_02(14)
 11C, .5155300E+03,-.8838491E+00,.10000000E+01, .0000000E+00, .0000000E+00,
```

```
106b,-.1863984E+03, .1241808E+04, .1884017E+04, .0000000E+00, .1160400E+08,col_h2o_02(15)
 11C,-.5044228E+04,-.8838491E+00,.10000000E+01, .0000000E+00, .0000000E+00,
106b, .3442191E+04, .9823442E+04, .1776546E+05, .0000000E+00, .1160400E+09,col_h2o_02(16)
 11C, .0000000E+00, .4926800E+03, .4627700E+04,-.1771900E+05, .4413800E+05,
101b, .0000000E+00, .7462000E+02, .0000000E+00, .3738600E+00, .1160400E+10,col_h2o_02(17)
 11B, 1234.56,OM( 11,  1: 1, 0)/GJJ=.1000E+01,A(  1,  0: 1, 0)=.0000E+00,.0000E+00,
 11B, 1234.56,OM(  8,  0: 1, 0)/GJJ=.1000E+01,A(  6,  1: 1, 0)=.0000E+00,.0000E+00,
 11C, .0000000E+00, .0000000E+00, .0000000E+00, .0000000E+00, .0000000E+00,
0900, .0000000E+00, .0000000E+00, .0000000E+00, .0000000E+00, .3674986E+06,
 11C, .9321868E-04,-.1600000E+02, .7645260E+00, .0000000E+00, .0000000E+00,
106b,-.9321868E-04, .0000000E+00, .0000000E+00, .0000000E+00, .2276705E+03,col_h2o_02(35)
 11C, .2746787E-03, .0000000E+00, .1111466E+01, .0000000E+00, .0000000E+00,
106b, .7110308E-02,-.7110308E-02, .3875726E-02, .0000000E+00, .2480680E+03,col_h2o_02(36)
 11C, .0000000E+00, .0000000E+00, .1280825E+01, .0000000E+00, .0000000E+00,
106b,-.1528985E-01, .1668719E-01, .2168689E-01, .0000000E+00, .2757192E+03,col_h2o_02(37)
 11C, .3106220E-02,-.1751000E+01, .3380409E+01, .0000000E+00, .0000000E+00,
106b,-.3987298E-01, .3987298E-01, .3778714E-01, .0000000E+00, .3531480E+03,col_h2o_02(38)
 11C, .4415636E-01,-.1369000E+01, .8847915E+01, .0000000E+00, .0000000E+00,
106b,-.9804332E-01, .9804332E-01, .1015433E+00, .0000000E+00, .1193785E+04,col_h2o_02(39)
 11C, .1008007E+01,-.9300000E+00, .1098603E+03, .0000000E+00, .0000000E+00,
106b, .2806329E+00,-.2806329E+00, .3468455E+00, .0000000E+00, .1056251E+05,col_h2o_02(40)
 11C, .8160559E+02,-.7150000E+00, .4000000E+02, .0000000E+00, .0000000E+00,
106b,-.1158279E+03, .1158279E+03, .1084326E+03, .0000000E+00, .1160400E+07,col_h2o_02(41)
 11C, .1427819E+04,-.8000000E-01, .5000000E+01, .0000000E+00, .0000000E+00,
106b, .4365491E+03,-.4365491E+03, .3515161E+03, .0000000E+00, .4641600E+08,col_h2o_02(42)
 11C, .0000000E+00, .9494482E+04,-.2477546E+05, .4185651E+05,-.2598691E+05,
101b, .0000000E+00, .0000000E+00, .0000000E+00, .2289590E+00, .2320800E+09,col_h2o_02(43)
 11B, 1234.56,OM( 11,  1: 1, 0)/GJJ=.1000E+01,A(  7,  0: 1, 0)=.0000E+00,.0000E+00,
 11B, 1234.56,OM( 12,  0: 1, 0)/GJJ=.1000E+01,A(  6,  1: 1, 0)=.0000E+00,.0000E+00,
 11C, .0000000E+00, .0000000E+00, .0000000E+00, .0000000E+00, .0000000E+00,
0400, .0000000E+00, .0000000E+00, .0000000E+00, .0000000E+00, .3674986E+06,
```

```
 11C, .5794543E+00,-.1000000E+01, .1300000E+02, .0000000E+00, .0000000E+00,
107b, .1926389E+01,-.2162007E+01,-.1386246E+01, .0000000E+00, .1160400E+05,col_h2o_02(113)
 11C, .1602754E+03,-.6418600E+00, .3846154E+01, .0000000E+00, .0000000E+00,
106b,-.9732970E+02,-.5716446E+02,-.1530126E+03, .0000000E+00, .1508520E+06,col_h2o_02(114)
 11C, .1905447E+02,-.1115000E+01, .1200000E+03, .0000000E+00, .0000000E+00,
106b,-.4267509E+02, .8582420E+02, .1665368E+03, .0000000E+00, .5802000E+06,col_h2o_02(115)
 11C, .0000000E+00, .8182500E+05,-.2337200E+06, .3031500E+06,-.1496600E+06,
101b, .0000000E+00, .0000000E+00, .0000000E+00, .6166300E-01, .6962400E+08,col_h2o_02(116)
 11B, 1234.56,OM( 11,  1: 1, 0)/GJJ=.1000E+01,A(  2,  0: 1, 0)=.0000E+00,.0000E+00,
 11B, 1234.56,OM( 13,  0: 1, 0)/GJJ=.1000E+01,A(  6,  1: 1, 0)=.0000E+00,.0000E+00,
 11C, .0000000E+00, .0000000E+00, .0000000E+00, .0000000E+00, .0000000E+00,
0400, .0000000E+00, .0000000E+00, .0000000E+00, .0000000E+00, .3674986E+06,
 11C, .3570000E+01,-.8823000E+00, .9900990E+03, .0000000E+00, .0000000E+00,
107b, .0000000E+00, .0000000E+00, .9078789E-02, .0000000E+00, .1172004E+05,satmag_col0(167)
 11C, .5155300E+03,-.8838491E+00,.10000000E+01, .0000000E+00, .0000000E+00,
106b,-.1863984E+03, .1241808E+04, .1884017E+04, .0000000E+00, .1160400E+08,satmag_col0(168)
 11C,-.5044228E+04,-.8838491E+00,.10000000E+01, .0000000E+00, .0000000E+00,
106b, .3442191E+04, .9823442E+04, .1776546E+05, .0000000E+00, .1160400E+09,satmag_col0(169)
 11C, .0000000E+00, .4926800E+03, .4627700E+04,-.1771900E+05, .4413800E+05,
101b, .0000000E+00, .7462000E+02, .0000000E+00, .3738600E+00, .1160400E+10,satmag_col0(170)
 11B, 1234.56,OM( 11,  1: 1, 0)/GJJ=.1000E+01,A(  4,  0: 1, 0)=.0000E+00,.0000E+00,
 11B, 1234.56,OM(  9,  0: 1, 0)/GJJ=.1000E+01,A(  6,  1: 1, 0)=.0000E+00,.0000E+00,
 11C, .0000000E+00, .0000000E+00, .0000000E+00, .0000000E+00, .0000000E+00,
0300, .0000000E+00, .0000000E+00, .0000000E+00, .0000000E+00, .3674986E+06,
 11C, .5094504E+01,-.8453121E+00, .3030300E+04, .0000000E+00, .0000000E+00,
107b, .0000000E+00, .0000000E+00, .0000000E+00, .0000000E+00, .1531728E+05,col_h2o_02(77)
 11C, .2020400E+05, .2000000E+01, .1750000E+02, .0000000E+00, .0000000E+00,
106b, .2998900E+05,-.4615301E+05,-.8769700E+04, .0000000E+00, .4641600E+08,col_h2o_02(78)
 11C, .3227100E+04,-.3483700E+03, .0000000E+00, .0000000E+00,-.2000000E+04,
101b, .0000000E+00, .0000000E+00, .0000000E+00, .2454700E+00, .8122800E+09,col_h2o_02(79)
 11B, 1234.56,OM( 11,  1: 1, 0)/GJJ=.1000E+01,A(  6,  0: 1, 0)=.0000E+00,.0000E+00,
```

```
 11B, 1234.56,OM( 11,  0: 1, 0)/GJJ=.1000E+01,A(  6,  1: 1, 0)=.0000E+00,.0000E+00,
 11C, .0000000E+00, .0000000E+00, .0000000E+00, .0000000E+00, .0000000E+00,
0700, .0000000E+00, .0000000E+00, .0000000E+00, .0000000E+00, .3674986E+06,
 11C, .0000000E+00,-.1086500E+02, .0000000E+00,-.1155100E-05, .0000000E+00,
102b,-.2042300E+02, .1938000E+02, .3424600E+02, .9116500E-01, .9167160E+04,col_h2o_02(84)
 11C, .8900000E+00, .9610000E+00, .4897000E+01, .0000000E+00, .0000000E+00,
105b, .0000000E+00, .0000000E+00, .0000000E+00, .0000000E+00, .9167160E+04,col_h2o_02(85)
 11C,-.5800000E+00, .1910000E+01, .2565800E+01, .0000000E+00, .0000000E+00,
105b, .0000000E+00, .0000000E+00, .0000000E+00, .0000000E+00, .9167160E+04,col_h2o_02(86)
 11C,-.5800000E+00, .1000000E+01, .9427000E+01, .0000000E+00, .0000000E+00,
105b, .0000000E+00, .0000000E+00, .0000000E+00, .0000000E+00, .9167160E+04,col_h2o_02(87)
 11C,-.2900000E+00, .2000000E+01, .3373000E+01, .0000000E+00, .0000000E+00,
105b, .0000000E+00, .0000000E+00, .0000000E+00, .0000000E+00, .9167160E+04,col_h2o_02(88)
 11C, .2250000E+01, .1900000E+01, .1000000E+01, .0000000E+00, .0000000E+00,
105b, .0000000E+00, .0000000E+00, .0000000E+00, .0000000E+00, .9167160E+04,col_h2o_02(89)
 11C,-.1500000E+00, .5900000E+01, .1330000E+01, .0000000E+00, .0000000E+00,
105b, .0000000E+00, .0000000E+00, .0000000E+00, .0000000E+00, .9167160E+04,col_h2o_02(90)
 11B, 1234.56,OM( 11,  1: 1, 0)/GJJ=.1000E+01,A(  3,  0: 1, 0)=.0000E+00,.0000E+00,
 11B, 1234.56,OM( 10,  0: 1, 0)/GJJ=.1000E+01,A(  6,  1: 1, 0)=.0000E+00,.0000E+00,

 12A,O+              ,0, 0, 0, 186504.344,
 12C, .0000000E+00, .0000000E+00, .0000000E+00, .0000000E+00, .0000000E+00,
0900, .0000000E+00, .0000000E+00, .0000000E+00, .0000000E+00, .3674986E+06,
 12C, .6036705E-22,-.1600000E+02, .1643348E+02, .0000000E+00, .0000000E+00,
107c,-.6036705E-22, .0000000E+00, .0000000E+00, .0000000E+00, .2276705E+03,col_h2o_02(53)
 12C, .4394864E-02,-.1539292E+02, .1118250E+01, .0000000E+00, .0000000E+00,
106c, .2301992E+01,-.2301992E+01,-.2197655E+01, .0000000E+00, .3741418E+04,col_h2o_02(54)
 12C, .0000000E+00, .0000000E+00, .1296104E+01, .0000000E+00, .0000000E+00,
106c,-.1530023E+00, .1743264E+00, .2629578E+00, .0000000E+00, .4183841E+04,col_h2o_02(55)
 12C, .4969952E-01,-.1734100E+01, .3480364E+01, .0000000E+00, .0000000E+00,
106c,-.5979301E+00, .5979301E+00, .5617972E+00, .0000000E+00, .5422694E+04,col_h2o_02(56)
```

```
 12C, .7066082E+00,-.1348000E+01, .8942552E+01, .0000000E+00, .0000000E+00,
106c,-.2142362E+01, .2142362E+01, .2050933E+01, .0000000E+00, .1887295E+05,col_h2o_02(57)
 12C, .1613449E+02,-.9370660E+00, .7700598E+02, .0000000E+00, .0000000E+00,
106c, .2485335E+02,-.2485335E+02,-.5730985E+01, .0000000E+00, .1687723E+06,col_h2o_02(58)
 12C, .8922453E+03,-.8491441E+00, .1857143E+02, .0000000E+00, .0000000E+00,
106c, .2367966E+01, .5028675E+02, .2125555E+03, .0000000E+00, .1299648E+08,col_h2o_02(59)
 12C, .7427399E+03,-.6449700E+00, .5384615E+01, .0000000E+00, .0000000E+00,
106c, .4544951E+04, .6002309E+04, .1316887E+05, .0000000E+00, .2413632E+09,col_h2o_02(60)
 12C, .0000000E+00, .6454418E+05,-.5335363E+05, .2109851E+06,-.2037416E+06,
101c, .0000000E+00, .0000000E+00, .0000000E+00, .6419800E-01, .1299648E+10,col_h2o_02(61)
 12B, 1234.56,OM( 12,  1: 1, 0)/GJJ=.1000E+01,A(  6,  0: 1, 0)=.0000E+00,.0000E+00,
 12B, 1234.56,OM( 11,  0: 1, 0)/GJJ=.1000E+01,A(  7,  1: 1, 0)=.0000E+00,.0000E+00,
 12C, .0000000E+00, .0000000E+00, .0000000E+00, .0000000E+00, .0000000E+00,
0400, .0000000E+00, .0000000E+00, .0000000E+00, .0000000E+00, .3674986E+06,
 12C, .4569600E+01,-.8823000E+00, .9900990E+03, .0000000E+00, .0000000E+00,
107c, .0000000E+00, .0000000E+00, .1162085E-01, .0000000E+00, .1160400E+05,col_h2o_02(22)
 12C, .6598783E+03,-.8838491E+00,.10000000E+01, .0000000E+00, .0000000E+00,
106c,-.2385899E+03, .1589515E+04, .2411541E+04, .0000000E+00, .1160400E+08,col_h2o_02(23)
 12C,-.6456612E+04,-.8838491E+00,.10000000E+01, .0000000E+00, .0000000E+00,
106c, .4406005E+04, .1257401E+05, .2273979E+05, .0000000E+00, .1160400E+09,col_h2o_02(24)
 12C, .0000000E+00, .6306304E+03, .5923456E+04,-.2268032E+05, .5649664E+05,
101c, .0000000E+00, .9551360E+02, .0000000E+00, .3738600E+00, .1160400E+10,col_h2o_02(25)
 12B, 1234.56,OM( 12,  1: 1, 0)/GJJ=.1000E+01,A(  1,  0: 1, 0)=.0000E+00,.0000E+00,
 12B, 1234.56,OM(  8,  0: 1, 0)/GJJ=.1000E+01,A(  7,  1: 0, 0)=.0000E+00,.0000E+00,
 12C, .0000000E+00, .0000000E+00, .0000000E+00, .0000000E+00, .0000000E+00,
0100, .0000000E+00, .0000000E+00, .0000000E+00, .0000000E+00, .3674986E+06,
 12C,-.3015800E+04, .1473800E+04, .1165800E+03,-.9284400E+03, .1393200E+04,
103c,-.3486400E+04, .3486400E+04, .7040100E+03, .1349000E-01, .1181287E+05,satmag_col0(163)
 12B, 1234.56,OM( 12,  1: 1, 0)/GJJ=.1000E+01,A(  4,  0: 1, 0)=.0000E+00,.0000E+00,
 12B, 1234.56,OM(  9,  0: 1, 0)/GJJ=.1000E+01,A(  7,  1: 1, 0)=.0000E+00,.0000E+00,
 12C, .0000000E+00, .0000000E+00, .0000000E+00, .0000000E+00, .0000000E+00,
```

```
0300, .0000000E+00, .0000000E+00, .0000000E+00, .0000000E+00, .3674986E+06,
 12C, .8922453E+03,-.8491441E+00, .1857143E+02, .0000000E+00, .0000000E+00,
107c, .2367966E+01, .5028675E+02, .2125555E+03, .0000000E+00, .1299648E+08,col_h2o_02(65)
 12C, .7427399E+03,-.6449700E+00, .5384615E+01, .0000000E+00, .0000000E+00,
106c, .4544951E+04, .6002309E+04, .1316887E+05, .0000000E+00, .2413632E+09,col_h2o_02(66)
 12C, .0000000E+00, .6454418E+05,-.5335363E+05, .2109851E+06,-.2037416E+06,
101c, .0000000E+00, .0000000E+00, .0000000E+00, .6419800E-01, .1299648E+10,col_h2o_02(67)
 12B, 1234.56,OM( 12,  1: 1, 0)/GJJ=.1000E+01,A(  7,  0: 1, 0)=.0000E+00,.0000E+00,
 12B, 1234.56,OM( 12,  0: 1, 0)/GJJ=.1000E+01,A(  7,  1: 1, 0)=.0000E+00,.0000E+00,
 12C, .0000000E+00, .0000000E+00, .0000000E+00, .0000000E+00, .0000000E+00,
0700, .0000000E+00, .0000000E+00, .0000000E+00, .0000000E+00, .3674986E+06,
 12C, .0000000E+00,-.1744911E+03, .0000000E+00,-.1855083E-04, .0000000E+00,
102c,-.3279920E+03, .3112415E+03, .5499850E+03, .9116500E-01, .1466746E+06,col_h2o_02(91)
 12C, .1429334E+02, .9610000E+00, .4897000E+01, .0000000E+00, .0000000E+00,
105c, .0000000E+00, .0000000E+00, .0000000E+00, .0000000E+00, .1466746E+06,col_h2o_02(92)
 12C,-.9314762E+01, .1910000E+01, .2565800E+01, .0000000E+00, .0000000E+00,
105c, .0000000E+00, .0000000E+00, .0000000E+00, .0000000E+00, .1466746E+06,col_h2o_02(93)
 12C,-.9314762E+01, .1000000E+01, .9427000E+01, .0000000E+00, .0000000E+00,
105c, .0000000E+00, .0000000E+00, .0000000E+00, .0000000E+00, .1466746E+06,col_h2o_02(94)
 12C,-.4657381E+01, .2000000E+01, .3373000E+01, .0000000E+00, .0000000E+00,
105c, .0000000E+00, .0000000E+00, .0000000E+00, .0000000E+00, .1466746E+06,col_h2o_02(95)
 12C, .3613485E+02, .1900000E+01, .1000000E+01, .0000000E+00, .0000000E+00,
105c, .0000000E+00, .0000000E+00, .0000000E+00, .0000000E+00, .1466746E+06,col_h2o_02(96)
 12C,-.2408990E+01, .5900000E+01, .1330000E+01, .0000000E+00, .0000000E+00,
105c, .0000000E+00, .0000000E+00, .0000000E+00, .0000000E+00, .1466746E+06,col_h2o_02(97)
 12B, 1234.56,OM( 12,  1: 1, 0)/GJJ=.1000E+01,A(  3,  0: 1, 0)=.0000E+00,.0000E+00,
 12B, 1234.56,OM( 10,  0: 1, 0)/GJJ=.1000E+01,A(  7,  1: 1, 0)=.0000E+00,.0000E+00,
 12C, .0000000E+00, .0000000E+00, .0000000E+00, .0000000E+00, .0000000E+00,
0300, .0000000E+00, .0000000E+00, .0000000E+00, .0000000E+00, .3674986E+06,
 12C, .1949251E+00,-.1000000E+01, .1000000E+03, .0000000E+00, .0000000E+00,
107c, .4380751E+00,-.4733288E+00,-.2490537E+00, .0000000E+00, .1160400E+05,col_h2o_02(117)
```

```
 12C, .4562045E+03,-.6418600E+00, .5000000E+01, .0000000E+00, .0000000E+00,
106c,-.3256285E+03,-.1117925E+03,-.3949023E+03, .0000000E+00, .1160400E+07,col_h2o_02(118)
 12C, .2154629E+03,-.1199180E+01, .1000000E+02, .0000000E+00, .0000000E+00,
106c, .1442955E+03,-.6157453E+02, .1102506E+03, .0000000E+00, .5802000E+07,col_h2o_02(119)
 12B, 1234.56,OM( 12,  1: 1, 0)/GJJ=.1000E+01,A(  2,  0: 1, 0)=.0000E+00,.0000E+00,
 12B, 1234.56,OM( 13,  0: 1, 0)/GJJ=.1000E+01,A(  7,  1: 1, 0)=.0000E+00,.0000E+00,

 13A,O2+             ,0, 0, 0, 230593.817,
 13C, .0000000E+00, .0000000E+00, .0000000E+00, .0000000E+00, .0000000E+00,
0100, .0000000E+00, .0000000E+00, .0000000E+00, .0000000E+00, .3674986E+06,
 13C,-.1844900E+02, .2716600E+03, .0000000E+00,-.2149400E+03, .0000000E+00,
1010,-.7953600E+02, .4055400E+02, .9064600E+01, .5248100E-02, .7731745E+05,satmag_col0(11)
 13B, 1234.56,OM( 13,  1: 1, 0)/GJJ=.1000E+01,A(  0,  0: 0, 0)=.0000E+00,.0000E+00,
 13B, 1234.56,OM( 12,  0: 1, 0)/GJJ=.1000E+01,A(  7,  1: 1, 0)=.0000E+00,.0000E+00,
 13C, .0000000E+00, .0000000E+00, .0000000E+00, .0000000E+00, .0000000E+00,
0100, .0000000E+00, .0000000E+00, .0000000E+00, .0000000E+00, .3674986E+06,
 13C, .0000000E+00, .0000000E+00, .0000000E+00, .0000000E+00, .0000000E+00,
1030, .3954000E+00, .0000000E+00, .0000000E+00, .0000000E+00, .2320800E+03,satmag_col0(22)
 13B, 1234.56,OM( 13,  2: 1, 0)/GJJ=.1000E+01,A(  0,  0: 0, 0)=.0000E+00,.0000E+00,
 13B, 1234.56,OM(  7,  1: 1, 0)/GJJ=.1000E+01,A(  7,  1: 1, 0)=.0000E+00,.0000E+00,
```